# Waves generated by subaerial high mobility slides : insight from a numerical model with a focus on energetic processes

Amirhossein Parvinashtiani

## ▶ To cite this version:

Amirhossein Parvinashtiani. Waves generated by subaerial high mobility slides : insight from a numerical model with a focus on energetic processes. Mechanics [physics]. Université de Pau et des Pays de l'Adour, 2024. English. NNT : 2024PAUU3012 . tel-04815165

**HAL Id: tel-04815165**
**https://theses.hal.science/tel-04815165v1**

Submitted on 2 Dec 2024

# Waves generated by subaerial high mobility slides: insight from a numerical model with a focus on energetic processes.

by:

***Amir H. Parvin A.***

A thesis presented for the degree of
Doctor of Philosophy

Jury president: Dr. Philippe Bonneton
Laboratoire SIAME
Université de Pau et des Pays de l'Adour
Anglet-France
May 31, 2024

# Approval Page

Après avis de :

| | | | |
|---|---|---|---|
| Philippe Gondret | Prof. | Université Paris-Sud | Rapporteur |
| Laurent Lacaze | DR CNRS (HdR) | IMFT | Rapporteur |

Devant la commission d'examen formée de :

| | | | |
|---|---|---|---|
| Philippe Bonneton | DR CNRS | Université de Bordeaux | Examinateur |
| Raphaël Paris | DR CNRS | Laboratoire Magmas et Volcans | Examinateur |
| Kamal El Omari | Maître de Conférences (HdR) | Université de La Réunion | Examinateur |
| Sylvain Viroulet | CR CNRS | IMFT | Invité |
| Yves Le Guer | Maître de Conférences (HdR) | UPPA | Directeur de thèse |
| Stéphane Abadie | Prof. | UPPA | Directeur de thèse |

## Abstract:

This thesis aims to improve the understanding of the generation and subsequent transformations of impulse waves generated by a subaerial fluid-like slides. The approach is entirely based on a VOF-RANS numerical model. The focus is on the energetic processes and the effect of the subaerial slide rheology and submergence. The model is first validated considering each individual physical processes at stake, including slide propagation, wave generation and breaking, wave dispersion, energy conservation and dissipation. This work pointed out the importance of a fine tuning of the model for a proper description of the processes. With the model set-up proposed, we achieved a correct representation of the dissipation processes, but not perfect, as non negligible numerical dissipation is still present for the most violent wave breaking cases.

The model is then used to conduct a numerical experiment involving a subaerial triangular water slide initially at rest just at the water line. The volume of the slide is gradually increased. The objective is to understand how the slide energy transfers to the free surface and then, how the wave processes (dispersion, breaking) act to shape the final leading wave energy, which is our hazard indicator. The leading wave energy, at the end of the channel, appears to be the result of a set of sequential processes. Generation determines the basic impulse wave characteristics and from there, the future evolution of the wave. Schematically, depending on its initial characteristics, the impulse wave will be either shaped by dispersion, by breaking, or by a combination of the two. Finally, considering the global energetic process from the initial slide potential energy to the final leading wave energy, we show that the process efficiency has an optimum for an intermediate slide volume.

The next phase explores the effects of the slide rheology and initial elevation. First, the slides with more mobility (low viscosity) were demonstrated to be more efficient in transferring their energy to the impulse wave. Second, among all the tested rheological parameters, the yield stress was shown to be the more influential parameter in reducing this efficiency. Different slide elevations were also tested and a lower energy transfer efficiency was found for this type of impact with high elevation in comparison with previous cases.

The final stage of the work consisted at gathering all the cases and trying to determine the important parameters which may explain the behavior observed. We investigated the role of the momentum flux and its time integrated version, the impulse. Based on our observations, the positive horizontal impulse seems to act as a constructive force and the negative horizontal impulse as a destructive one. We finally defined a new parameter called Efficient Impulse Ratio (EIR), which measures the fraction of horizontal impulse left for wave generation. This parameter explains reasonably well the different behaviors obtained in our results. Nevertheless, so far, this parameter is only descriptive and do not allow to relate the initial slide characteristics to the maximum wave energy.

---

**Keywords:** subaerial landslides, impulse wave, numerical modeling, dissipation, dispersion, rheological laws, impulse

---

**Total page numbers:** 153

**Résumé:**
Cette thèse vise à améliorer la compréhension de la génération et des transformations ultérieures des vagues impulsives générées par des glissements de fluides subaériens. L'approche est entièrement basée sur un modèle numérique VOF-RANS. L'accent est mis sur les processus énergétiques et l'effet de la rhéologie du glissement subaérien et de son immersion. Le modèle est d'abord validé en considérant chaque processus physique individuel mis en jeu, avec la propagation du glissement, la génération et la rupture des vagues, la dispersion, la conservation de l'énergie et la dissipation. Ce travail a souligné l'importance d'un réglage fin du modèle pour une description appropriée des processus. Avec le modèle proposé, nous avons obtenu une représentation correcte des processus de dissipation, bien que non parfaite, car une dissipation numérique non négligeable est encore présente pour les cas de rupture d'onde les plus violents.

Ensuite, le modèle est utilisé pour mener une expérience numérique impliquant le lâcher d'un volume triangulaire subaérien initialement au repos juste à la ligne d'eau. Le volume du glissement est progressivement augmenté. L'objectif est de comprendre comment l'énergie du glissement est transféré à la surface libre, puis comment les processus (dispersion, rupture) agissent pour façonner l'énergie finale de la vague principale, qui est notre indicateur de risque. L'énergie de la vague principale, à la fin du canal, semble être le résultat d'un ensemble de processus séquentiels. La génération détermine les caractéristiques de base de la vague d'impulsion et à partir de là, l'évolution future de la vague. Schématiquement, en fonction de ses caractéristiques initiales, la vague d'impulsion sera façonnée soit par la dispersion, soit par la rupture, soit par une combinaison des deux. Enfin, en considérant le processus énergétique global de l'énergie potentielle initiale du glissement à l'énergie finale de la vague principale, nous montrons que l'efficacité du processus a un optimum pour un volume de glissement intermédiaire.

La phase suivante du travail explore les effets de la rhéologie du glissement et de son émergence. Tout d'abord, il a été démontré que les glissements avec plus de mobilité (faible viscosité) sont plus efficaces pour transférer leur énergie à la vague d'impulsion. Ensuite, parmi tous les paramètres rhéologiques testés, la contrainte seuil s'est avérée être le paramètre le plus influent dans la réduction de cette efficacité. Différentes élévations de glissement ont également été testées, et une moindre efficacité de transfert d'énergie a été constatée pour ce type d'impact avec grande élévation par rapport aux cas précédents.

La dernière partie du travail consistait à rassembler tous les cas et à essayer de déterminer les paramètres importants pouvant expliquer le comportement observé. Nous avons étudié le rôle du flux de moment et de sa forme intégrée dans le temps, l'impulsion. Sur la base de nos observations, l'impulsion horizontale positive semble agir comme une force constructive et l'impulsion horizontale négative comme une force destructive. Nous avons enfin défini un nouveau paramètre appelé Ratio d'Impulsion Efficace (RIE), qui mesure la fraction d'impulsion horizontale utile pour la génération des vagues. Ce paramètre explique raisonnablement bien les différents comportements observés pour nos résultats. Ce paramètre est cependant uniquement descriptif et ne permet pas de relier les caractéristiques initiales du glissement à l'énergie maximale de la vague.

**Acknowledgment:**

I would like to start by thanking my supervisors, Yves Le Guer and Stéphane Abadie, for their invaluable guidance. I am particularly grateful to Yves for securing the funding from the TerraNAmi project: "Landslides and Mudflows Generating Waves," defining the project, and giving me the opportunity to work on such a unique and exciting topic. Although we could not benefit from experimental work for this study, your tremendous help and unwavering support throughout my Ph.D. were invaluable.

This research would not have been the same without the indispensable aid, involvement, and encouragement from Stéphane. His broad expertise and insights into the topic, along with his novel propositions during my most desperate moments, were critical to the completion of my research. I am also very grateful to my advisor, Kamal El Omari, who has been involved since the beginning of this journey. His expertise in CFD has always been a reliable source of knowledge for me. Additionally, I extend my gratitude to Volker Reober for allowing me to collaborate on the ALPHEUS project.

I would like to express my sincere thanks to all the jury members for their time and valuable feedback on my work. A special thanks goes to Philippe Gondret and Laurent Lacaze for their diligent review of my thesis and their constructive comments, which helped refine my research and improve its quality. The presence of Philippe Bonneton, Raphaël Paris, and Sylvain Viroulet at my defense was heartwarming and precious to me.

I should also thank my office mates and fellow Ph.D. students at the SIAME laboratory: Mohamed, Erwan, Jannik, Aritz, Émile, Diego, Fatima-Zahra, Solène, Maria, Kindro, Alexandre, and my compatriots Amin, Neda, Arash, Mojtaba, Ebrahim, Meysam, and Masoumeh for their support and for making this Ph.D. journey enjoyable. It has been an absolute delight working alongside them and spending time with them. Many thanks to the university's staff, Caroline Hanin and Natalia Hochman-Lefevre, for their assistance with the administrative paperwork since I came to France. Their hard work and support are greatly appreciated.

Lastly, I would like to express my deepest appreciation and gratitude to my family for their unwavering support throughout this thesis. Despite the demands of this work, they stood by me with understanding and patience, even when I couldn't spend as much time with them as I would have liked. Their encouragement and love have been a source of strength and motivation.

# Contents

# List of Figures

# List of Tables

# Chapter 1

# Introduction

---

Tsunamis are among the most destructive phenomenon on Earth. With the current trend of increasing population density at the coast, they poses a great challenge to the human society.

In this work, the focus is on tsunamis generated by landslides. After earthquakes, landslide tsunamis are the major cause of tsunamis, accounting for approximately 10% of tsunami occurrences in the period spanning from 1900 to 2020 (Reid and Mooney, 2023). A few reported landslide-induced tsunami events which occurred around the world are presented in Table 1.1. This table illustrates the recurrence and the fatalities associated to landslide tsunamis.

In this thesis, we study more specifically the problem of waves generated by subaerial landslides; a very complex problem involving granular physics, fluid mechanics and wave processes. Recently, a few studies (Bullard et al., 2019; Rauter et al., 2021) proposed a simplification of the generation stage, considering a water slide (i.e., a liquid with the same density as the reservoir fluid). In these studies, the authors concentrated on the prediction of the maximum wave amplitude after generation.

In the present work, we followed the same strategy of simplification, but we rather focused on the energetic transfer processes from the stage of generation, to the end of the main wave transformations. We also investigated the role of the slide rheology in greater details.

Our approach is based on a RANS multiphase Navier-Stokes VOF model (multiphaseInterFoam). This type of model (as soon as the generation stage is simplified), allows a complete description of the energetic processes and gives all the variables necessary for the interpretation.

The plan of the manuscript is the following.

After the literature review presented in chapter 2, chapter 3 is mainly devoted to the presentation of the numerical model. As it is intensively and exclusively used in this work, the model has been thoroughly validated, considering all the processes intended to be described, including energetic aspects. Therefore, chapter 3 presents the results obtained in all the test cases and proposes recommendations for the model set-up.

Chapter 4 is devoted to the thesis results. Here, the strategy followed consisted in initiating the study with the simplest phenomena and progressively introduce more complexity. Therefore, in the first step of the work, we considered low viscosity slides and conducted a comprehensive exploration of the impulse waves physics. This entails studying the wave parameters and the effective energetic processes, from the inception to the end. In a second step, we progressively introduced the slide complex rheology and the submergence effects on the wave characteristics. The final step was to gather all the cases

simulated and to try to propose an unified way of analysing the wave generation.
Finally, in the last chapter of this manuscript, the conclusions and perspectives of the work are drawn.

Table 1.1 – Record of historical landslide tsunamis.

| **Case** | **Year** | **H$_{max}$** | **Slide type** | Other information |
|---|---|---|---|---|
| Island of Santorini, Greece (Petley, 2023) | 1650 | 20 m | submerged | landslide triggered by Kolumbo volcano eruption in Aegean Sea |
| Ambon Island, Banda Sea (Pranantyo and Cummins, 2020) | 1674 | 100 m | submerged | 2347 casualties, landslide triggered by tectonic cause. |
| Storfjorden, Norway (Harbitz et al., 2014) | 1731 | 30 m | subaerial | 17 casualties |
| Oshima-Ōshima, Sea of Japan (Satake, 2007) | 1741 | 13-34 m | subaerial | The source of tsunami is subjected to debate |
| Langfjorden, Norway (Redfield and Osmundsen, 2009) | 1756 | 40-50 m | subaerial | 32 casualties |
| Mount Unzen, Japan (Miyamoto et al., 2010) | 1792 | 100 m | subaerial | around 15000 casualties, triggered by volcano eruption |
| Krakatoa, Sunda Strait (Latter, 1981) | 1883 | 24-42 m | subaerial | 30000 casualties |
| Lovatnet, Norway (Waldmann et al., 2021) | 1905 | 40 m | subaerial | 61 casualties |
| Disenchantment Bay, Alaska (Lander, 1996) | 1905 | $>$ 30 m | subaerial | A fallen glacier |
| Grand Banks, Canada (Fine et al., 2005) | 1929 | 3-8 m | submerged | Trigirred by earthquake, 28 casualties, 13 metres run-up on Burin Peninsula shore |
| Tafjorden, Norway (Harbitz et al., 2014) | 1934 | 63.5 m | subaerial | three tsunamis, 40 casualties |
| Lovatnet, Norway (Waldmann et al., 2021) | 1936 | 74 m | subaerial | three tsunamis, 74 casualties |
| Lituya Bay, Alaska (Lander, 1996) | 1958 | 524 m | subaerial | similar occurrences in 1854, 1899, and 1936. |
| Vajon dam, Italy (Datei, 2005) | 1963 | 27.5 m | subaerial | 1900-2500 casualties |
| Lembata, Indonesia (Paris et al., 2014) | 1979 | - | subaerial | >539 casualties, less than 10 m run-up inundation up to 1,500 m inland |
| Spirit Lake, Washington, US (Couston et al., 2015) | 1980 | 180-260 m | subaerial | magma-avalanche |
| Papua New Guinea (Davies, 2017) | 1998 | 15 m | submerge | 2200 casualties, landslide triggered with 7M earthquake. |
| Paatuut, Greenland (Dahl-Jensen et al., 2004) | 2000 | - | subaerial | rock avalanche, 50 m run-up close to the landslide place |
| Grijalva river, Mexico (Hernández-Madrigal et al., 2011) | 2007 | 15 m | subaerial | Debris flow, 30 casualties, The potential causative factors include a M4.5 earthquake that occurred 5 days before the landslide and a water-level drawdown of the river. |
| Taan Fiord, Alaska, US (Higman et al., 2018) | 2015 | 100 m | subaerial | Falling glacier and rock avalanche |
| Karrat Fjord, Greenland (Paris et al., 2019) | 2017 | 100 m | subaerial | rock avalanche, 4 casualties |
| Elliot Creek, British Columbia, Canada (Geertsema et al., 2022) | 2020 | 100 m | subaerial | rock avalanche |

# Chapter 2

# Literature review

---

In this chapter, we provide an overview of the previous researches focused on impulse waves generated by various types of slides including the fluid-like slide, focus of the present work. We also introduce the various classifications of landslides as well as different aspects of the rheological behavior of water-sediment mixtures. At the end of this chapter, the objective is to identify existing gaps within this field and accordingly define the goals of our study.

## 2.1 Notations

Before going in more detail into the previous works carried out in this topic, it is necessary to first define the different parameters required to describe the landslide impulse wave phenomenon.
Figure 2.1 shows a schematic sketch of the problem studied.
In a two-dimensional environment, a slide, with bulk density $\rho_s$, initial volume $v_0$, mass $m_0$, and average thickness $\bar{s}$, collides with the water at rest in the reservoir with an average velocity $\bar{v_s}$, generating an impulse wave train, generally consisting of a larger leading wave followed by the rest of the trailing waves. The zero subscript denotes the value of the variable at $t = 0$, time at which the slide starts to move.
The still water depth is $h_0$. Sine the domain is considered 2D its width is constant and equal to $b$. It is common to describe the slide or the wave parameters for a unit width of domain ($b = 1$ m). The water level variation can be described by the function $\eta(x, t)$ varying in space and time. The coordinate origin is set on the still water level. The leading wave is localized using an up-crossing method. The wavelength ($L_1$), wave period ($T_1$), and wave celerity ($C_1$) are analogously considered, the subscript number representing the wave (1 for leading wave, etc.). A superscript, $f$, $c$, or $t$, can also be added to this notation to designate the wavefront, the wave crest, or the wave trough, respectively. A leading wave amplitude is attributed to the crest (i.e., $a_1^c$) and to the trough (i.e., $a_1^t$), the corresponding wave height being the sum of the two.

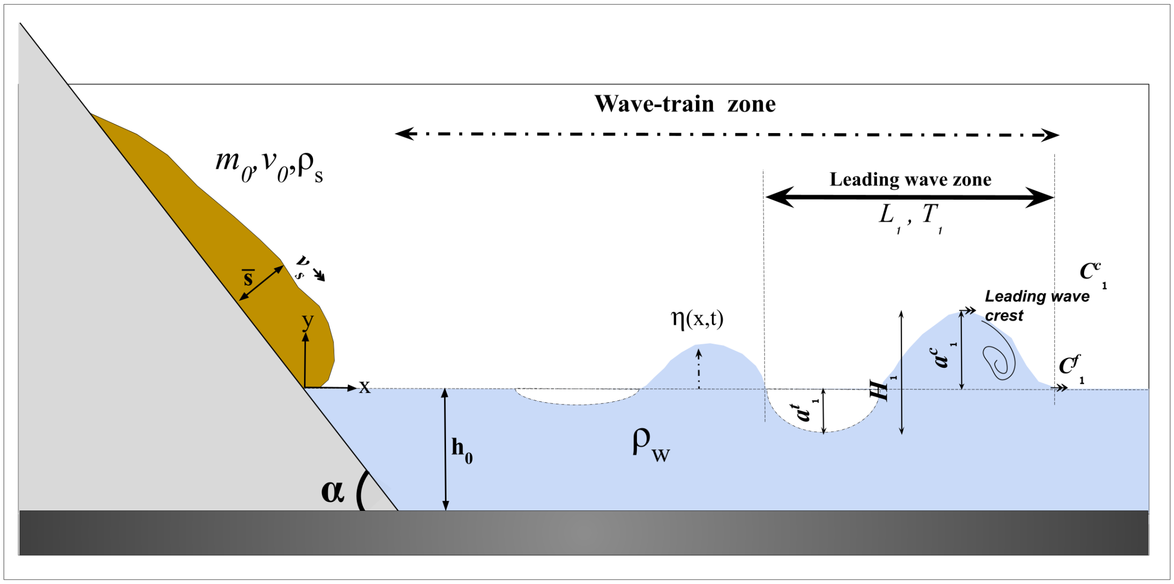

Figure 2.1 – Problem studied and associated parameters.

## 2.2 Dimensionless parameters

To compare the results for different conditions, we introduce dimensionless parameters represented by capital letters.

- dimensionless slide volume: $V_0 = \dfrac{v_0}{b\,h_0^2}$,
- dimensionless time: $t^* = t\sqrt{\dfrac{g}{h_0}}$,
- dimensionless near-field maximum wave amplitude: $A_{1,max} = \dfrac{a^c_{1,max}}{h_0}$,
- dimensionless slide mass: $M = \dfrac{m_0}{\rho_s\ b\ h_0^2}$,
- dimensionless slide thickness: $S = \dfrac{\bar{s}}{h_0}$,
- slide Froude number: $F = \dfrac{\bar{v}_s}{\sqrt{g\ h_0}}$,
- ratio between slide density and water density: $R = \dfrac{\rho_s}{\rho_w}$.

## 2.3 General overview of past studies and scaling relations

The present Ph.D. thesis specifically focuses on continuous flow-like landslides. The literature regarding fluid-like slides is comprehensively addressed in a separate section (section 2.6). Meanwhile, in this section, a brief overview of different previous experimental attempts is provided, since a majority of former studies were carried out with other forms of deformable slides.

In the scientific literature, various experimental approaches have been employed to study landslide tsunamis. The slide mechanism is one way to categorize them. Note that the experiments can also be categorized based on other factors such as whether the slides are submerged or subaerial, the experiment conducted in a 3D basin or a 2D prismatic wave channel, and the slopes varied or not, among others. Early investigations on impulsive waves trace back to Russell (1837), who utilized a moving vertical piston. Over the decades, experiments with sliding solid bodies, including materials like aluminum and PVC, have been also conducted (Kamphuis and Bowering (1970), Heinrich (1992), Panizzo et al. (2005), Ataie-Ashtiani and Nik-Khah (2008), Heller and Spinneken (2015)).

The deformed slides come in many shapes. In this domain, granular materials, whether natural or synthetic, have been mostly employed. Natural materials like rock and gravel have been utilized in studies such as Mohammed and Fritz (2012), Heller (2007) and Heller (2008), Bolin et al. (2014), McFall and Fritz (2016), and Wang et al. (2021) for example. Additionally, natural materials are placed in mesh-pack[1] forms, as seen in works such as Evers and Hager (2015) and Evers (2017). Synthetic materials, including polypropylene grains (Evers and Hager (2015), Evers (2017)), ceramic beads (Mulligan and Take (2017), and glass beads Viroulet et al. (2014), Viroulet et al. (2016), Robbe-Saule et al. (2021)), have also been widely adopted as sliding masses in laboratory experiments.

A few researchers have tried to predict the leading wave height resulting from a subaerial impact event by considering all the relevant parameters immediately at the point of the impact, namely,

- the still water depth in the reservoir,
- slide impact velocity,
- slide thickness,
- bulk slide volume,
- bulk slide density,
- slide impact angle,
- and grain diameter (for granular slides).

Semi-empirical relations for the near field nondimensional wave amplitude $A_{1,max}$ were derived from these experiments. Except for the Rauter et al. (2021) and Bullard et al. (2019) which slide is water, the rest of the relations are based on granular materials. A summary of the relationships derived follows:

$$A_{1,max} = A_{1,max}(M,\ F,\ S,\ \Delta T,\ R,\ cos(\alpha)), \tag{2.1}$$

(a) $A_{1,max} = \frac{1}{4}\ F^{7/5}\ S^{4/20};$ Fritz (2002)

(b) $A_{1,max} = \frac{4}{9}\ F^{4/5}\ S^{2/5}\ M^{1/5}\ cos\left(\frac{6}{7}\ \alpha\right)^{2/5};$ Heller and Hager (2010a)

(c) $A_{1,max} = \frac{1}{5}\ F^{1/5}\ S^{3/20}\ M^{9/20}\ cos\,(\alpha)^{7/20};$ Zitti et al. (2015)

$A_{1,max} = \frac{1}{2}\ F^{1/5}\ M^{4/5}\ \Delta T^{-1/5}\ cos\,(\alpha)^{7/10};$ same authors but considering landslide impact duration

---

[1] an open netted bag

(d) $A_{1,max} = \sqrt{1 + \ R\ S\ F^2\ cos(\alpha)^2} - 1;$ Mulligan and Take (2017)

(e) $A_{1,max} = \sqrt{1 + 2\ R\ S\ F^2\ cos(\alpha)^2} - 1;$ Bullard et al. (2019) (water slide)

(f) $A_{1,max} = 0.89\ F^{0.8}\ S^{0.50}\ M^{0.38}\ cos\,(\alpha)^{0.57};$ Rauter et al. (2021) (based on numerical modeling)

Note that these scaling relations involved highly energetic slide therefore entering the water body with a significant velocity ($\bar{v_s} >> 0$). Cases with short travel distances (like Viroulet et al. (2013)) and different failure mechanisms like cliff collapsing (like Robbe-Saule et al. (2021)) might require different scaling relations and parameterizations.

## 2.4 Wave characteristics

Another aspect of the previous investigations concerns the propagation and evolution of waves in the far-field. Seemingly, the amplitude decay for plane waves follows a power law. The following relationship were obtained (with $x$ propagation direction) : where $a_1^c \propto x^{-\frac{1}{2}}$ in Zweifel (2010), $a_1^c \propto x^{-\frac{4}{15}}$ in Heller and Hager (2010b), and $a_1^c \propto x^{-\frac{1}{3}}$ in Evers and Hager (2015).
The generated impulse wave is usually non linear. It also falls in the intermediate ($2 < L/h_0 < 20$) or close to the shallow-water ($L/h_0 > 20$) wave depth regimes. From the generation moment, the impulse wave characteristics constantly vary. First because it has been generated by an unsteady process, and second, because it is an individual impulse in quiescent water. This evolution can not be totally explained by the classical wave theory based on different assumptions. In some cases, the impulse wave train may be close to classical nonlinear wave theories such as the fifth-order Stokes and the first-order cnoidal wave theories (Fritz et al., 2004). Heller and Hager (2011) and Bougouin et al. (2020) also used the Stokes, cnoidal, solitary, and bore wave theories to describe the observed wave profiles in their experiments.
The next sections explain several aspects of the impulse wave evolution after generation.

### 2.4.1 Oscillatory waves and the Translatory waves

From the physical point of view, water waves can be classified either as "oscillatory" or "translatory" waves (Stoker, 1992). In oscillatory waves, the average transport of fluid, namely the discharge or mass transport, is nil, similarly as in the transverse oscillation of a rope. Generally, all the regular wave theories such as Airy, Stokes, Cnoidal, and stationary waves fall into this category (Le Méhauté, 1976).
In translatory waves, there is a transport of water mass in the direction of the propagation. Examples of such phenomena are tidal bores or moving hydraulic jumps; waves generated by the breaking of a dam; surges on a dry bed; undulated moving hydraulic jumps; solitary waves; and flood waves in rivers. It is pointed out that oscillatory and translatory waves may sometimes look very much alike and be treated mathematically by the same method.
For example, a solitary wave, which is a translatory wave, is characterized by a unique wave crest accompanied by a sudden jump ahead by the water particles under the wave crest. Cnoidal waves, which are oscillatory waves, present very similar characteristics. However, in the case of a cnoidal wave, there is a gentle slow return under a long flat trough between wave crests. A solitary wave motion always involves an important net mass transport. A cnoidal wave has a very small mass transport because of this return flow. From the mathematical point of view, nevertheless, these two wave theories are of the same family, namely, they are subject to the same simplifying assumptions and obey the

same basic equations. The solitary wave is seen as a limited case of the cnoidal wave when the wave period tends to infinity (Figure 2.2).

As a shock wave phenomenon, a breaking wave is a type of translatory wave, a type also encountered in gas dynamics. This phenomenon is characterized by its high non-linearity, turbulence production (associated with a high rate of energy dissipation) and air entrainment (Le Méhauté, 1976).

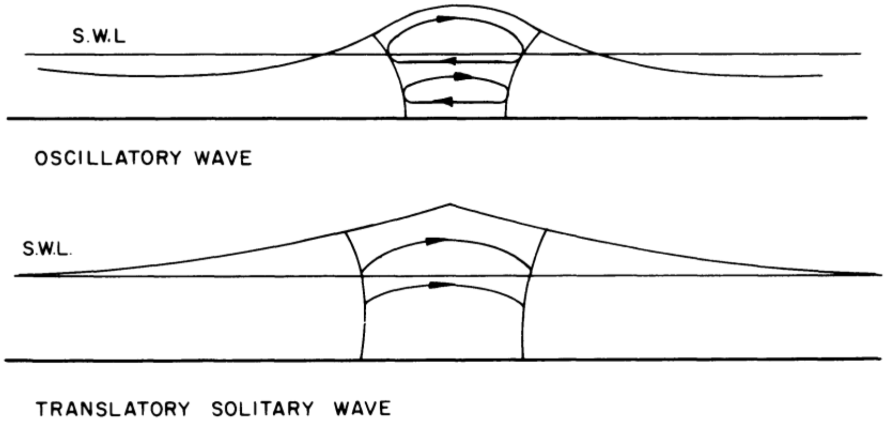

Figure 2.2 – Difference between an oscillatory wave and a translatory wave (Le Méhauté, 1976).

## 2.4.2 Non-linearity criteria

The non-linearity of waves refers to the deviation from a pure linear (sinusoidal) shape in terms of skewness and asymmetry of the water profile. Generally, impulse waves show both skewness and asymmetrical features in their profiles. The three following criteria are generally used to characterize the non linearity of a water wave : First, the ratio between the wave amplitude ($a_1^c$) and the wave height. Second, the Ursell number $Ur = H_1 L_1^2 / h_0^3$ and third, the wave steepness $H_1/L_1$.

In the literature, usually, the leading wave generated by granular landslide exceed the linearity limit no matter the criterion retained (Heller and Hager (2011), Fritz et al. (2004) and Sarlin et al. (2021)) The trailing waves, in the near-field, are usually non-linear but they can turn to linear in the far field, due to the amplitude decay and dispersion effects (Mohammed and Fritz, 2012).

$a^c/H$ value ranges from 0.5 for a linear wave to 1 for a solitary wave (note that in most cases, the leading wave crest amplitude is much higher than the wave trough one ($a^t \approx 0$ (Huber, 1980)). Based on Huber (1980) and Zweifel et al. (2006), the following classification is proposed:

$$\begin{array}{lc} 0.4 < a_1^c/H_1 \leq 0.6 & \text{weakly nonlinear} \\ 0.6 < a_1^c/H_1 \leq 0.9 & \text{moderately nonlinear} \\ 0.9 < a_1^c/H_1 \leq 1.0 & \text{strongly nonlinear} \end{array}$$

## 2.4.3 Wave breaking

For ocean waves, the breaking is generally triggered by the shallow water depth ($a^c/h_0 \approx 0.78$) or, in deeper water, by the steepness of the wave. In intermediate water, the criterion used is (Dean and Dalrymple, 1991):

$$\frac{H_{breaking}}{L_{breaking}} = 0.142\ tanh(\frac{2\ \pi\ h_{breaking}}{L_{breaking}}), \tag{2.2}$$

The "breaking" subscript indicates the wave parameters and depth at the the moment of breaking. and simply $a^c/L \approx 0.14$ in deep water.
Regardless of the reason for the wave-breaking, the maximum particle celerity at the wave crest ratio over the wave progressive celerity $U_{max}/C_1^f$ should be larger than 0.85 (Saket et al., 2017).
There is no precise breaking criterion for impulse waves over flat bottom in the literature except the $a_1^c/h_0 \approx 0.6$ limitation non-breaking waves, mentioned in Bullard et al. (2019).
There are several types of wave breaking that can occur in the ocean, each with its unique characteristics and effects. Some of the most common types of wave breaking include spilling and plunging (Figure 2.3). Spilling waves are characterized by a gradual breaking of the wave as it approaches the shore. The wave energy is dissipated slowly, resulting in a gentle transition and a less erosive effect on the shore.
In the plunging breaking, as the wave approaches shallower water, its energy becomes concentrated, causing the wave to steepen and eventually collapse forward, creating a plunging effect. The crest of the wave curls over itself, forming a tube or barrel shape before crashing forcefully into the water below. Plunging wave breakers are commonly observed in areas with steep ocean floor topography or when waves encounter a sudden change in depth (Dean and Dalrymple, 1991).

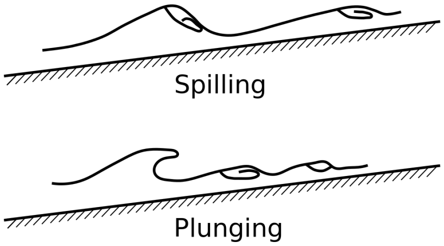

Figure 2.3 – Spilling and plunging wave breaking types (Dean and Dalrymple, 1991).

### 2.4.4 Propagation celerity

The observed travel celerity of an impulse wave can be compared with various theoretical models. The first which comes in mind would be the linear wave celerity which in shallow water goes down to $C_1^f = \frac{c_1^f}{\sqrt{g \cdot h_0}}$. A theoretical estimation of the celerity of a solitary wave is given by Laitone (1960):

$$\frac{c_1^c}{\sqrt{g\,h_0}} = 1 + \frac{a_1^c}{2h_0} \tag{2.3}$$

In this model, the wave is entirely above the still water $(H \equiv a_1^c)$
Another estimation of the solitary wave celerity is given in Russell (1844) for small relative wave crest amplitudes $(a_1^c/h_0)$) (see also Boussinesq (1872)):

$$\frac{c_1^c}{\sqrt{g\,h_0}} = \sqrt{1 + \frac{a_1^c}{h_0}} \tag{2.4}$$

Based on experimental solitary wave tests conducted by Sander and Hutter (1991), the following empirical relationship is also proposed (also found in Zweifel (2010)).

$$\frac{c_1^c}{\sqrt{g\,h_0}} = 0.95\sqrt{1+\frac{a_1^c}{h_0}} \tag{2.5}$$

Finally, an analytical formula for the celerity of a fully developed turbulent bore front is given in Hughes (1992) and Stoker (1992)):

$$c_1^f = \sqrt{\frac{g\,(a_1^c+h_0)\,(a_1^c+2h_0)}{2\,h_0}} \tag{2.6}$$

### 2.4.5 4 types of impulse waves

Previous researchers tried to classify the impulse wave types observed in their experiments. Four main classes are reported : non-linear oscillatory waves (a weakly dispersive wave train), non-linear transition waves, solitary-like waves, and dissipative transient bore (Figure 2.4). In some papers (e.g., Heller and Hager (2010b)) the terms employed are Stokes-like, cnoidal-like, solitary-like, and bore-like, respectively. Froude number, thickness of the slide at the impact point and dimensionless slide volume seem to control the apparition of a particular wave type (Fritz et al., 2004).

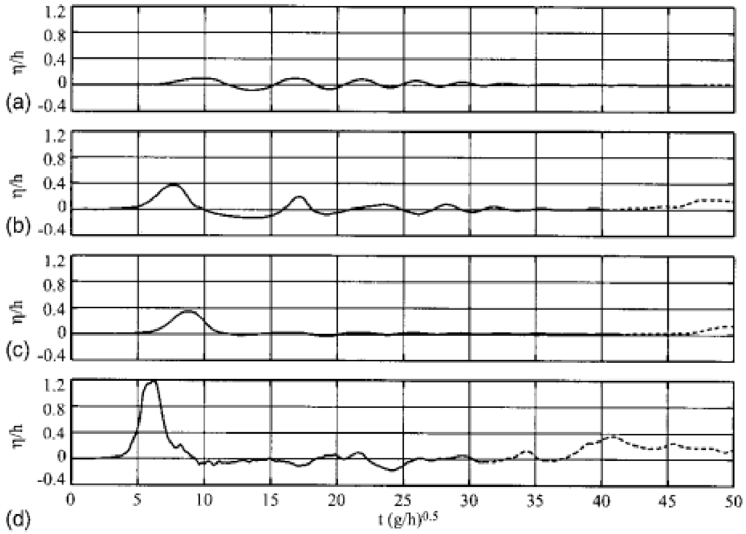

Figure 2.4 – Classes of impulse waves reported in Fritz et al. (2004) : (a) nonlinear oscillatory waves; (b) nonlinear transition waves; (c) solitary-like wave; (d) dissipative transient bore.

Nonlinear oscillatory waves are characterized by a relatively small leading wave crest followed by a dispersive oscillatory wave train. Conversely, nonlinear transition waves rather display a large leading wave crest and trough, followed by a weakly dispersive wave train. They are also characterized by a long trough separating the leading wave crest and the trailing waves. Because of dispersion and nonlinearity, the leading wave amplitude evolves during the propagation while dispersion may enhance the subsequent trailing waves. Therefore, in some cases, far away from the source region, the trailing waves may be more destructive than the leading tsunami wave.

Solitary-like waves are only identified in some experiments, involving slides with larger Froude numbers and relative slide thicknesses compared with the prior two types.
The formation of a dissipative transient bore may be observed when the leading wave crest amplitude exceed the still water depth ($a_1^c > h_0$). In the near-field, this value can be as high as 2.5 (Heller and Hager, 2010b). Unlike the solitary-like wave, the bore profile is not symmetric (steep wave front with a flat wave tail). Air entrainment is also another distinctive feature.
Table 2.1 provides a final summary of the impulse wave type characteristics based on optical measurements.

Table 2.1 – Features of the impulse wave types (Heller and Hager, 2011).

| **Stokes-like wave** | **Cnoidal-like wave** | **Solitary-like wave** | **Bore-like wave** |
|---|---|---|---|
| Wave profile symmetric (to both axes) | Wave profile symmetric (to vertical axis) | Wave profile symmetric (to vertical axis) | Irregular wave profile (to both axes) |
| Trough of identical lenght as crest | Trough longer than crest | - | Steep wavefront, flat wave tail |
| Multiple equivalent crests (at least two) | Multiple crests (at least two) | One dominant crest, Trough nearly absent ($< a_1^c/4$) | One dominant crest |
| No air transport | Small air transport | Small or no air transport | Large air transport |
| $a_1^c < h_0/2$ ($\approx$ intermediate-water) | $a_1^c < h_0$ ($\approx$ intermediate-water) | Intermediate-water | Intermediate- to shallow-water |

## 2.5 Zones definition for the leading wave

From the moment of inception by landslide impact until the end, the leading impulse wave passes through a sequence of specific zones. Classically, three zones are reported based on the physical processes, namely : the generation zone, the near-field zone and the propagation zone. In the literature, others terms also appear such as "splash zone" and "Far-field" (Heller (2007); Walder et al. (2003) and Yavari-Ramshe and Ataie-Ashtiani (2016)). In this section, we describe the different parameters that could be needed to define/locate these zones (Fig. 2.5).

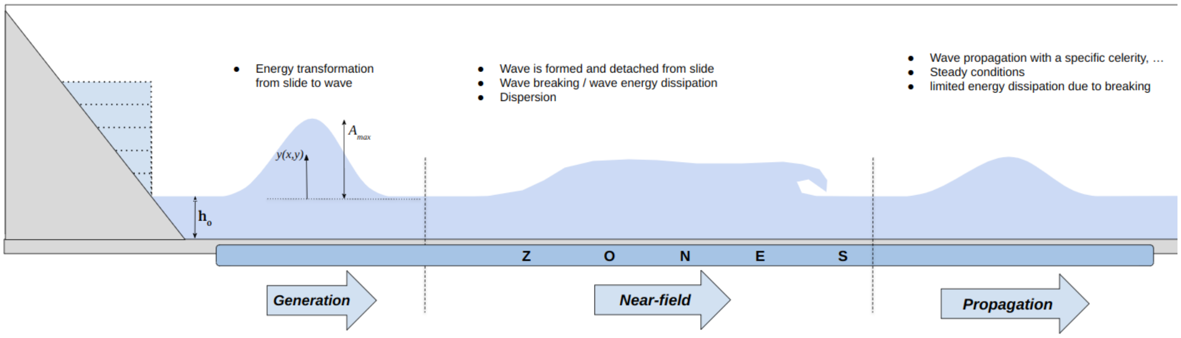

Figure 2.5 – Schematic view of generation, near-field, and propagation zones and their characteristics.

## 2.5.1 Generation zone

Once the slide impacts the still water in the basin, energy transfer begins and a wave starts to form. At this stage, there is a transfer of the slide energy to the wave. Meanwhile, different forms of energy dissipation like turbulence and bottom friction, can start to play a role (details in section 3.2.1). Wave generation in itself lasts only for a short period (Heller et al., 2016). Rauter et al. (2021) estimated that wave generation duration is limited to $\Delta t < 4\sqrt{\frac{h_0}{g}}$.

Battershill et al. (2021) numerical results state that the total energy of the water reaches a maximum at $t \approx 8\sqrt{\frac{h_0}{g}}$. In this study, the potential energy of the granular phase flattens at $t \approx 18\sqrt{\frac{h_0}{g}}$, suggesting that the grains stop imparting any energy to water at this stage.

## 2.5.2 Near-field zone

The so-called near-field zone starts when the slide stops transferring energy to the wave. At this stage, the initial wave shape should be formed, either in a non-breaking or breaking shape, and be totally detached from the slide. The leading wave energy dissipation can be significant in this stage. In the meantime, dispersion may also play a role. Therefore, we expect the majority of the wave transformations to take place in this near-field zone. This specific stage ends when the wave parameters stop evolving dramatically.

## 2.5.3 Propagation zone

In this area, the significant wave breaking ends, energy dissipation is weak and consequently, the leading wave crest is quasi-stable. It may however remain strongly non-linear and subjected to some kind of dispersion.

## 2.6 Waves generated by fluid-like landslides

As established earlier, the focus of this work is on wave generated by subaerial flow-like slide. In this section, we concentrate on the previous experimental and numerical studies on this matter.

### 2.6.1 Experimental modeling

The number of experimental studies on tsunamis generated by fluid-like slides is very limited. Because of the negligible internal shear strength, water can be considered as a limit case for high mobility slides. Following this idea, Bullard et al. (2019) carried out a set of large-scale experiments involving water slides. 4 different slide volumes (0.1-0.4 $m^3$) were released down a 6.73 $m$ long slope into a reservoir of depths varying from 0.15-0.65 $m$. The slope angle was set constant and equal to 30 degrees. The slide thickness and velocity were measured at impact using side and downward-looking high-speed cameras. Water surface elevations were measured at nine positions along the 33.8 $m$ long flume. An acoustic Doppler current profiler was used to measure the fluid velocity.

The experimental results indicate that the landslide thickness and velocity play a key role on the near-field maximum wave amplitude, the latter being relatively independent on the reservoir water depth. On the other hand, in the far-field, the maximum wave amplitude is highly dependent on the reservoir depth. The authors also found that the wave-depth ratio limit, which differentiates the breaking from the non-breaking waves, is given by the relationship $a_1^c/h_0 = 0.6$ .

Bougouin et al. (2020) conducted a series of experiments with fluidized granular slides supposed to represent pyroclastic flows. The experimental channel (dimensions: 7 m x 0.8 m x 0.2 m) was connected to an inclined plane with different slope angles but most of the results correspond to experiments performed with $\alpha = 15^\circ$. The water depth in the reservoir was varied from 13.1 $cm$ to 38.5 $cm$. The granular material used corresponds to monodisperse spherical glass beads. A few experiments were also performed with salt water. They used two high-speed cameras to record the fluidized granular flow entering water which subsequently develops into a turbidity current.

They concentrated on the wave shape in the impact region, which is primarily affected by the slide mass flux and volume. The dimensionless amplitude was related to the slide Froude number, relative thickness, relative mass, and slope angle. Testing fine fluidized granular, fine dry granular, and water flows, the authors found that the nature of the flowing material is of lesser importance in their setup. By contrast, coarse granular flows generated lower amplitude waves, which is attributed to the penetration of water into the porous granular medium.

De Lange et al. (2020) investigated the effects of debris-flow volume, composition (gravel, sand, clay, water) and slope on wave celerity and amplitude in a small-scale physical model. The latter consisted in an inclined channel that transits into a three-dimensional water reservoir with non-flat bottom. The authors found the relation between the mixture water content and wave celerity to be strong. The debris-flow velocity was also found to increase with water and clay (kaolinite) content increase (up to 22%), which both lubricate the flow. In this set of experiments, the clay volume fraction varied from 0% to 29%. However, for larger clay content (>22% vol.), the cohesive forces increase and the velocity decreases. Therefore, debris flows with a clay content of 22% vol. show an optimum in water turbulence and jumping particles, compared to flows with less or more clay.

In this experiment, they also observed that a clay cloud disperses in all directions, even if the debris flow stopped flowing and that the dispersed clay cloud can locally increase the water density and suppress the wave amplitude.

### 2.6.2 Numerical modeling

There have been numerous numerical studies on the topic of tsunamis triggered by landslides, each of them employing different methods, scales, and assumptions. This section aims to present a brief background of these earlier studies restricted to simulations involving fluid-like slides.

A few authors have used Newtonian fluids to reproduce previous granular experiments. For instance, the experiments described in Viroulet et al. (2013) were also simulated with classical one-phase VOF models in Clous and Abadie (2019), Paris et al. (2021) and Romano et al. (2023). The water flow within the grains is not replicated which may or may not be important to reproduce the wave depending on the duration of the generation zone (Clous and Abadie, 2019). For a complete description of the complex two phase flow during wave generation the reader may consult Rauter et al. (2022) and Lacaze and Kerswell (2009). Battershill et al. (2021) studied the waves generated by Pyroclastic Density Currents using the code BASILISK[2]. They compared with the experiments performed in Bougouin et al. (2020) and concluded that fluidized granular flows can be modeled with a viscous Newtonian fluid.

The experiments carried out in Bullard et al. (2019) were used for validation of the model described in Rauter et al. (2021). The latter used the multiphase interfoam solver like in the present study. The conclusions of this paper are the following. Generally, the simulation results were in good agreement with the measured experimental wave profiles. However, the replication of the slide thickness and velocity over the runout slope, remained very challenging. Applying a stricter CFL[3] condition was also inevitable for satisfying the convergence of the model. The authors finally carried out a broad parametric analysis on $a^c_{1,max}$ in comparison with the empirical scaling relations provided in section 2.3. In this analysis, the slide parameters considered were velocity, thickness, slope angle and the water depth in the reservoir. They found that the maximum wave amplitude can be well estimated based on the landslide mass. In contrast to that, the water depth plays a key role in determining the final leading wave amplitude (after propagation). The Bullard et al. (2019) study served as inspiration for our work in many aspects, given the similarity of the water slide and the numerical method employed.

Previous investigations on the rheology effect on the generated waves are rare. They are rather limited to submerged landslides. We may cite Skvortsov and Bornhold (2007) who used a shallow water model with a Bingham visco-plastic fluid to model the generated tsunami. This study was applied to the underwater landslide that occurred in Canada in 1975.

Reid and Mooney (2023) also simulated waves generated by an underwater landslide following the Herschel-Bulkley law with a depth-averaged model.

## 2.7 Slide to water energy conversion efficiency

During slide impact, the energy from the slide is transformed into various forms, including energy transferred to the water body, internal slide friction, slide deformation, and mechanical deformation of the channel bottom (Heller, 2007). This section focuses on the conversion of the slide energy to the wave energy $E_{w,tot} = E_{w,pot} + E_{w,kin}$. The current understanding of the transfer of energy between slide and waves are still very limited and inconclusive, partly due to the wide range of conditions studied.

The efficiency is the ratio between the wave energy ($E_{w,tot}$) to the slide initial energy ($E_{s,tot}$). It can be expressed at different times (e.g., when the wave energy is maximum or at the end of the channel). Given the importance of this question in our work, we tried to give a comprehensive review of the previous studies.

### 2.7.1 Experimental studies

They are mostly related to granular material slides. In many cases, the slide energy was assumed to be the kinetic energy at impact :

---

[2] basilisk.fr

[3] Courant-Friedrichs-Lewy

$$E_{s,kin} = \frac{1}{2}\rho_s v_0 {v_s}^2 \tag{2.7}$$

Where $\rho_s$ is the bulk density of the slide, $v_0$ is the landslide volume and $v_s$ is the landslide velocity at impact.
Two approaches are usually followed to calculate the wave energy. In the first one, the wave potential energy is assessed by (Mohammed and Fritz, 2012):

$$E_{w,pot} = \frac{1}{2}\,\rho_w\; g\; c \int_0^{t_1} \eta(t)^2\, dt \tag{2.8}$$

Where $\eta$ represents the free surface measured at a particular wave gauge position. $c$ is the wave celerity commonly estimated with linear shallow water approximation ($c = \sqrt{g \cdot h_0}$) (Mohammed and Fritz, 2012). Since there is usually no data about the water particles motion in the water column, the wave kinetic energy estimation is based on the equi-partition assumption of linear water wave theory (i.e., $E_{w,pot} = E_{w,kin}$). Kamphuis and Bowering (1970), Huber (1980), Fritz (2002) are some examples using this approach.
This method has two main flaws. First, the shallow water depth celerity assumption may not be accurate. Second, the impulse waves are mostly non-linear (see section 2.4.2), and the potential and kinetic energy components are therefore not equal. In breaking conditions, this equilibrium may not be respected at all (Williams, 1985; Iafrati, 2011; Deike et al., 2015).
The flow velocity field may be obtained with more advanced techniques like Particle Image Velocimetry (PIV). This alternative approach is for instance employed in Heller (2007) and Heller et al. (2016). The wave potential energy is here calculated using the water free surface recorded in an observation window (x: 0-8$h_0$; y: -$h_0$ - $\eta$) with CCD cameras following:

$$E_{w,pot} = \frac{1}{2}\,\rho_w\; g \int_0^{8h_0} \eta(x)^2\, dx \tag{2.9}$$

While the wave kinetic energy is :

$$E_{w,kin} = \frac{1}{2}\,\rho_w \int_0^{8h_0} \int_{-h_0}^{\eta} (v_{px}^2 + v_{py}^2)\, dy\, dx \tag{2.10}$$

where $v_{px}, v_{py}$ are the measured particle velocity components in the x and the y-direction, respectively. In one out of 26 examinations, the kinetic wave energy $E_{w,kin}$ exceeded the potential wave energy $E_{w,pot}$. The authors also reported ratio $E_{w,pot}/E_{w,kin}$ of $\approx 2$, far from the usual linear assumption.
Energy conversion efficiency varies widely depending on the experimental conditions. Values between 11.3% and 85.7% were reported in Heller (2007). In the same study, larger slide Froude numbers led to less effective energy conversion. Fritz et al. (2004) reported values between 4% and 50%, Huber (1980) between 1% and 40% and Kamphuis and Bowering (1970) between 10% and 50%. Wiegel et al. (1970) estimated this ratio to only about 2% in their study of the Lituya Bay case.

### 2.7.2 Numerical studies

In contrast to experiments, numerical models allow a direct access to the velocity field in the whole domain. It also allow the complete monitoring of the different energies evolution in time. Unlike in experimental studies, in numerical investigations, the energy conversion efficiency is generally calculated based on the initial slide energy $E_{s,pot}$ at t = 0 s.

Clous and Abadie (2019) calculated the time evolution of the different phases energy components with the THETIS[4] code in a set-up similar to Viroulet et al. (2013). The energy transferred to surface waves represented only 4 % of the initial slide energy.

Battershill et al. (2021) describe the wave energy components evolution for different boundary conditions and slide viscosities. The authors observed that the total energy of the water reaches a maximum at time $t \cdot \sqrt{\frac{g}{h_0}} \cong 10$ after impact. The maximum ratio between wave energy and initial slide energy was found limited to 40%.

To conclude this review, we provide in table 2.2 a summary of the energy conversion reported in the previous studies. As it can be remarked, the data covers a wide range of values depending on the case conditions.

Table 2.2 – Energy conversion rate from slide energy to wave energy in subaerial cases.

| **Study** | **Model type** | $\frac{E_{w,tot}}{E_{s,kin}}$ | Consideration |
|---|---|---|---|
| Kamphuis and Bowering (1970) | 2D physical model- Block | 10–50% | - |
| Wiegel et al. (1970) | Lituya Bay case | 2% * | * Ratio of initial potential energy of slide. |
| Huber (1980) | 2D physical model - granular slide | 1–40% | - |
| Fritz et al. (2004) | 2D physical model - granular slide | 4–50% | 2–30% is for leading wave |
| Heller (2007) | 2D physical model- granular slide | 11.3–85.7% | $0.09 \leq \frac{E_{w,pot}}{E_{s,kin}} \leq 0.58$ |
| Ataie-Ashtiani and Nik-Khah (2008) | 2D physical model- Block | 5–50% | - |
| Mohammed and Fritz (2012) | 3D physical model - gravel slide | 1-15% | 0.5–3% is for leading wave |
| McFall and Fritz (2016) | 3D physical model - cobble slide | 1-24% | 0.5–11% is for leading wave |
| Han et al. (2022) | 3D physical model - rock slide | 1-18% | 0.5–7% is for leading wave |
| Xu and Dong (2021) | 3D numerical model - SPH-DEM | 2.5-20%** | ** Based on Mohammed and Fritz (2012) experiment |
| Clous and Abadie (2019) | 2D numerical model - Newtonian fluid | 4% * | * Ratio of initial potential energy of slide. |
| Battershill et al. (2021) | 2D numerical model - Newtonian fluid | ≈ 40%* | * Ratio of initial potential energy of slide. |
| Ward and Asphaug (2003) | numerical model | 9.4% | for a hypothetical asteroid impact. |

---

[4] A Navier-Stokes VOF model tool developed at the University of Bordeaux.

## 2.8 Landslide classifications and physics

So far, the previous sections have mainly focused on the characteristics of the wave generated by the impact of the landslide mass. Our work also aims to investigate the effect of intrinsic slide characteristics that can control the landslide motion. Therefore, the following sections are dedicated to introducing the classifications and rheological behavior of landslides.

### 2.8.1 Classification of sediment-water gravitational flows

Different landslide classification systems have been introduced in the literature over the last few decades with a few inconsistencies and inaccuracies between them sometimes leading to ambiguity.
Li and Mo (2019) provides a summary of different major landslide classifications based on different characteristics of :

(a) Type of movement:
(Stepped slides/Slide/Slideflow/Fall/etc.);

(b) Location of slide surface:
(Intra-loess (through loess)/loess-bedrock (through loess and along bedrock interface, along a bedding plane, or cutting through bedrock));

(c) Movement Controlling:
(Erosion-induced/Loess–bedrock interface/Crack-controlled/Induced by stress changes, crack development, irrigation and rainfall, and a combination of these);

(d) Type of material:
(Intra-loess/Loess-clay interface/Clay-sandstone interface/Loess debris-flow/Intra-loess slide/Loess flowslide/etc.);
(Loess/loess-other soil layers/Loess - soft rock/Loess - hard rock);

(e) Shape of rupture:
(Rotational/planar);

(f) Depth of rupture:
(shallow/medium deep/Extremely deep);

(g) Velocity:
(Extremely slow/Very slow/Slow/Moderate/Fast/Very fast/Extremely fast);

(h) Volume:
(Small/Medium/Large/Extremely large);

(i) Initiation location:
(Progressive [5]/Retrograde[6]);

(j) Environment:
(Natural/Man-made);

(k) Age:
(Ancient/Old/Recent/Present day);

---

[5] sliding above, loading onto the lower reaches.

[6] sliding below, removing support from the upper reaches.

The comprehensive categorization of the landslide process by Varnes (1978) includes falling, toppling, sliding, spreading, and flowing, all of which are contingent upon causal effects and slope characteristics. The hazard associated with landslides increases with higher fluid velocity. Cruden and Varnes (1996) proposed a classification based on the velocity of landslide movement. According to this classification, slide velocity ranges from <15 $mm$ per year for extremely slow movements to more than 5 $m/s$ for extremely rapid ones. While we address many categorization types in this section, our primary focus is on classifications of flow-like landslides. Pierson et al. (1987) introduced a classification based on two primary parameters: the deformation rate and the sediment concentration, providing a more quantitative and physically relevant approach. They classified water-sediment mixtures into two main groups, namely "Apparent liquid flows" and "flows of plastic fluids", based on their rheologic response to the shear stress. The colored zones in the presented schematic chart (Fig. 2.6) show the rheological behavior types for coarse, poorly sorted and non-cohesive mixture particles. An apparent liquid flow is a diluted sediment-water flow that can be referred to as "normal stream-flow" or "hyper-concentrated stream-flow". The streamflow is still unaffected by the presence of sediment, due to its small concentration. It can therefore be considered as a Newtonian fluid. A stream with sediment concentration between 20 to 60 percent by volume, can be categorized as hyper-concentrated streamflow. Due to the increasing sediment particle interaction, the damping of the turbulence is noticeable. This flow is slightly plastic and therefore exhibits a non-Newtonian behavior (Pierson et al., 1987).

Two types of plastic fluids are included in Pierson et al. (1987) classification: "Slurry flow" and "Granular flow".
A "Slurry flow" exhibits a plastic behavior. The mixture is saturated and the pore water transports the flowing granular mass. The entrained air part is most likely only a few percent of the total volume. In the case of high content of fine materials (silt-clay) or low water content, viscosity can control the flow behavior. In some conditions, viscous forces are supplanted by inertial forces wherein momentum is transferred through particle collisions. This happens when the velocity is coarsely larger than 2 $m/s$.
The "granular flow" term is adopted when the grain concentration is high and, therefore, bulk behavior is largely governed by frequent interparticle forces, namely friction and collision (boundary C in Figure 2.6). In this case, the full weight of the flowing granular mass is endured by grain-to-grain contact or collisions. The mixture may be partly dried with air filling some space between pores. For this type of flow, the "Liquidity Index" is less than 1.
At low shear rates, the inertial effects are negligible and viscous effects determine the general shear stress. At moderate shear rates, grain inertial effects begin to dominate, but frictional effects are still significant. For high velocity such as avalanches, frictional effects are minimal.

The classification of Pierson et al. (1987) provides another view angle based on rheological boundaries for a better understanding of the geomorphological processes. The vocabulary used is very similar to the previous classification. "Streamflow", "Hyper-concentrated", "Debris flow" and "Earth flow/grain flow" are the terms employed. Streamflow and Hyper-concentrated flow, both act as a liquid flow but Hyper-concentrated flow exhibits a plastic behavior to some extent.
Both classifications of the water-sediment mixture are presented in Figure 2.6.
Debris flow is a term for slurry flow with both inertial and viscous varieties. It should be seen as an intermediate phenomenon between hyper-concentrated flows and earthflow types. In debris flows, the fundamental rheological property is the yield stress. Debris flows can also have sharp transition behavior of some physical parameters (e.g. celerity, deposit nature, and flow type).
Debris flows and normal, or hyper-concentrated flows, have differences in terms of *"Transient nature"*, *"Number of phases"*, *"Deposit structures"*[7] and *"Solid fraction range"*. Moreover, in comparison to landslide or debris avalanches, debris flows are distinguishable by *"Velocity of flow"*, *"Motion type"*

---

[7] The grain size distribution of the slide mass after the slide stops.

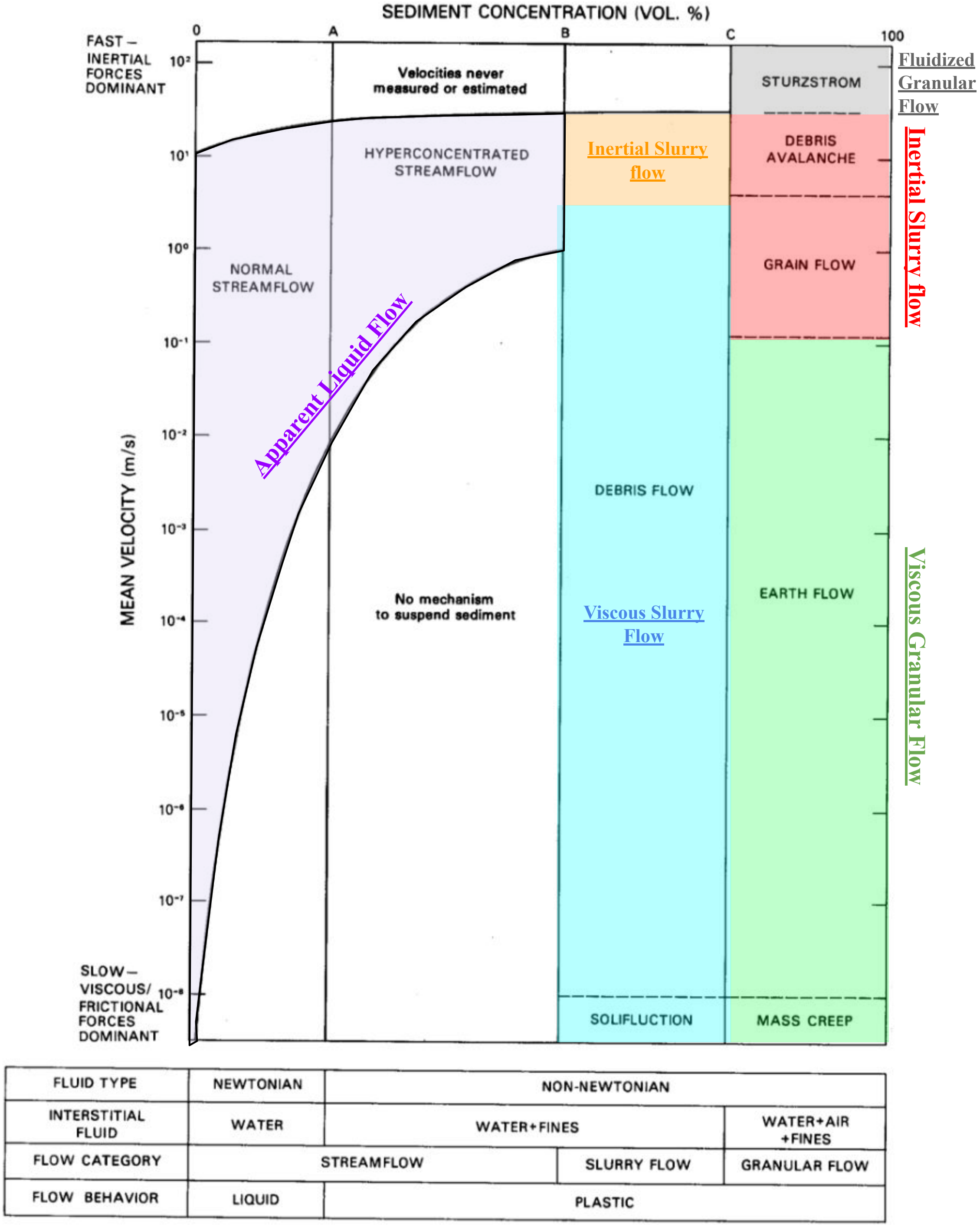

| | | | | |
|---|---|---|---|---|
| FLUID TYPE | NEWTONIAN | NON-NEWTONIAN | | |
| INTERSTITIAL FLUID | WATER | WATER+FINES | | WATER+AIR +FINES |
| FLOW CATEGORY | STREAMFLOW | | SLURRY FLOW | GRANULAR FLOW |
| FLOW BEHAVIOR | LIQUID | PLASTIC | | |

Figure 2.6 – Sediment-water flows classification (adopted from Pierson et al. (1987)). From left to right, boundary A marks the onset of the yield stress; boundary B is a sudden rapid increase in yield stress; and boundary C is the end of the liquefaction behavior.

and *"Depositing aspect"*[8].

The flow debris types in Coussot and Meunier (1996) are thus distinguished: "muddy debris flows" for the flows with large enough fine fraction, and "granular debris flows", where low fine particle fraction is sufficient to grain contacts play a major role in its bulk behavior.

In few alternative classifications of the literature, the term "debris flow" may not necessarily align with the explanation provided earlier. For example in Dasgupta (2003) which is based on Middleton and Hampton (1973), the under-water sediment gravity flow is divided into four distinct types: (i) Turbidity current; (ii) Fluidized sediment flow; (iii) Grain flow, and (iiii) Debris flow.

To sum up this section, we present (Fig. 2.7) the diagram proposed in Yavari-Ramshe and Ataie-Ashtiani (2016) based on the classification terms from several sources. This figure does not show the previous rheological boundaries introduced in Pierson et al. (1987), but their position can be located depending on the slide travel velocity and sediment concentration. The large portion of granular materials in the debris flow leads to a two-phase (non-homogeneous) behavior on the left part of the figure. The perimeter of the present study is merely limited to the one-phase flow zone indicated in the figure.

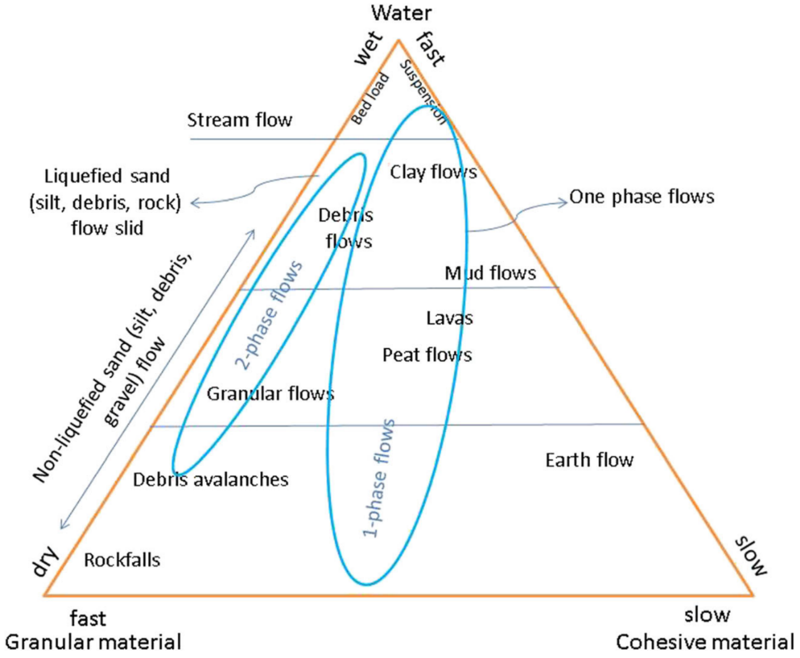

Figure 2.7 – Classification of gravitational mass movements as a function of the water content (dry-wet), velocity (slow-fast), and material type (granular-cohesive) (Yavari-Ramshe and Ataie-Ashtiani, 2016).

---

[8] This term mostly refers to the morphological features of the debris flow deposits in the channel.

## 2.8.2 Rheological behavior of landslides

### 2.8.2.1 Rheological Laws

Rheology is the study of the deformation and flow of the materials that behave somewhere between fluid and solid. Materials show a combination of elastic, viscous and plastic behavior because of their complex micro-structure level interactions. Some examples are blood, toothpaste, and paints. For the materials under an applied force the plastic deformation is more dominant than elastic behavior (Chhabra and Richardson, 1999).

Considering a thin layer of a fluid contained between two parallel planes along the x direction, for an incompressible and isotropic Newtonian fluid like water we can define a linear relation between the viscous stress with the strain rate:

$$\tau = \mu \frac{du}{dy} = \mu \dot{\gamma}_{yx} \tag{2.11}$$

Where $\tau$ is the uni-directional shear stress (drag), $\mu$ is a scalar constant of proportionality, the shear viscosity of the fluid (dynamic viscosity) and $\frac{du}{dy}$ is the velocity gradient (normal to the shear).

On the one hand, for non-Newtonian fluids, the relation between the shear stress and shear strain rate is different (Chhabra and Richardson, 1999). The viscosity in non-Newtonian fluids is not constant and depends on the shear rate or time. The time independent Non-newtonian fluids behavior model is called viscoplastic as ($\tau_{yx} = f(\dot{\gamma}_{yx})$), while the type with time-dependent viscosity ($\tau_{yx} = f(\dot{\gamma}_{yx},\ t)$) is referred to as viscoelastic (Figure 2.8).

The apparent viscosity of time-dependent fluids may increase or decrease with time. There are two categories of thixotropic and rheopectic (negative thixotropy) for these types of fluids (Figure 2.8). Thixotropic fluids show shear thinning behavior and rheopectic fluids show shear thickening behavior, but they change with the kinematic history of the sample. The effect of kinematic history on viscoelastic materials is a complex subject that depends on material properties such as microstructure factor and applying force properties (such as strain rate, amplitude, frequency, and rest periods) (Chhabra and Richardson, 1999). The behavior of these materials is described with visco-elastic fluid theories which is out of the scope of this work.

Our work with rheological laws is constrained to the time-independent (viscoplastic) models. Time-independent (viscoplastic) non-Newtonian fluid categories are distinguished on the different forms of the function $f$ (Figure 2.8):

- **Shear thickening (Dilatant):** The viscosity increases with the rate of shear strain.
- **Shear thinning (Pseudoplastic):** The viscosity decreases with the rate of shear strain.
- **Bingham plastic:** It's a viscoplastic material that behaves as a rigid body at low stresses but flows as a viscous fluid above a threshold of yield stress.
- **Yield-pseudoplastic:** The relationship between shear stress and shear rate is non-linear and the fluid has yield stress before starting to flow.

### 2.8.2.2 Viscoplastic models

A viscoplastic fluid behavior has a yield stress ($\tau_0$) in which the shear stress ($\tau$) must be exceeded before the fluid will deform or flow. The parameters in the following models should be attained by experiment, so the curve-fitted values of parameters like yield stress ($\tau_0$) are not the same. Three commonly used models for viscoplastic fluids (the Bingham plastic model, the Herschel–Bulkley fluid model, and the Casson fluid model) are briefly described here.

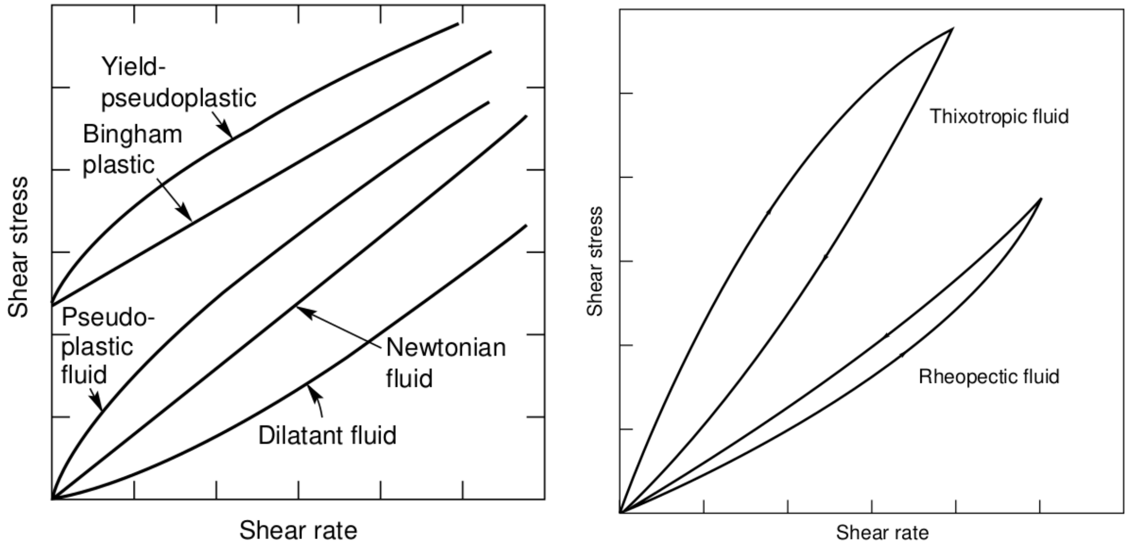

Figure 2.8 – Types of time-independent flow behavior (left); schematic shear stress –shear rate behavior for time-dependent fluid behavior (right) (Chhabra and Richardson, 1999). Shear stress and shear rate unit in SI are $N/m^2$ and $1/s$, respectively.

- **The Bingham plastic model**
  This is the simplest equation describing the flow behavior of a fluid with a yield stress and, in steady one-dimensional shear, it is written as (Chhabra and Richardson, 1999):

$$\begin{array}{ll} \tau_{yx} = \tau_0 + \mu(\dot{\gamma_{yx}}) & \text{for } |\tau_{yx}| > |\tau_0| \\ \dot{\gamma_{yx}} = 0 & \text{for } |\tau_{yx}| < |\tau_0| \end{array} \tag{2.12}$$

  $\mu$ and $\tau_0$ parameters are apparent viscosity and yield stress, respectively. The parameters are obtained by curve fitting regarding the equation (2.12) (Chhabra and Richardson, 1999).

- **The Herschel–Bulkley fluid model**
  A simple generalization of the Bingham plastic model to embrace the non-linear flow curve (for $|\tau_{yx}| > |\tau_0|$) is the three constant Herschel–Bulkley fluid model (Herschel and Bulkley, 1926). In one-dimensional steady shearing motion, the Herschel–Bulkley constitutive law is written as:

$$\begin{array}{ll} \tau_{yx} = \tau_0 + k(\dot{\gamma_{yx}})^n & \text{for } |\tau_{yx}| > |\tau_0| \\ \dot{\gamma_{yx}} = 0 & \text{for } |\tau_{yx}| < |\tau_0| \end{array} \tag{2.13}$$

  Where the $k$, $n$ are the consistency index and power-law index parameters, respectively (Chhabra and Richardson, 1999). Note that here too, the dimensions of $k$ depend upon the value of n.

  The formulation for tensor form of shear stress ($\tau_{ij}$) related to the strain rate tensor ($\dot{\gamma_{ij}}$), also can be written as (Hogg and Matson, 2009):

$$\begin{array}{ll} \tau_{ij} = (\tau_0 + k|\dot{\gamma_{ij}})|^n)\, \dot{\gamma_{ij}}/|\dot{\gamma_{ij}}| & \text{for } |\tau_{ij}| > |\tau_0| \\ \dot{\gamma_{ij}} = 0 & \text{for } |\tau_{ij}| < |\tau_0| \end{array} \tag{2.14}$$

  Here the expression $|\ \ |$ denotes the second invariant of the tensor.

- **The Casson fluid model**
  Many foodstuffs and biological materials, especially blood, are well described by this two constant model as (Chhabra and Richardson, 1999):

$$\begin{aligned} &\sqrt{|\tau_{yx}|} = \sqrt{|\tau_0|} + \sqrt{(\mu_c\,|\dot{\gamma_{yx}}|)} && \text{for } |\tau_{yx}| > |\tau_0| \\ &\dot{\gamma_{yx}} = 0 && \text{for } |\tau_{yx}| < |\tau_0| \end{aligned} \tag{2.15}$$

In common CFD models such as OpenFOAM (the model used in the present work), the classical rheological models (i.e., Herschel-Bulkley, Bird-Carreau, Cross Power Law, Power Law, Casson) are available. Customized model that allows a user to specify viscosity as a function of strain rate at run-time can also often be defined. Because in CFD employing a discontinuous behavior (solid behavior for stress below the yield stress and fluid behavior for stress above the yield stress) is not possible, a regularized model can be applied to overcome this numerical issue (Beverly and Tanner, 1992). In low strain rates, the material is modeled as a very viscous fluid with viscosity $\nu_0$. Beyond a threshold, the kinematic viscosity follows the intended rheological law in correspondence with the strain rate value (Greenshields, 2018). For example, for the Herschel-Bulkley model, the apparent viscosity acts under the following relation:

$$\nu = min\,(\nu_0, \frac{\tau_0}{\dot{\gamma}} + k\,\dot{\gamma}^{n-1}) \tag{2.16}$$

Note the units for kinematic viscosity ($\nu$) are $L^2/T$, same for $\nu_0$. The time constant parameter (fluid consistency) $k$ unit is $[L^2 \cdot T^{n-2}]$. For yield stress ($\tau_0$) the unit is $L^2/T^2$. The power law index ($n$) is unitless.

Figure 2.9 schematically demonstrates how apparent kinematic viscosity transits between solid to fluid states with varying strain rate values.

The conventional parameters of the Herschel-Bulkley model should be attained in a laboratory by rheometer apparatus. On the other hand, the regulation viscosity ($\nu_0$) is not based on exact measurements and is considered a very large arbitrary value (Rudert and Schwarze, 2009). In some references, for $\nu_0$ it is advised to choose a value about 1,000 times greater than the viscosity in the liquid regime (O'Donovan and Tanner (1984) and Schaer et al. (2018)).

#### 2.8.2.3 Rheology of Debris flow/Mud flow

As it has been mentioned in section 2.8.1, debris flow types are complex fluids that also exhibit non-Newtonian behavior. The material in debris flow may vary on a large scale in terms of clay type, grain size distribution, solid fraction, etc. By raising the fine material fraction -notably clay up to 2 $\mu m$-, the rheological parameters also significantly change, which in general dictates the non-Newtonian behavior. The structure of clay particles is radically different from that of other grains because they're microscopic sheets instead of round grains like sand. Moreover, due to their small size, water-clay particle interaction is quite different from grain-water interaction (Coussot, 1997). You can find more information about the water-clay mixture's rheological behavior in section 2.8.2.4.

Therefore mud-flows can be considered as a subclass of debris flows. The mud suspensions that flows in mountain streams after heavy rains are a typical example of mudflow. Drilling muds composed of water-bentonite mixture with oil and grains, red muds, waste materials such as sewage sludge, coal slurry, or fresh concrete paste are also described by the same mud flow rheological behavior (Coussot, 1997).

Debris flow/mud-flow occurs as a mass movement that can be triggered by changing of water content normally due to rainfall intensity. The water content is determinative in these solid-water mixtures

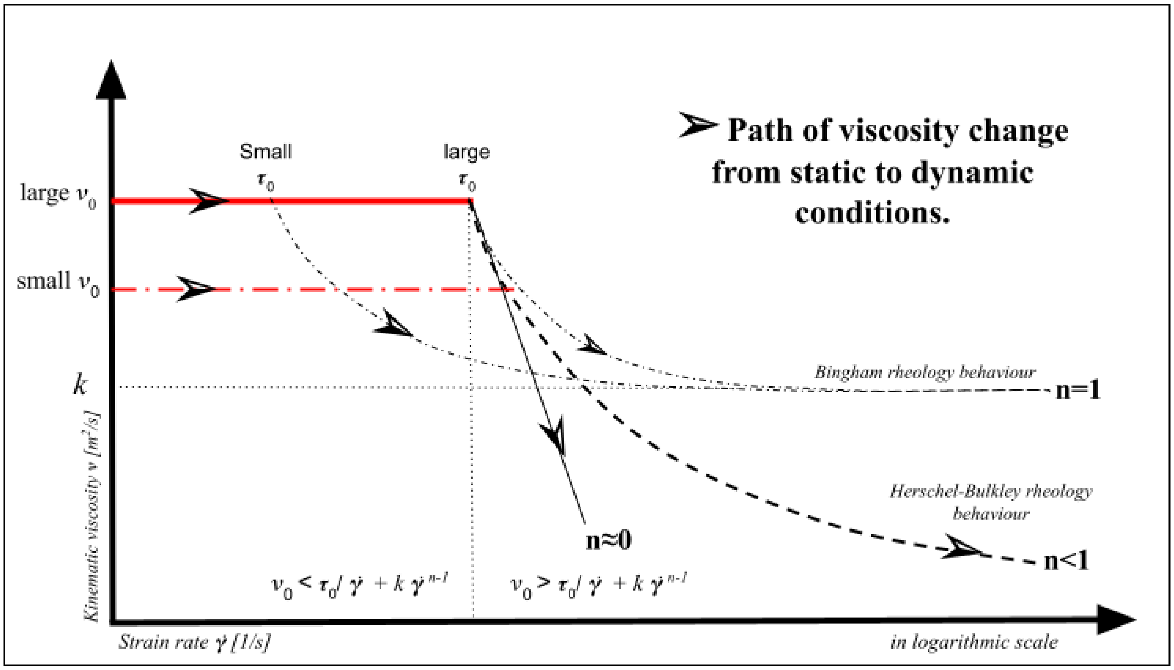

Figure 2.9 – Conceptual diagram showing how the parameters in Eq.(2.16) affect the apparent kinematic viscosity in the Herschel-Bulkley viscoplastic model in CFD models when the strain rate values change.

.

fluid's motion. Lee and Widjaja (2013) studied the rheology parameters (yield stress and viscosity) of mudflow in laboratory experiments. Their results show that mudflows (in this case for a low plasticity silt soil) initiate when the water content is equal to or higher than the liquid limit.

In debris flows the viscosity controls the fluid mobility, while the flow depth thickness during the transportation and deposition is governed by the solid concentration by volume. Typically, solid grains and intergranular liquid constitute roughly equal percentages (30-70%) of the volume of a debris flow. Rock avalanches can transform into debris flows through the entrainment of water or water-rich sediment, and debris flows that entrain additional water can become so dilute that they transform into surging floods (Iverson, 2005).

Numerous scholarly[9] inquiries have explored the rheological characteristics of debris flow and mud flow using a variety of methodologies and rheological laws. The sample compositions in these investigations vary greatly, and the procedures used for measurement vary according to the situation. Examples of these approaches include the use of viscometers, rheometers, inclined planes, falling ball and cone tests, flow-box tests, and other devices. These differences in measurement methodologies have thus led to a substantially varied range of the obtained results .

For example, a yield stress range of 65-400 [Pa] and a range of fluid consistency parameters (k) of 10-1000 [P a.sn] can be obtained for debris flow. Natural fine mud suspension flow characteristics according to Herschel-Bulkley law, are described in Coussot (1997) as a book reference.

As an example, the rheology parameters for a recent "quick clay landslide" event that happened in Gjerdrum (Norway) on, December 30, 2020, are provided. These Herschel-Bulkley model parameters are taken by correlating with consistency limits tests and are used for simulation with the model OpenFOAM in (Alene et al., 2022). Table 2.3 provides the slide rheological parameters (equation

---

[9] data about 60 different cases are provided in detail in appendix B.1

(2.13)) for this event.

Table 2.3 – Density and Herschel-Bulkley model parameters for the 2020 Norway event (Alene et al. (2022)).

| **parameters** | $\tau_0$ [Pa] | $k$ $[Pa.s^n]$ | $n$ [-] | density $[kg/m^3]$ |
|---|---|---|---|---|
| **value** | 200 | 50 | 0.34 | 2000 |

#### 2.8.2.4 Rheological behavior of water-clay mixtures

The distinctive rheological behavior observed in clay-water mixtures is attributed to the unique microstructure formed by the spatial arrangement of clay particles. Clay particles are formed up of hundreds of monolayers layered on top of one another. These monolayers are composed of a fixed mixture of silicon-oxygen tetrahedral ($SiO_2$) and aluminium-oxygen octahedral ($Al(OH)_3$) sheets. Various combinations of clay types exists, such as kaolinites, bentonites, illites, smectites (montmorillonites), chlorites, etc. Some cations ($Ca^{2+}$, $Li^+$, $K^+$, $Fe^{2+}$) absorption may happen due to excess negative charges within these lattice of mono-layers. These exchangeable cations play a key role in the microstructure and behavior of the water-clay system (Coussot, 1997).

The rheologic behavior in a mud suspension is a consequence of interaction between mud-suspension's components (water, clay particles, grains (Figure 2.10)) which in turn can split into four main interaction types: *Interaction within water, Interaction between immersed clay particles in water, Electrical interaction between grains within a clay-water suspension, and Interaction within a mud suspension* (Coussot, 1997).

For rheological tests, generally, two types of standard materials are used in laboratory experiments[10]. First type is a polymeric material base such as Carbopol (see Piau (2007)) and the second type is standard fine clay materials mixtures like Kaolinite (also referred to as Kaoline, China-clay), Bentonite, etc. In the 1990s and early 2000s, the typical material used in most experiments was kaolin, a clay suspension that usually exhibits viscoplastic properties. Compared to other clays, kaolin has an unusual behavior, partly because yield stress arises from steric interactions (jamming) between flocs rather than colloidal interactions (Ancey and Cochard, 2009).

Clay-type effects on mud behaviour have been explored in many studies (Packter (1956), Jeong et al. (2010), Widjaja et al. (2015)).

Several studies in the literature have shown that the behavior of mud appears to be particularly sensitive to criteria other than clay content.

Among them, we have,

- temperature (Coussot and Piau (1994)),
- pH (Coussot and Piau (1994); Torrance (1999)),
- electrolyte concentration (Torrance (1999); Viccione et al. (2015)),
- third force-free surface particles element like sand (Coussot and Piau (1995); Coussot et al. (1998); Parsons et al. (2001); Nguyen et al. (2018)),

Other additive components like oil (Pal et al. (1992); Hato et al. (2011)) and soil organic carbon content in natural samples (Carotenuto et al. (2015)) are among the factors that influence the mud's rheological response.

In some studies (analytical and experimental purposes) the authors described the rheological behavior of kaoline-water mixture with Bingham model (Kessel and Kranenburg (1996), Komatina and Jovanovic (1997), Huang and García (1997)).

---

[10] A table of rheological parameters in different laboratory tests is provided in appendix B.2

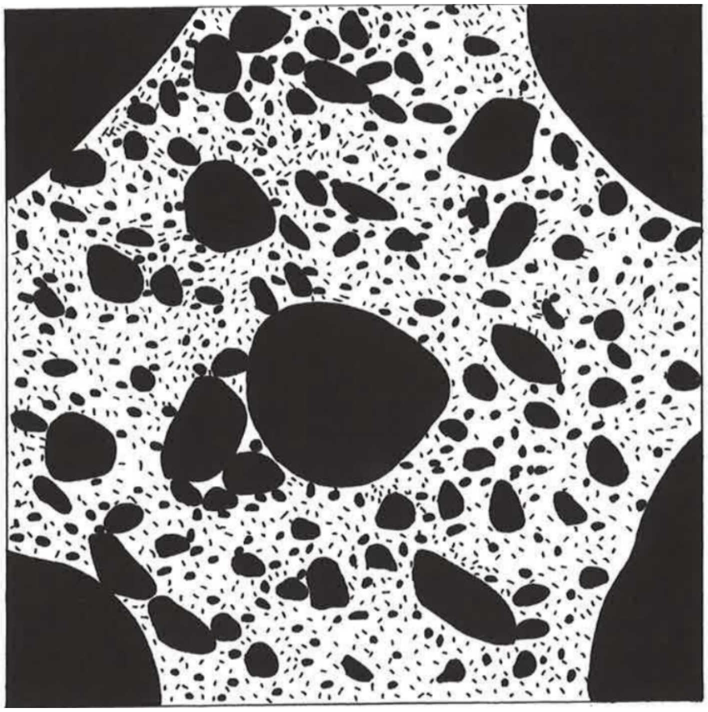

Figure 2.10 – Imaginary planar view of the internal structure of a mud suspension. Clay particles (short lines), grains (points of various areas) have been dispersed at random on the plane (water in white) with no account for any model for particle interaction. The approximate length of a side of the picture is 0.1 mm (Coussot (1997)).

O'brien and Julien (1985) and Julien and Lan (1991) used a quadratic rheological model (a modification of Bingham model with an extra $b(\frac{du}{dy})^2$ term).

It is expected that the shear rate of high-density mud sediment in natural rivers and the decelerating stage of mud-flow is bound to less than 100 ($s^{-1}$). However, a very large shear rate is expected in mudflows at the accelerating stages in mountainous areas (Huang and García (1998)).

In lower shear stress level, viscosity decreases with the increase of shear rate, so a Bingham plastic model may overestimate the true yield stress due to shear at the low shear rate, specifically for the high solid concentration that exhibits shear thinning phenomenon (Huang and García, 1998).

It is worthy of note that the shear-thinning behavior of clay-water suspensions has often been noticed in the literature (Street (1956); Weymann et al. (1973); Akae and Low (1988)).

Moreover considering that in the high shear rate range, the Bingham model result's accuracy is not enough, so since then in many works, the rheologic behavior of water-clay mixture is approached by the Herschel-Bulkley viscoplastic model (De Kee et al. (1990); Coussot (1994); Coussot and Piau (1994); Coussot and Meunier (1996); Huang and García (1998); Balmforth et al. (2007)).

Though shear-thinning is often associated with floc breakage, there is still no micro-structural theory that can even qualitatively anticipate this behavior. To compare rheological properties or predict flow behavior, the best way is to fit an empirical model to the experimental data and compare the values of the corresponding parameters (Maciel et al. (2009)).

It is worth noting that the Herschel–Bulkley model is an idealized interpretation of the viscoplastic behavior of a yield-stress fluid. So here we shall mainly focus on the rheological and flow properties of a homogeneous, viscoplastic, concentrated muddy mixture and it does not deal with natural events at all (Coussot, 1997). Other fluid features like visco-elasticity, thixotropy, aging, sedimentation, and temperature effects are neglected.

## 2.9 Identified gasps and research strategy

The domain covered by this literature review was quite vast. Our investigations show that there are still several important gaps and restrictions in our understanding of the waves generated by subaerial landslides, even though a significant research effort has already been brought to this interesting topic. In previous works, the strongest attention has been on granular slides as being representative of the real cases found in nature. While this is, without a doubt, a trail to follow, this presents the disadvantage to concentrate all the efforts on the generation phase, as solving this problem is already a huge challenge in this case. This is likely the reason why, most of the authors have concentrated their efforts to the estimation of the wave characteristics right after wave generation. Nevertheless, by focusing on this particular stage, the authors ignored the complex transformations that the wave can subsequently experience, such as breaking or dispersion. Accounting for these processes may be critical to improve the accuracy of the hazard assessment. The literature review also showed the scarcity of the results concerning the energy transfers and the interest of using numerical models in this context.

Finally, our investigations of the landslides classification and rheology illustrated the great complexity of the topic. Due to this and as far as wave generation is concerned, it seems that a gradual approach starting from very simple cases and progressively increase the complexity of the rheology may be a valuable strategy to improve our understanding of the topic.

According to our previous comments, we propose a research strategy organized around two axes of investigation (figure 2.11):

1. The first axis, the x-axis, aims to gain comprehensive knowledge of every aspect of the impulse wave transformation, from the moment of generation to the end of the propagation stage with a focus on the energetic processes. This step is conducted in a so-called "phase I" with a reduced complexity of the slide rheology (i.e., a water slide).

2. The second axis, the y-axis, intends to study the effect of slide rheology, governing the slide deformation, as well as the initial elevation effect, both on the wave generation. Here, we progressively increase the complexity of the rheological models in several phases, the last one, also including the submergence effect.
3. Finally, the investigations conducted in both axis will allow to generate an interesting dataset that we propose to analyze in more global way in the last stage of this work.

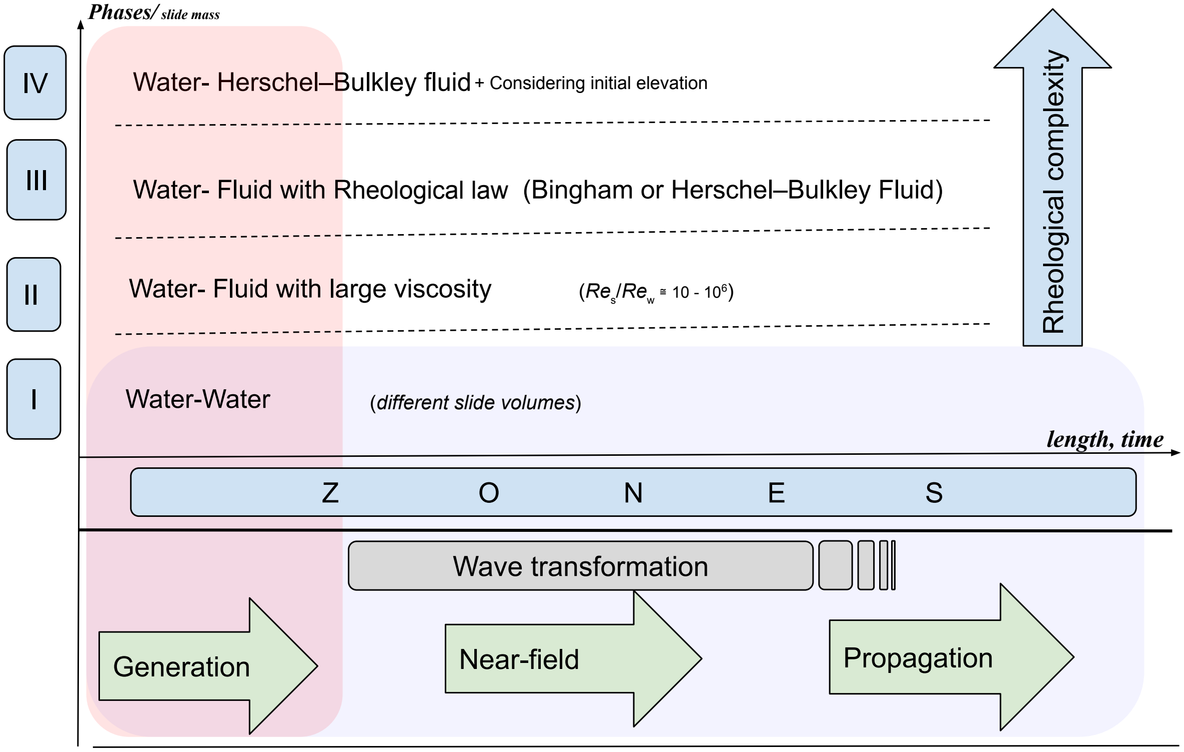

Figure 2.11 – Thesis research strategy.

# Chapter 3

# Methodology

---

This section presents the different aspects of the numerical model used in this work as well as its governing equations, validation, and the post-processing procedures including the computations of the energy components.

## 3.1 Numerical methods

### 3.1.1 `OpenFoam`

- General
  The Open Source Field Operation and Manipulation (OpenFOAM$^{®}$) is a collection of a hundred of C++ libraries of solvers and utilities. These solvers are customized for various purposes in computational fluid dynamics applications. This open-source CFD software has been developed by OpenCFD Ltd since 2004. OpenFoam is meant to address a wide range of incompressible/compressible, unsteady flows, laminar or turbulent thermophysical, and multiphase flows.

- Multiphase solvers
  Depending on the problem considered, multiphase modeling can be implemented with two different Euler-Euler approaches. First, the Dispersed-Continuous (Mixture Models) approach is adopted to simulate dispersed fluids (gas(bubbles)). In this method, the solver (`twoPhaseEulerfoam` in OpenFoam) solves separate equations for both phases i.e. dispersed phase and continuous phase (Rusche, 2002).

  The other approach is the Continuous-Continuous formulation like the volume of fluid method (VOF). It is adapted to describe two incompressible, isothermal immiscible fluids with sharp interfaces.

  The material properties are constant in the region filled by one of the two fluids except at the interface.

The VOF formulation relies on the fact that the boundary between the phases is well-defined. Typical applications of the VOF model include stratified flows, free-surface flows, filling, sloshing, motion of large bubbles in a liquid, the prediction of jet breakup (surface tension), and the tracking of any liquid-gas interfaces. In this work, depending on the problem case, two-phase and multi-phase VOF solvers (`InterFoam` or `multiphaseInterfoam`) will be used. In VOF model a single set of mixture momentum and energy equations is shared by all the phases and solved implicitly (Hirt and Nichols (1981); Jasak (1996); Ubbink (1997)).

In addition to the continuity Equation and momentum Equation, and to track, at each time step, the location of the interface between the two fluids, an equation for phase fraction ($\alpha_i$) has to be solved. The phase-fraction for phase $i$ is a scalar field defined as follows:

$$\alpha_i(x,t) = \begin{cases} 1 & \text{if phase } i \text{ is present at } \ x,t \\ 0 & else. \end{cases} \tag{3.1}$$

The phase volume fractions equation is solved with accurate explicit or semi-implicit time algorithms with higher-order advection schemes to ensure a sharp interfaces between each pair of phases. The `multiphaseInterFoam` solver MULES[1] is the default algorithm for solving the phase fraction equations.

- Governing equations solved in `InterFoam` and `multiphaseInterfoam`:

For incompressible flows, the continuity equation reads:

$$\nabla \cdot \mathbf{u} = 0. \tag{3.2}$$

where $\mathbf{u}$ is the velocity, The momentum equation reads:

$$\frac{\partial \rho \mathbf{u}}{\partial t} + \nabla \cdot (\rho \mathbf{u}\mathbf{u}) = -\nabla \mathbf{p} + \nabla \cdot (2(\mu + \mu_t)\mathbf{D}) + \rho \mathbf{g} + f_{\sigma i}. \tag{3.3}$$

Here, $\mathbf{g}$ is the gravitational acceleration, $\mathbf{p}(x,t)$ the pressure field, and $\rho(x,t)$, $\mu(x,t)$ and $\mu_t$ are the local fluid density, molecular dynamic viscosity and turbulent (eddy) viscosity (see section 3.1.2), respectively.

As there are several phases, the local fluid properties are averaged among the existing phases in a computational cell.

$$\rho(x,t) = \sum_{i}^{No.\ phases} \alpha_i(x,t)\ \rho_i, \tag{3.4}$$

$$\mu(x,t) = \sum_{i}^{No.\ phases} \alpha_i(x,t)\ \mu_i. \tag{3.5}$$

Here $\rho_i$ and $\mu_i$ are the density and molecular dynamic viscosity of an existing phase in a cell.

$\mathbf{D}$ is the strain rate tensor:

$$\mathbf{D} = \frac{1}{2}(\nabla \mathbf{u} + (\nabla \mathbf{u})^T). \tag{3.6}$$

---

[1] Multidimensional Universal Limited Explicit Solver

The scalar strain rate field ($\dot{\gamma}$ ) is the second invariant ($I_2$ ) of the strain rate tensor. This quantity is an important in turbulence models and rheological aspects and is calculated by the following relationship:

$$\dot{\gamma} = \sqrt{2\mathbf{D} : \mathbf{D}} = \sqrt{2\sum_{i=1}^{3}\sum_{j=1}^{3}\mathbf{D}_{ij}\mathbf{D}_{ij}} \tag{3.7}$$

$f_{\sigma i}$ is the surface tension which is modeled as continuum surface force as follows (Heyns and Oxtoby, 2014):

$$f_{\sigma i} = \sigma\,\kappa\,\nabla\alpha_i. \tag{3.8}$$

in which $\sigma$ is surface tension at the interface (e.g. the default value is 0.07 ($kg.s^{-2}$) for water-air interface) and $\kappa$ is the local curvature of the interface (Brackbill et al., 1992).

The phase fraction values is updated at each time step thanks to the phase fraction advection equation given by:

$$\frac{\partial\alpha_i}{\partial t} + \nabla.(\alpha_i\mathbf{u}) + \sum_{j}^{adjacent\,cells}\nabla\cdot(\alpha_i\alpha_j u_{r,ij}) = 0. \tag{3.9}$$

Here $u_{r,ij}$ is the relative velocity between phases. The last term is employed as a numerical technique to ensure a sharp and non-diffusive interface. Since in any given control volume cell, the sum of the volume fractions for all phases is always equal to 1 ($\sum_{i=1}^{N}\alpha_i = 1$), thus for N phases, only N-1 volume fraction equations are solved.

- Numerical solutions and stability:
  The time and space computational domain is discretized into a finite number of timesteps and cells to solve the governing equations. Spatial discretization is the standard Gaussian finite-volume integration method that is based on summing values on cell faces, which must be interpolated from cell centers (Greenshields, 2018). The equations are solved in-time a marching manner within the PIMPLE algorithm that combines the PISO (Pressure Implicit with Splitting of Operators) and SIMPLE (Semi-Implicit Method for Pressure-Linked Equations) original algorithms. This algorithm ensures the pressure-velocity coupling. The Courant number field (CFL number) dictates the stability of solution by limitation time step duration $\Delta t$. Theoretically, the CFL value must be equal or smaller than one. The CFL number for a uniform grid size $\Delta x$ can be stated as follows:

$$CFL_{conv} = \frac{|\mathbf{u}|\,\Delta t}{\Delta x} \tag{3.10}$$

Where CFL$_{conv}$ number represents the stability condition related with respect with the convective terms.

Generally for flow velocities around 10 $m \cdot s^{-1}$, the contribution of viscosity to numerical instabilities of the equations is only relevant for very fine mesh sizes ($\Delta x < 10^{-6}$ m) (Rauter et al., 2021). Therefore the diffusive CFL condition is often neglected in many CFD codes such as OpenFoam. Nevertheless in certain conditions like high viscosity values in landslides (considering molecular viscosity and eddy viscosity), flows with low particle velocities (e.g. surface waves), very fine cell sizes and high turbulence, a more restrictive condition than the convective CFL condition should be respected (Rauter et al., 2021). The CFL$_{diff}$ number for such a case is:

$$CFL_{diff} = \frac{(\mu + \mu_t)\,\Delta t}{\rho\,\Delta x^2} \tag{3.11}$$

Rauter et al. (2021) limited the CFL$_{diff}$ to 1. In Moukalled et al. (2016), CFL$_{diff}$ is equal to 0.5. In section 3.4.2.1 we will show that the constraint CFL$_{diff}$<1 is respected by strongly limiting CFL$_{conv}$.

### 3.1.2 Turbulence models

#### 3.1.2.1 Reynolds Averaged Navier Stokes equations

Let the $\phi$ parameter represent, at time $t$ and position $x$, the instantaneous value of any of the flow variables i.e. ($\mathbf{u}$, p, $\rho$, etc.). Then as shown in Figure 3.1, $\phi$ can be decomposed into a mean value component $\bar{\phi}(\mathbf{x}, t)$ and a fluctuating component $\phi'(\mathbf{x}, t)$ such that:

$$\phi(\mathbf{x}, t) = \bar{\phi}(\mathbf{x}, t) + \phi'(\mathbf{x}, t). \tag{3.12}$$

The mean value $\bar{\phi}$ is being computed by a Reynolds averaging technique (Moukalled et al., 2016). The velocity field in the computation domain in (i, j, k) Cartesian coordinates is written as below:

$$\mathbf{u}(\mathbf{x}, t) = \bar{\mathbf{u}}(\mathbf{x}, t) + \mathbf{u}'(\mathbf{x}, t), \tag{3.13}$$

with

$$\bar{\mathbf{u}} = \bar{U}\mathbf{i} + \bar{V}\mathbf{j} + \bar{W}\mathbf{k}, \tag{3.14}$$

and

$$\mathbf{u}' = U'\mathbf{i} + V'\mathbf{j} + W'\mathbf{k}, \tag{3.15}$$

Introducing this formulation into Navier-Stokes equation leads to the appearance of a new term into equation: the Reynolds averaged stress tensor $\boldsymbol{\tau}^{\boldsymbol{R}}$ (Moukalled et al., 2016). This tensor reads as follows:

$$\boldsymbol{\tau}^{\boldsymbol{R}} = \rho\overline{\mathbf{u}'\mathbf{u}'} = \rho \begin{pmatrix} \overline{U'U'} & \overline{U'V'} & \overline{U'W'} \\ \overline{U'V'} & \overline{V'V'} & \overline{V'W'} \\ \overline{U'W'} & \overline{V'W'} & \overline{V'W'} \end{pmatrix}, \tag{3.16}$$

Based on the Boussinesq hypothesis (Boussinesq (1877)) it is assumed that for a Newtonian fluid, Reynolds stress is a linear function of the mean velocity gradients, leading to:

$$\boldsymbol{\tau}^{\boldsymbol{R}} = \underbrace{\frac{2}{3}\,[\rho k \,+\, \mu_t(\nabla\cdot\mathbf{u})]\,\mathbf{I} - \mu_t\,2\,\mathbf{D}}_{\text{a Newtonian fluid}} = \underbrace{\frac{2}{3}\,\rho\,k\,\mathbf{I} - \mu_t\,2\,\mathbf{D}}_{\text{a Newtonian fluid and incompressible flow}} \tag{3.17}$$

Here $k$ is the turbulent kinetic energy defined as:

$$k = \frac{1}{2}\overline{\mathbf{u}'\cdot\mathbf{u}'}, \tag{3.18}$$

In eq. (3.17), $\mu_t$ is the turbulent eddy viscosity (analogy to the molecular viscosity $\mu$), which is flow-dependent.
Another important parameter in these two-equations turbulence models is the rate of dissipation of the turbulent kinetic energy per unit mass ($\epsilon$) given by:

$$\epsilon = \frac{1}{2}\,\frac{\mu}{\rho}\,\overline{[\nabla\mathbf{u}' + (\nabla\mathbf{u}')^T] : [\nabla\mathbf{u}' + (\nabla\mathbf{u}')^T]}. \tag{3.19}$$

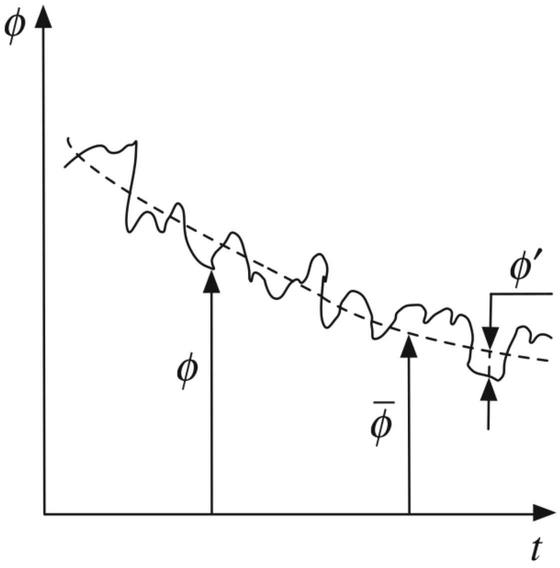

Figure 3.1 – Fluctuating and mean variable components (Moukalled et al., 2016).

#### 3.1.2.2 Standard k-$\epsilon$ model

In this model, the eddy viscosity $\mu_t(x,t)$ is calculated as follows:

$$\mu_t = \rho\, C_\mu \frac{k^2}{\epsilon}. \tag{3.20}$$

The governing equations for the $k$ and $\epsilon$ are:

$$\frac{\partial \rho\, k}{\partial t} + \nabla \cdot (\rho\, k\, \mathbf{u}) = \nabla \cdot \left( \left( \frac{\mu_t}{\sigma_k} + \mu \right) \nabla k \right) + P_k - \rho \epsilon, \tag{3.21}$$

$$\frac{\partial \rho\, \epsilon}{\partial t} + \nabla \cdot (\rho\, \epsilon\, \mathbf{u}) = \nabla \cdot \left( \left( \frac{\mu_t}{\sigma_\epsilon} + \mu \right) \nabla \epsilon \right) + \frac{C_{1\epsilon}\, \epsilon}{k} P_k - \frac{\rho\, C_{2\epsilon}\, \epsilon^2}{k}. \tag{3.22}$$

Where $P_k$ is the production of the turbulent energy term, with:

$$P_k = \boldsymbol{\tau}^{\boldsymbol{R}} : \nabla \mathbf{u} \tag{3.23}$$

Recommended values of the model constants according to Rodi (1980) are given in table 3.1.

Table 3.1 – Standard k-$\epsilon$ model constants values for (Rodi (1980)) and Openfoam-code (2023a).

| $C_\mu$ | $\sigma_k$ | $\sigma_\epsilon$ | $C_{1\epsilon}$ | $C_{2\epsilon}$ |
|---|---|---|---|---|
| 0.09 | 1.0 | 1.3 | 1.44 | 1.92 |

In the derivation of the standard k-$\epsilon$ model, the flow is assumed to be fully turbulent and the effects of molecular viscosity to be negligible. Therefore the standard k-$\epsilon$ model is considered as a high Reynolds number turbulence model valid only for fully turbulent free shear flows and therefore cannot be integrated all the way to the wall (Moukalled et al., 2016).

#### 3.1.2.3 RNG k-$\epsilon$ model

The renormalized group (RNG) k-$\epsilon$ model was developed in order to improve the behavior of the standard k-$\epsilon$ model in the case of high streamline curvature flows such as, for instance, flows over a backward-facing step. It consists basically on a modification of a coefficient in the $\epsilon$ equation, to account for the interaction between the turbulent dissipation and the mean shear (Yakhot et al., 1992). In the (RNG) k-$\epsilon$ model, the k and $\epsilon$ equations are similar to equations 3.21 and 3.22. The only change is on the coefficient $C^*_{1\epsilon}$. In standard k-$\epsilon$ model, it is equal to $C_{1\epsilon}$, while in the RNG model, it is computed as:

$$C^*_{1\epsilon} = C_{1\epsilon} - \frac{\eta\,(1-\eta/\eta_0)}{1+\beta\eta^3}, \tag{3.24}$$

In (3.24), $\eta$ is the additional expansion parameter used in the derivation by Yakhot et al. (1992), defined as the time scale ratio of the turbulent to the mean strain rate, ($\eta = \dot{\gamma}\,k/\epsilon$). The eddy viscosity is still computed by equation (3.20).
All the model coefficients, except $\beta$ which is measured experimentally, are obtained through the derivation of the RNG k-$\epsilon$ model (see Table 3.2.).

Table 3.2 – Default values for RNG k-$\epsilon$ model.

| Reference | $C_\mu$ | $\sigma_k$ | $\sigma_\epsilon$ | $C_{\epsilon 1}$ | $C_{\epsilon 2}$ | $\eta_0$ | $\beta$ |
|---|---|---|---|---|---|---|---|
| Brown et al. (2016) | 0.0845 | 1.39 | 1.39 | 1.42 | 1.68 | 4.38 | 0.012 |
| Openfoam-code (2023b) | 0.0845 | 0.71942 | 0.71942 | 1.42 | 1.68 | 4.38 | 0.012 |

#### 3.1.2.4 Nonlinear k-$\epsilon$ model

The non linear k-$\epsilon$ model (NL) is a wall-bounded model proposed by Shih (1993) and Shih et al. (1996). Unlike to the standard k–$\epsilon$ model, this model does not produce negative normal stresses in particular situations of complex turbulent flows. The non linear k-$\epsilon$ model connects the mean strain rate of the flow to the Reynolds stress tensor using the quadratic algebraic nonlinear Reynolds stress model. The Reynolds stress tensor ($\boldsymbol{\tau^R}$) adjusts by adding a nonlinear stress term $\boldsymbol{\tau_{nl}}$, defined as:

$$\boldsymbol{\tau^R_{nl}} = \frac{2}{3}\,\rho\,k\,\mathbf{I} - \mu_t\,2\,\mathbf{D} + \boldsymbol{\tau_{nl}}. \tag{3.25}$$

where $\boldsymbol{\tau_{nl}}$ is:

$$\boldsymbol{\tau_{nl}} = \frac{1}{2}\,(\boldsymbol{\chi} + \boldsymbol{\chi}^T), \tag{3.26}$$

and:

$$\boldsymbol{\chi} = \frac{k^3}{\left(A_2+\eta^3\right)\epsilon^2}\left(C_{\tau 1}\left[\nabla\mathbf{u}\cdot\nabla\mathbf{u} + (\nabla\mathbf{u}\cdot\nabla\mathbf{u})^T\right] + C_{\tau 2}\left[\nabla\mathbf{u}\cdot(\nabla\mathbf{u})^T\right] + C_{\tau 3}\left[(\nabla\mathbf{u})^T\cdot\nabla\mathbf{u}\right]\right), \tag{3.27}$$

$C_{\tau 1}$, $C_{\tau 2}$, $C_{\tau 3}$ and $A_2$ are constants given in table 3.4. The definition of parameter $\eta$ is the same as in the RNG k-$\epsilon$ model. k and $\epsilon$ values are calculated using similar to RNG k-$\epsilon$ equations with coefficients of Table 3.3.

Table 3.3 – Coefficient values for nonlinear k-$\epsilon$ model.

| Reference | $C^*_{\epsilon 1}$ | $C^*_{\epsilon 2}$ | $\sigma_\epsilon$ | $\sigma_k$ |
|---|---|---|---|---|
| Shih (1993) | 1.44 | 1.99 | 0.77 | 1 |
| Brown et al. (2016) | 1.44 | 1.92 | 0.77 | 1 |
| Openfoam-code (2023c) | 1.44 | 1.92 | 1 | 1.3 |

Table 3.4 – Additional coefficient values for nonlinear k-$\epsilon$ model.

| Reference | $C_{\tau 1}$ | $C_{\tau 2}$ | $C_{\tau 3}$ | $A_1$ | $\alpha_\xi$ | $A_2$ |
|---|---|---|---|---|---|---|
| Shih (1993) | -4 | 13 | -2 | 1.25 | 0.9 | 1000 |
| Openfoam-code (2023c) | 3 | 15 | -19 | 1.25 | 0.9 | 1000 |

The eddy viscosity is obtained through the general relationship of the standard k-$\epsilon$ model (3.20). Except that the value of $C_\mu$ (equation (3.20)) depends upon the values of $\xi$ and $\eta$ by:

$$C_\mu = \frac{2}{3\left(A_1+\eta+\alpha_\xi\,\xi\right)}, \tag{3.28}$$

Where $\alpha_\xi$ and $A_1$ are constants (Table 3.4) and $\xi = \Omega\frac{k}{\epsilon}$ is an additional scalar parameter defined in terms of the mean rate of rotation, $\Omega = \sqrt{2\,\boldsymbol{\Omega} : \boldsymbol{\Omega}}$, with:

$$\boldsymbol{\Omega} = \frac{1}{2}\left(\nabla\mathbf{u} - (\nabla\mathbf{u})^T\right). \tag{3.29}$$

#### 3.1.2.5 k-$\omega$ and k-$\omega$ SST models

The k-$\omega$ turbulence model was originally developed by Wilcox (1988) to address the limitations of k-$\epsilon$ family models in resolving the complex flows, flows with adverse pressure gradients and near-wall flows. A new variable is introduced, $\omega$, which is the specific rate of turbulent dissipation, namely the rate at which turbulent kinetic energy is dissipated. This type of model also solves two transport equations to predict the turbulent flow properties.

The k-$\omega$ Shear-Stress Transport (SST) model introduced first by Menter (1994) is a variant of the k-$\omega$ model. While they share some similarities, they also have significant differences in terms of their capabilities and the types of flows they are best suited for. In terms of the model approach, the k-$\omega$ model is primarily designed for simulating wall-bounded flows, and it provides good predictions in the near-wall region. The k-$\omega$ SST is an extension of the standard k-$\omega$ model which combines elements of both k-$\omega$ and $k-\epsilon$ models. By using blending factors, the k-$\omega$ SST model tends to the k-$\omega$ model in the near-wall region and to the $k-\epsilon$ model away from the wall. This makes it versatile and suitable for a wider range of flows, including both wall-bounded and free-stream flows. The current build-in k-$\omega$ SST models of OpenFoam use the formulation of the Menter et al. (2003) governing equations as the following:

$$\frac{\partial \rho\, k}{\partial t} + \nabla \cdot (\rho\, k\, \mathbf{u}) = \nabla \cdot ((\mu + \sigma_k\, \mu_t)\ \nabla k) + P_k - \rho\, \beta^* \omega k, \tag{3.30}$$

$$\frac{\partial \rho\, \omega}{\partial t} + \nabla \cdot (\rho\, \omega\, \mathbf{u}) = \nabla \cdot ((\mu + \sigma_\omega\, \mu_t)\ \nabla \omega) + \frac{\gamma}{\nu_t} \cdot G - \rho\beta\omega^2 + 2\rho(1-F_1) \cdot \frac{\sigma_{\omega 2}}{\omega} \cdot \nabla k \cdot \nabla \omega. \tag{3.31}$$

where:

$$G = \rho\nu_t |\dot{\gamma}|^2, \qquad P_k = min(G, 10\rho\beta^*\, k\omega), \qquad \nu_t = \frac{a_1 k}{max(a_1\, \omega, \sqrt{2}\, \dot{\gamma}\, F_2)}\,. \tag{3.32}$$

With $\beta^* = 0.09$ and $a_1 = 0.31$. $F_1$ and $F_2$ are blending functions. $F_1$ is designed to be one in the near wall region (activating k-$\omega$ ) and zero away from the distance from the nearest wall (activating k-$\epsilon$). The coefficients $\sigma_k$, $\sigma_\omega$, $\beta$ and $\gamma$ are a blend of an inner constant (subscript 1) and an outer constant (subscript 2), blended according to the equation below:

$$\phi = F_1 \phi_1 + (1 - F_1)\phi_2. \tag{3.33}$$

in which $\phi_1$ and $\phi_2$ are given in Table 3.5 for each variable.

Table 3.5 – Default values for $\phi_1$ and $\phi_2$ used in equation (3.33) to calculate attributed parameters in equations (3.30) and (3.31).

| $\phi$ | $\sigma_k$ | $\sigma_\omega$ | $\beta$ | $\gamma$ |
|---|---|---|---|---|
| $\phi_1$ | 0.85034 | 0.5 | 0.075 | 0.5532 |
| $\phi_2$ | 1.0 | 0.85616 | 0.0828 | 0.4403 |

#### 3.1.2.6 Modified turbulent models for multi-phases simulations

So far all the turbulence models presented in the manuscript were developed primarily for a single flow. Therefore the turbulence models in their original form do not take into account the variability around the air-water interface (such as density or viscosity). For that reason, density should be implemented explicitly into the turbulence equations derivatives terms as spatially variable. In the used OpenFoam version (v2212), this modification has been made by default (except in the nonlinear k-$\epsilon$ mode). Thanks to the sharp interface-traking VOF method in OpenFoam (Eq. 3.9), the local density field is almost discontinuous. This discontinuity leads to a velocity gradient around the interface between water and air to the TKE transport equation, which, in turn, prompts an excessive production of TKE ($P_k$). Higher $k$ values produce higher eddy viscosity around the interface which finally introduces extra artificial dissipation and wave damping in propagating waves area. A few authors (Devolder et al.

(2017) and Larsen and Fuhrman (2018)) tackled this issue by adding a buoyancy term $G_b$ in the TKE equation (Eq. 3.30), as:

$$G_b = -\frac{\nu_t}{\sigma_t} \cdot \nabla \cdot \rho \mathbf{g} \tag{3.34}$$

Where $\mathbf{g}$ is the gravity acceleration vector.
The constant scalar $\sigma_t$ determines how much buoyancy is introduced. In our study, it is kept constant scalar during all the simulations presented and equals 0.85 (similar to Devolder et al. (2017)). The buoyancy term suppresses the artificial turbulence level at the free water surface, i.e. in the zone where a vertical density gradient exists, by driving the turbulent viscosity $\nu_t$ to zero. As a result, in the case of propagating waves, the model switches to the laminar regime near the free water surface, preventing excessive wave damping. Conversely in zones with a rather horizontal density gradient, e.g. surfing zone, the original turbulence model is recovered, as $G_b = 0$.
The performance of this enhanced method has been studied for propagating wave and breaking wave conditions in Devolder et al. (2017), Devolder et al. (2018), and Larsen and Fuhrman (2018) in comparison with the original turbulence models formulation given in Brown et al. (2016).
In addition to the buoyancy term, Larsen and Fuhrman (2018) also implemented a limiter factor in order to decay the unphysical TKE dissipation rate that occurs in the simulation due to the presence of numerical errors or instabilities in the turbulence model.
Owing to stability considerations (Larsen and Fuhrman (2018) model instabilities in our case), in this study, we used the Devolder et al. (2017) turbulent model closure only available for the k-$\omega$ and k-$\omega$ SST turbulence models in OpenFoam.

# 3.2 Post-processing Methods

## 3.2.1 Energy components

For each phase, mechanical energy ($E_m$) is composed of two elements: kinetic energy ($E_k$) and potential energy ($E_p$). The sum of the mechanical energy components of each phase makes up the total mechanical energy of the system ($E_T$ in equation (3.35)). Theoretically, unless energy is lost by any kind of dissipation, $E_T$ remains constant. Note that $E_T(t = 0)$ is equal to the sum of the initial potential and kinetic energies of the slide (Equation (3.36)).

Here the indexes of $s$, $w$, and $a$ denote the corresponding energy values for slide, wave, and air phases, respectively. Only internal energy dissipation in the slide ($\phi_s$) reduces the initial energy content $E_0$ before impacting water, with a negligible energy exchange with the ambient environment.

$$E_T = \sum_{m}^{water,slide,air} (E_{k,m} + E_{p,m}) \tag{3.35}$$

$$E_{T(t=0)} = E_{s(t=0)} = E_{k,s(t=0)} + E_{p,s(t=0)} \tag{3.36}$$

After impacting water, a portion of the mechanical energy of the slide transfers into the mechanical energy of water. This energy transformation continues until the slide motion stops.

At that time, the only remaining energy term in the slide is a constant potential fraction. Equation (3.37) summarizes the energetic exchanges between slide and water accounting for dissipation in each phase.

$$\left[\frac{d}{dt}(E_{ks} + E_{ps}) + \phi_s\right]_{slide} = -\left[\frac{d}{dt}(E_{k,water} + E_{p,water}) + \phi_{water}\right]_{wave} \tag{3.37}$$

The mechanical energy terms in each phase can be obtained from Equations (3.38) and (3.39). Here, the kinetic energy includes the turbulent kinetic energy component (TKE). We assume that the entire kinetic energy content in water is associated with the formed wave-train. To isolate the wave potential energy, it needs to be distinguished from the potential energy content of water at rest. Equation (3.40) theoretically explains the calculation of the potential energy of the wave $E_{p,wave}$. This formulation is applicable to the wave zone where the water column does not interfere with the slide phase ($x > X_p$), where $X_p$ is the x-position of the slide moving front (Figure 3.2). The potential wave energy is now independent of the coordinate reference by reducing the water potential energy of water content by the initial potential energy of water. For the sake of simplicity and to avoid confusion, henceforth, $E_{pw}$ represents only the wave-train gravitational potential content.

The wave potential energy can be additionally estimated using free surface integration in equation (2.9).

The energy dissipation term includes physical and numerical dissipation terms. There is no reliable way to estimate the numerical dissipation in the model and it originates from several inevitable inaccuracy sources such as numerical diffusion and dispersion errors, truncation errors, balance errors, and rounding errors.

On the other hand, the physical dissipation term can be calculated directly. It can be divided into two separate terms. The first one is the viscous dissipation that occurs in any flow around the walls and in zones with high internal vorticity. The viscous dissipation rate depends on the mean velocity gradient (strain rate) and the apparent fluid viscosity.

The second physical dissipation term is the turbulent dissipation which takes place in high-turbulence areas (specifically associated to wave breaking). The turbulence dissipation rate can be extracted from the turbulence parameters.

As already introduced, $\phi$ represents the rate of the physical energy dissipation in a specific fluid environment (slide, water, etc.). By integrating $\phi$ within times 0 and t, the dissipation energy can be expressed as equation (3.41).

An overall schematic view of the energetic processes which occur in the numerical domains is illustrated in Figure 3.2. We can rewrite the theoretical equations set (3.38 to 3.41) in a discretized form (3.42 to 3.45) for the calculation of energy components in phase $m$ by integrating cell(i,j) values in a two-dimensional -x and y- computational domain. These are also extendable for 3D domain results.

**In integral form:**
The kinetic energy term of the phase $m$ is:

$$E_{k,m} = \iint_A \alpha_m \ (\frac{1}{2}\ |\mathbf{u}|^2 \ + k \ ) \ \rho \ \ dx\, dy \tag{3.38}$$

Also the potential energy term of the phase $m$ reads as:

$$E_{p,m} = \iint_A \alpha_m \ g \ y \ \rho \ \ dx\, dy \tag{3.39}$$

$A$: area of the 2D computation domain.
The potential energy of the wave is given by:

$$E_{p,wave} = \iint_{X_p}^{\infty} \alpha_w \ \rho \ g \ y \ \ dx\, dy - \int_0^{h_0} \int_{X_p}^{\infty} \ \rho \ g \ y \ \ dx\, dy \tag{3.40}$$

Where $X_p$ is the x-position of the slide moving front.
The energy dissipation term is expressed as:

$$E_{diss,m} = \int_{t=t_0}^{t=t_1} \underbrace{(\iint_A \alpha_m \ \mu_m \ \dot{\gamma}\dot{\gamma}\, dx\, dy + \iint_A \alpha_m \ \epsilon \ \rho\, dx\, dy)}_{\text{physical energy dissipation rate } (\phi)} \ dt \tag{3.41}$$

**In discretized form:**

$$E_{k,m} = \sum_{i=1}^{N_x} \sum_{j=1}^{N_y} \alpha_m(i,j) \ ( \underbrace{\frac{1}{2}\ |u^2(i,j)|}_{\text{mean flow kinetic energy term}} + \underbrace{k(i,j)}_{\text{TKE term}} \ ) \ \rho_m \ \Delta A(i,j) \tag{3.42}$$

$$E_{p,m} = \sum_{i=1}^{N_x} \sum_{j=1}^{N_y} \alpha_m(i,j) \ \rho_m \ g \ y(i,j) \ \Delta A(i,j) \tag{3.43}$$

$$E_{p,wave} = \sum_{i=X_p}^{N_x} \sum_{j=1}^{N_y} \alpha_w(i,j) \ \rho_w \ g \ y(i,j) \ \Delta A(i,j) - \sum_{i=X_p}^{N_x} \sum_{j=1}^{h_0} \ \rho_w \ g \ y(i,j) \ \Delta A(i,j) \tag{3.44}$$

$$\phi_m = \underbrace{\sum_{i=1}^{N_x} \sum_{j=1}^{N_y} \alpha_m(i,j) \ \mu_m \ \dot{\gamma}(i,j)\dot{\gamma}(i,j) \ \Delta A(i,j)}_{\text{mean flow dissipation term}} + \underbrace{\sum_{i=1}^{N_x} \sum_{j=1}^{N_y} \alpha_m(i,j) \ \epsilon(i,j) \ \rho_m \ \Delta A(i,j)}_{\text{turbulence dissipation term}} \tag{3.45}$$

Where $N_x$ and $N_y$ represent the node number in the x and y direction, respectively. $\alpha(i,j)$ is the corresponding phase indicator value (phase-fraction) of a cell for the phase $m$ (between 1 for totally occupied by the intended phase $m$ and vice versa). $\Delta A(i,j)$ represents the area of the cell. $y(i,j)$ is the cell center elevation from a Cartesian coordinates with origin on initial water surface level (Fig. 3.2).
$\dot{\gamma}(i,j)$ denotes the scalar shear rate value in the cell(i, j) (as already described in Eq. (3.7)).

$\mu_m$ is the apparent viscosity of phase $m$. For a Newtonian fluid, the apparent viscosity is constant and equals to the dynamic viscosity of the fluid. For a non-Newtonian fluid, the local computed values of viscosity should be applied in this relation (see section 2.8.2.2). $\epsilon$ is the turbulence kinetic energy dissipation rate in k-$\epsilon$ turbulence models family. For k-$\omega$ models, it is calculable by the following relation:

$$\epsilon = 0.09\ \omega\ k \tag{3.46}$$

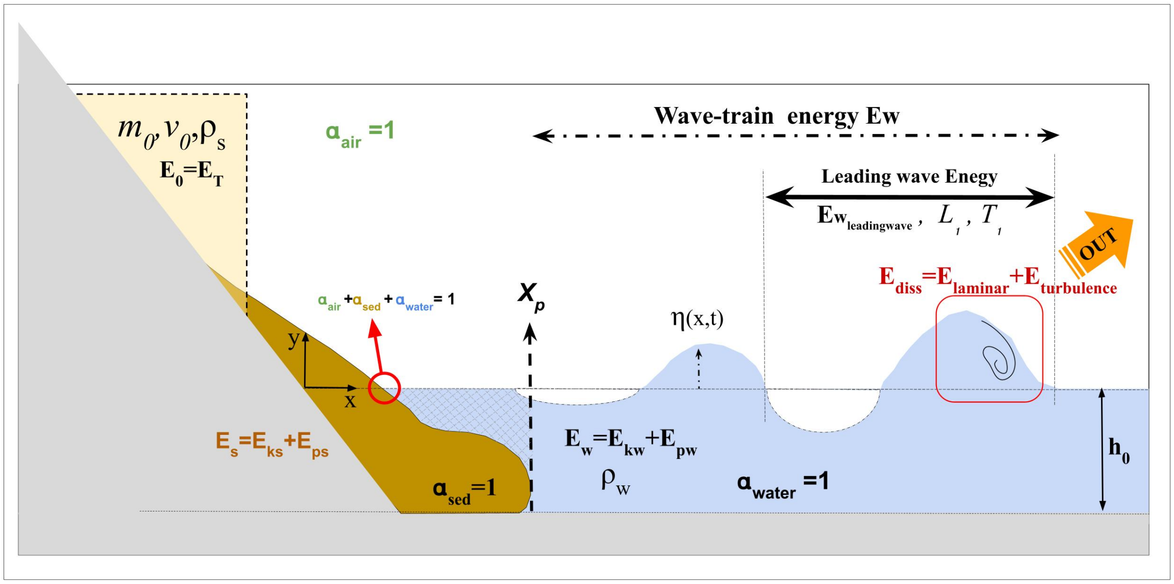

Figure 3.2 – Schematic view of the physical problem with the indication of energy components and dimensional parameters.

## 3.2.2 Wavelet analysis

### 3.2.2.1 Continuous Wavelet Transform (CWT)

The continuous wavelet transform (CWT) of a continuous-time signal $s(t)$ is defined as:

$$s(a, b) = \frac{1}{\sqrt{a}} \int_{-\infty}^{\infty} s(t)\Psi\left(\frac{t-b}{a}\right) dt, \tag{3.47}$$

where $b$ is the translation (time shift) and $a$ the dilatation (scaling in frequency) of the mother wavelet $\Psi$. $a$ and $b$ may be varied continuously ( $-\infty < b < +\infty$ and $a > 0$). The CWT thus transforms the signal from the time to the time-scale domain. Contrary to Fourier transform that yields an average amplitude of over the entire dataset, CWT analysis expands a one-dimensional time series into the two-dimensional parameter space ($a$, $b$), and provides a local measure of the relative amplitude of activity at scale $a$ at time $b$. Here $\Psi$ is a windowing function that with a convolution examines the characteristics of a data signal both in the time and in the frequency domain. This function can be replaced with a motherwavelet function. A motherwavelet function must verify two admissibility conditions:

$$\begin{cases} \int_{-\infty}^{\infty} \Psi(t)\, dt = 0, & \text{the zero mean condition} \\ \int_{-\infty}^{\infty} |\Psi(t)|^2\, dt < \infty. & \text{the finite energy condition} \end{cases} \tag{3.48}$$

In this study as in many studies, wavelet analysis has been performed using Morlet motherwavelet (Figure 3.3). The Morlet wavelet (Morlet (1983) and Grossmann and Morlet (1984)) is a plane wave modulated by a Gaussian. It is described by the following equation (Liu (2000) and Fritz and Liu (2001)):

$$\Psi_0(t) = \pi^{-1/4}(e^{-imt} - e^{-m^2/2})\, e^{-t^2/2}, \tag{3.49}$$

The wavelet transform of this wave-mother is defined by:

$$\hat{\Psi}_0(\omega) = \pi^{-1/4}(e^{-(\omega-m)^2} - e^{-(-m^2+\omega^2)}), \tag{3.50}$$

where $m = \pi\sqrt{2/ln2}$ is the basic frequency ($\omega_0$). If $m > 5$ then the second term in Eq. (3.50) becomes negligible. So in fact, some authors present the Morlet wavelet as :

$$\Psi_0(t) = \pi^{-1/4}(e^{-imt})\, e^{-t^2/2}, \tag{3.51}$$

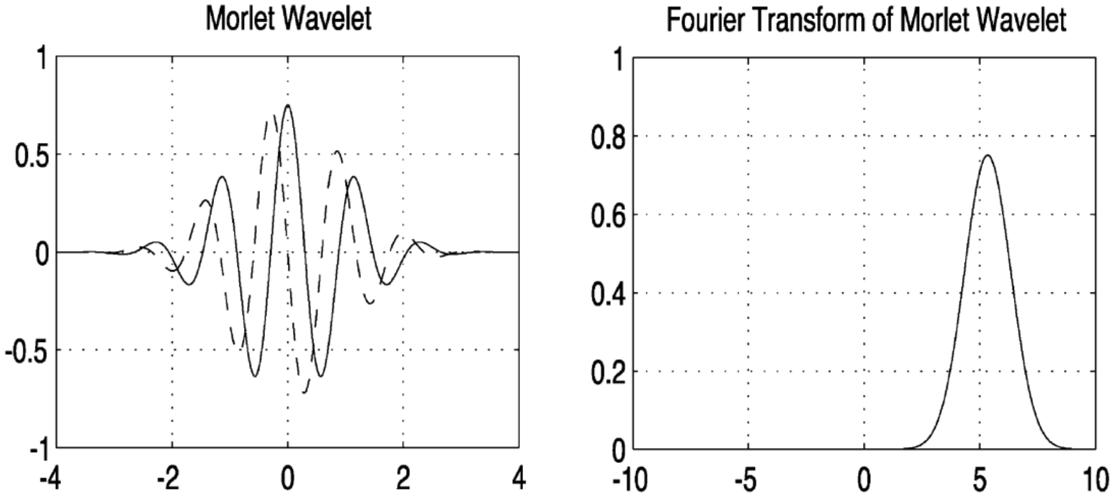

Figure 3.3 – Morlet wavelet and its wavelet transform, left panel: real and imaginary component plot in the time domain and right panel: frequency domain (Panizzo et al., 2002).

## 3.3 Validation of the model - introduction

The validation of a model for the study of wave generated by landslide is a complex task due to two main reasons. First, because the slide, in itself, is a challenge to simulate due to the complex interplay of various physical phenomena involved between two separate phases. Second, because after generation, waves experience dramatic changes such as dispersion, breaking at different time scale, which also represent highly difficult problems for the computation, even individually taken.

In the context of this study, we decided to simplify the first problem by considering a continuous liquid phase for the slide (i.e., either Newtonian or Non Newtonian). This allows to model the generation with a reliable VOF approach. Nevertheless, as the considered problem is somehow slightly disconnected from the real applications, to the best of the author knowledge, reference experimental studies are not available.

For this reason, and also due to the second difficulty previously pointed out in the first paragraph (i.e., several complex wave processes to investigate), we decided to cut the problem in peaces and consider each processes separately. The latter include, landslide propagation over a slope, liquid slide wave generation and breaking, then pure wave processes with non linearity, dispersion and energy dissipation by breaking. One of the most important aspect of this validation stage is the conservation of energy which is usually rarely addressed. Indeed, in order to provide accurate interpretations, it is here crucial to ensure that numerical dissipation is controlled and that the dissipation is really due to physical processes.

It is important to note that OpenFoam has already been validated in several previous studies for the generation of waves by landslides. The purpose is generally to show that the generated waves can be properly simulated. Nevertheless, most of the time, as already pointed out, the slide model is not consistent with the reference experiment and the model has to be tuned. For instance, Paris et al. (2021) used a viscous slide with a calibrated viscosity to reproduce a granular experiment (Viroulet et al., 2013). Romano et al. (2023) implemented a Coulomb viscoplastic rheology model in OpenFoam to simulate granular experiments. While the rheology is closer, it does not take into account the penetration of the water flow within the slide grain and therefore the model has also to be calibrated. An exception is the numerical study of Rauter et al. (2021) which addressed waves generated by a water slide (Bullard et al., 2019). The results showed the difficulty to reproduce the slide shape at impact, nevertheless, the wave field appear correctly reproduced. We did not try to reproduce this simulations, but we took into account the conclusions of the authors regarding the resolution requirements and the CFL constraints.

In the following, we propose a complete validation of the model with respect to individual processes acting in the global problem studied. Table 3.6 gives an overall view of the work performed and present the different model setup to allow easy comparison for the reader.

Finally, for all following cases, the kinematic viscosity and density of water and air are $10^{-6}$ $(m^2.s^{-1})$, 1000 $(kg.m^{-3})$, $1.48 \times 10^{-5}$ $(m^2.s^{-1})$ and 1 $(kg.m^{-3})$, respectively.

Table 3.6 – Setup properties of validation cases considered in this study.

| General purpose | (#) Case | Cell dimension (mm) | # cells in incident[†] | Bottom BC | Solver | Turbulence | CFL | Conv. scheme |
|---|---|---|---|---|---|---|---|---|
| slide propagation | (1)Rheology | 0.625*0.625<br>0.83*0.83<br>1.25*1.25<br>2.5*2.5 | 4-12 | no-slip | interFoam | laminar | 0.5 | linearUpwind |
| wave generation and breaking | (2)Janosi moving gate | 5*5 | 12 | No BC | overInterDyMFoam | $k-\omega$ SST (Devolder et al. (2017)) | 1 | linearUpwind |
| | (2)Janosi 2-3phases | 5*5 | 12 | no-slip | interFoam<br>multiphaseInterfoam | $k-\omega$ SST (Devolder et al. (2017)) | 0.1 | linearUpwind |
| wave dispersion | (3)Undular bore | 20*2 | 7-15 | no-slip | interFoam | $k-\omega$ SST (Devolder et al. (2017)) | 0.1 | linearUpwind |
| energetic processes | (4)Couette shear flow | 0.2*0.1 | 100 | no-slip | interFoam | laminar | 0.5 | linearUpwind |
| | (5)Propagating solitary | 68.8*68.8<br>34.4*34.4<br>17.2*17.2 | 4-15 | free-slip | interFoam | laminar | 0.2 | linearUpwind |
| | (6)Breaking solitary | 2.5 * varies<br>5*varies | 40-80 | no-slip | interFoam | varies (table 3.10) | 0.5 | linearUpwind |
| | (7)Turbulent bore | 10*10<br>5*5<br>2*2 | 10-40 | free-slip | interFoam | $k-\omega$ SST (Devolder et al. (2017)) | 0.1 | linearUpwind |

[†] The term "incident" here refers to the intended phenomenon zone under study. The rheological case, involves the slide thickness, wave height for the propagating wave, and the breaking wave at the moment of breaking (for Janosi and solitary breaking, and turbulent bore case). Additionally, it encompasses the entire domain under shear stress in the Couette case.

### 3.3.1 CASE 1: Slide propagation - validation of the Non Newtonian rheological model

This section presents a validation of the Herschel-Bulkley rheology model implemented in OpenFoam based on the experimental and analytical results of Huang and García (1998). In this study, the setup consists of an adjustable tilted Plexiglas tank 100 cm length and 30 cm width. In the upstream section, a constant 10 cm long reservoir (with an area of A) released a kaolin-water mixture with varying volumetric concentrations ($C_v = V_{solid}/(V_{solid} + V_{water})$) over the slope (angle $\theta$) through a sliding gate. Table 3.7 provides the parameters of the three experiments conducted. Figure 3.4 shows an example of a mesh used for case (a). In the computational domain, the gravity vector is tilted to reproduce the effect of the slope angle. The domain is split in different zones, each featuring an adapted resolution. In particular, in the zone in which the fluid moves, the cell size is the finest. Indeed, the shear rate generated in the boundary layer adjacent to the bottom plays a key role in determining the fluid viscosity and should be properly resolved. Moreover, the experimental results show that the slide thickness drops very quickly to very small values (<1 cm), therefore, the mesh had to adapt to this feature. In the present study we tested different mesh sizes, namely : 0.625mm, 0.833mm, 1.25 mm, and 2.5mm, to allow conducting a sensitivity study. Figures 3.5 and 3.6 shows the experimental data and the corresponding simulation results. Snapshots of slide interfaces are shown in figure 3.5. This figure shows that if the slide front position is well predicted by the model, the profile shows some discrepancies with the measured reference. In particular, a few oscillations are visible in the slide shape simulated in a zone where a strong shear flow is expected. This may be due to slight inaccuracy of the numerical approximation in this area, which may lead to artificial Kelvin-Helmoltz type instabilities. Figure 3.6 shows the slide front displacement and the hydrograph for the less dense and viscous case (i.e., case (c)). Physically, in the initial stages of motion, the slide encounters resistance to movement. Once the its motion initiated, the slide accelerates until, again due to resistance forces, it decelerates and eventually comes to a stop. This figure shows that there is a time lag in the initial motion of the slide between the simulation and the experiment. If we omit this lag, and compare only the slope of the curves, then the prediction of the front displacement is approximately equivalent to the data. The

Table 3.7 – Rheological parameters (Equation (2.13)) measured for different kaoline-water suspensions (Huang and García, 1998).

| Cases | $C_v$ | Bulk density, $\rho$ | $\tau_0$ | $k$ | $n$ | A | $\theta$ |
|---|---|---|---|---|---|---|---|
| - | % | $(gr.cm^{-3})$ | $(Nm^{-2})$ | $(Nm^{-2}s^n)$ | - | $(cm^2)$ | degree |
| a | 21.07 | 1.348 | 14.10 | 10.20 | 0.34 | 29.2 | 18.5 |
| b | 19.59 | 1.323 | 9.96 | 7.10 | 0.38 | 32.4 | 24.5 |
| c | 13.05 | 1.215 | 2.21 | 0.22 | 0.75 | 24.7 | 11 |

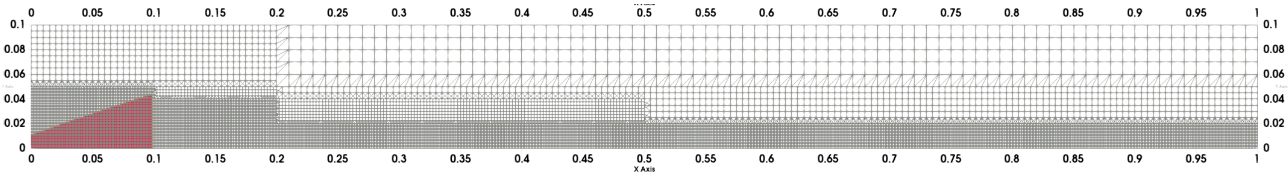

Figure 3.4 – Example of mesh corresponding to the simulation of case (a) (Huang and García, 1998). In this example, the finest mesh cell is 1.25 mm. The initial slide phase is also provided in red (left part of the domain).

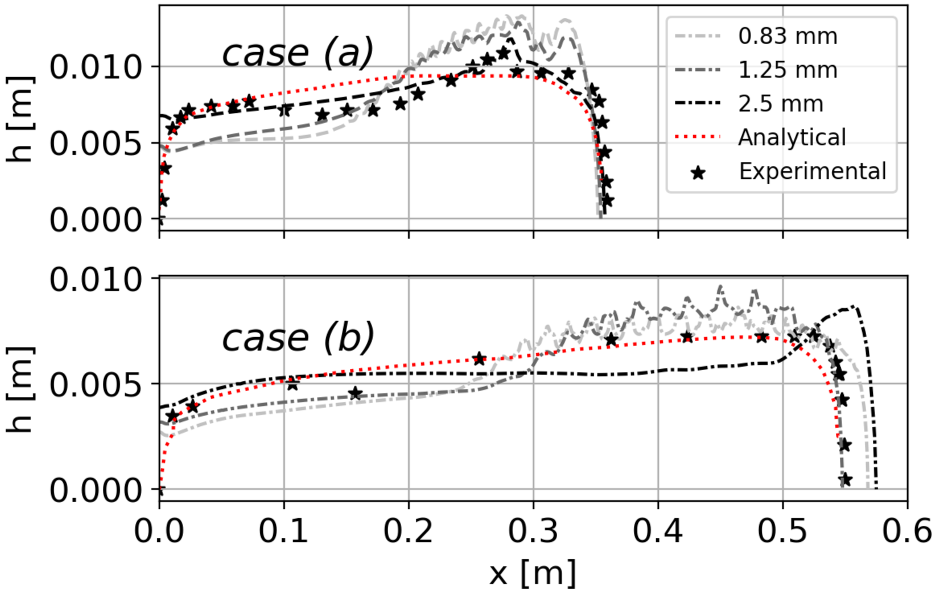

Figure 3.5 – Comparison of theoretical, experimental data in Huang and García (1998) and numerical OpenFoam rheological model results free-surface profile for different cell sizes for case (a) and (b), (refer to Table 3.7)

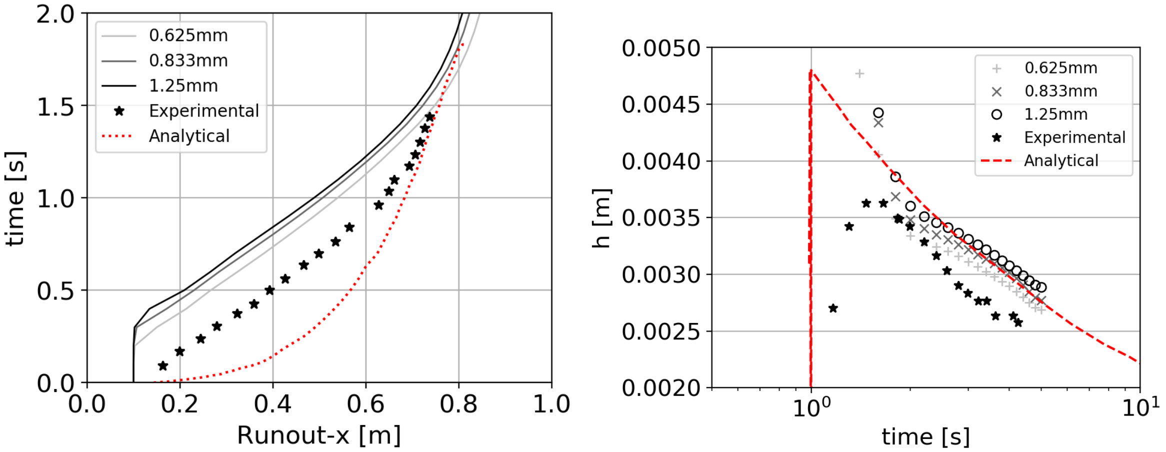

Figure 3.6 – Comparison of theoretical, experimental data in Huang and García (1998) and numerical OpenFoam rheological model results of front spreading rate (left) and hydrograph at x = 0.689 m (right) for the case (c) for different cell sizes (0.625 mm, 0.833 mm, and 1.25 mm).

right plot also shows differences with the measurements while corresponding better to the theoretical model. Regarding the sensitivity study, both figures show that the difference between the mesh results is not very significant. In summary, we conclude that the model accurately predicts the position of the slide but has some difficulty with the shape. Correct results can be obtained when, at least, 4 to 7 cells are used to discretize the running slide thickness.

### 3.3.2 CASE 2: Wave generation and breaking

To evaluate the capacity of the model to generate a violent impulse wave, we considered the Jánosi et al. (2004) experimental test case. This classical wet dam break results in a wave that breaks immediately as a plunging breaker (Figure 3.7). This case involves the interaction of two water masses with energetic transfers from one mass to the other, followed by a complex free surface evolution during the breaking. As such, it involves similar processes as the ones usually acting during the generation of a wave by a sliding mass except that, here, there is no slope.

The experiment was carried out with three different downstream water levels (with the upstream water height $d_0 = 150$ mm): a dry case ($d = 0$), a rather shallow water case ($d = 18$ mm), and a deeper case ($d = 38$ mm). For validation purposes, we focused only on the deeper case. In order to reproduce the observed interface evolution, the motion of the gate has to be simulated. Note that this gate motion has to be inferred as no law is given in the reference paper. In our study, the most precise results were obtained with a gate upward velocity set to 1 m/s. As a reference, Dumergue and Abadie (2022) imposed a gate upward constant velocity of 1.5 m/s with the model THETIS in order to best fit the observations. To simulate the gate motion, we implemented the "`overInterDyMFoam`" solver, a compatible version of "`InterFoam`" (used for two incompressible, isothermal immiscible fluids using VOF) with the over-set method. The mesh is uniform with a 5 mm square cell size for the fixed domain and 2 mm cells in the dynamic mesh zone. In our simulation, we presumed the gate thickness to be equal to 5mm. To ensure the gate is fully closed at the beginning, we defined a layer of impermeable porous medium at the bottom. This was necessary since usual wall boundary conditions cannot overlap with the gate contour at the beginning. Finally, a turbulence model has been utilized with the same setup as the next validation cases.

Figure 3.8 shows a comparison of the simulated and measured free surface location at different times. Globally, the correspondence between the two is very good. The model is able to reproduce the wave generation and breaking very accurately. Note that to obtain this result, we also had to use an additional 2 cm longitudinal offset (40 cm instead of the original 38 cm as mentioned in the original paper). This discrepancy could potentially be attributed to unknown factors such as the gate thickness for example or data digitization errors. We can infer from the preceding section that the breaking wave interface is accurately predicted by the two-phase model "`interFoam`". However, usually, to simulate wave generated by landslide, a three-phase model is required (slide, water and air) such as "`multiphaseInterfoam`". It is therefore important to also check the validity of the latter model. To do so, we repeated the Jánosi et al. (2004) case but without gate motion, as "`multiphaseInterfoam`" is not currently able to manage a dynamic mesh. The obtained results are compared to results obtained with the "`interFoam`" solver but without gate motion. Note that in the three phase simulation, two phases are water and the third phase is air. Figure 3.9 shows the comparison of the two model results. Obviously, they are very close to each other. Nevertheless, even though the problem solved is theoretically the same, a few slight discrepancies can be observed between the two model outputs, like the size of the air bubble entrapped for instance, or the rear part of the wave which is sharper in the three-phase case.

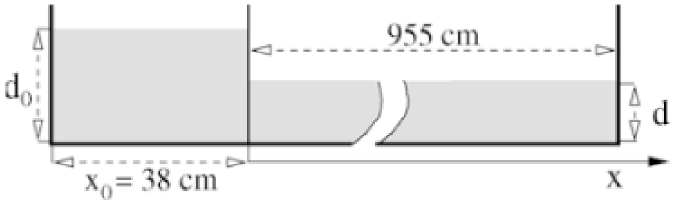

Figure 3.7 – Schematic of the wet dam break setup (Jánosi et al., 2004) used for the model validation with $d_0 = 15cm$ and $d = 38mm$.

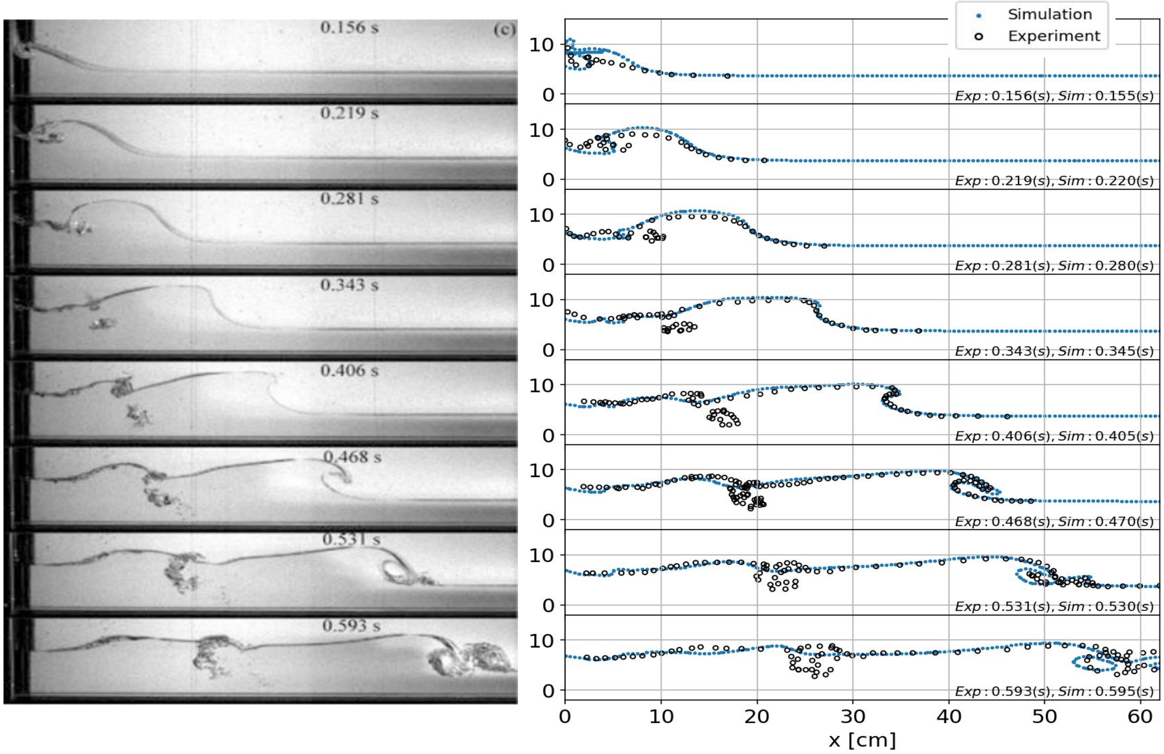

Figure 3.8 – Wave generated in a wet dam break. Left panel: sequences of experimental snapshots after releasing water from Jánosi et al. (2004), right panel: comparison between experimental and numerical results (this study).

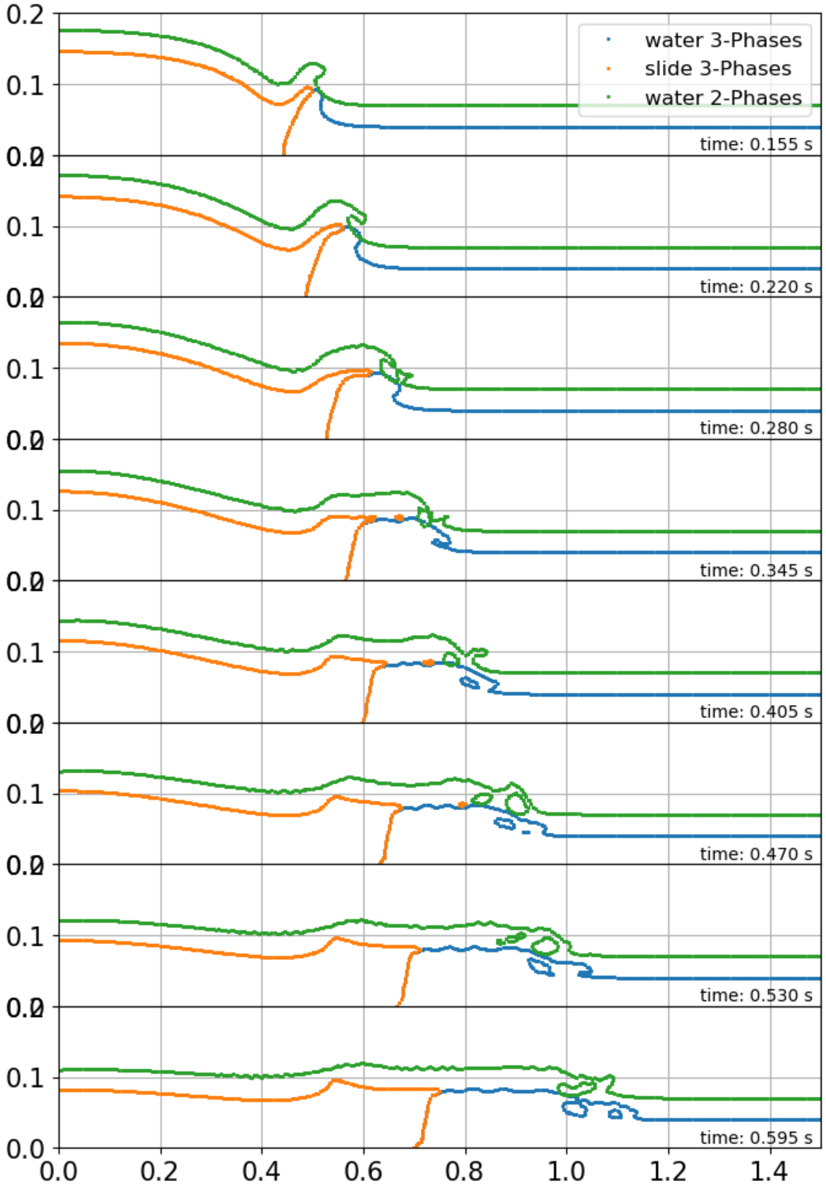

Figure 3.9 – Comparison between two-phase "`interFoam`" and three-phase simulations "`multiphaseInterfoam`" for the same case as Figure 3.8 but without gate motion simulation. Note that we applied a vertical offset of 5 cm to "`interFoam`" results in order to ease the comparison. Horizontal and vertical legend dimensions are in meters.

### 3.3.3 CASE 3: Wave dispersion - case of the undular bore

A wave generated by a subaerial landslide is generally non linear and dispersive. Moreover, in most of the cases, the leading wave exhibits diforsipation by breaking. The last point will be investigated in detail in the next section. Here, we focus on the ability of the model to reproduce a non linear dispersive wave train. For that purpose, we simulate the generation of an undular bore with a wet dam break similar to the experiment described in Soares Frazao and Zech (2002). In this work, undular bores with different Froude numbers are generated and measured. Note that an undular-bore waves form only if the change in surface elevation of the wave is less than 0.28 of the initial water depth (Peregrine (1966)). If it is more, the bore becomes turbulent. In this section, we considered two Froude numbers as indicated in Table 3.8 with also the upstream and downstream water levels.

We numerically re-constructed the two model setups and compared the water surface signals computed and measured at different gauges positions.

The model setup is a wet-dam break case. The computational domain is 53 meters long with an upstream reservoir of 26.91 m assumed to be equivalent to an infinite length. The gauges are located at x= 33.06 m, 40.06 m, and 42.56m, respectively, from the beginning of the domain.

Table 3.8 – Characteristics of the undular bores computed in this study.

| Froude number | upstream water level | downstream water level |
|---|---|---|
| 1.0104 | 0.323 m | 0.251 m |
| 1.1702 | 0.3685 m | 0.2477 m |

A mesh sensitivity study is presented in figure 3.10 for a particular Froude number. This study involves mesh cells stretched in the horizontal direction. As can be observed, the model seems to converge but not to the measured data.

The rest of the results are given for the finer mesh resolution. This mesh approximately covers the maximum wave height within ten cells and the horizontal cell dimension is stretched 10 times. Figure 3.11 shows the comparison of the numerical results with the measurements. The model predicts the development of undulations at frequencies consistent with the measurements. Nevertheless, it also tends to underestimate the amplitude of theses oscillations, especially for the larger Froude number. Hence, we can expect some inaccuracies in the future simulations of highly non linear dispersive waves. This is not a surprise as CFD models, such as OpenFoam, are known to suffer from numerical dissipation, which is not compatible with an accurate treatment of non linear waves (for more adapted method see for instance Raoult et al. (2016)).

Table 3.9 illustrates the relative errors of the simulated wave parameters. The comparison further highlights a higher margin of error in the modeled wave height compared to the wave period.

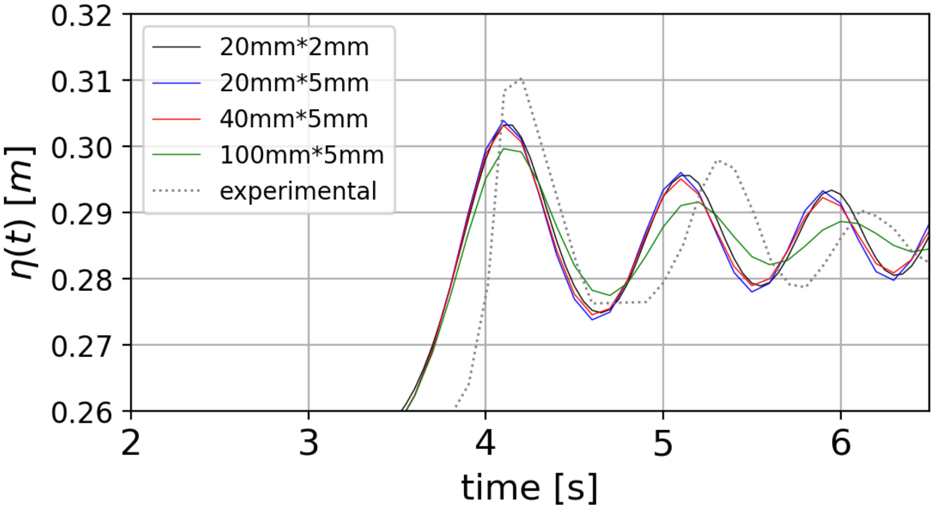

Figure 3.10 – Undular bore case (Fr = 1.0104). Comparison between the simulated free surface obtained with various mesh resolutions and the measurements of Soares Frazao and Zech (2002) (dotted line) at x= 33.06 m gauge position.

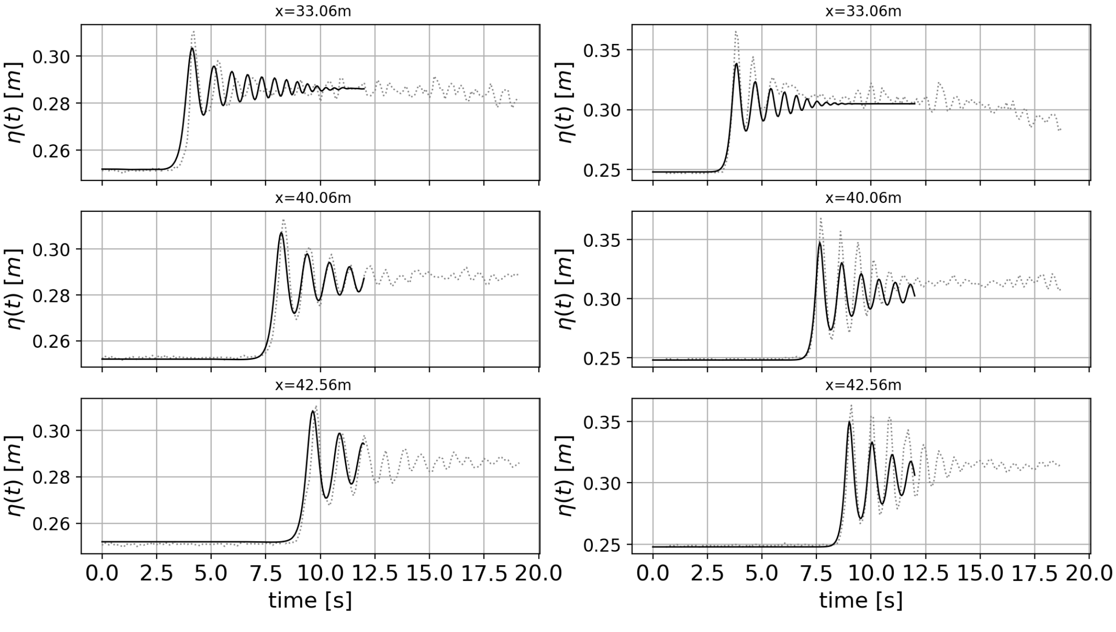

Figure 3.11 – Undular bore free surfaces for Fr = 1.104 (Left panel) and Fr = 1.1702 (Right panel) at different gauges positions. Navier-Stokes model (solid line) and measurements by Soares Frazao and Zech (2002) (dotted line).

Table 3.9 – Error assessment for the first three waves in the case ($H$, wave height and $T$, period): Fr=1.0104 at gauge x=33.06m.

| - | Experimental | Simulation | Difference |
|---|---|---|---|
| $H_1$ | 0.04 m | 0.0284 m | -29 % |
| $H_2$ | 0.019 m | 0.0179 m | -6.8 % |
| $H_3$ | 0.0077 m | 0.0127 m | +64.3 % |
| $T_1$ | 1.18 s | 1 s | -14.7 % |
| $T_2$ | 0.83 s | 0.82 s | -8.8 % |
| $T_3$ | 0.77 s | 0.72 s | -7 % |

### 3.3.4 CASES 4 to 7: Validation of the energetic processes

Accurately simulating energetic transfers in wave generated by subaerial landslide is a difficult matter requiring the consideration of several complex processes. Theoretically, the initial slide potential energy progressively transforms into kinetic energy and, after the impact, into wave kinetic and potential energy. During these processes, a fraction of this energy is dissipated, both from viscous (mainly associated with bottom friction and velocity gradients at the interfaces) and turbulent dissipation. The latter is mostly generated near the wave crest in wave breaking, either very violently (plunging breaking) or more gradually (in the turbulent bore case). During this process, some part of the mean flow kinetic energy is transferred to turbulent kinetic energy (TKE). This process is the most important contribution to the global dissipation (Equation (3.41)). In this respect, finding the best turbulence model and the most suitable model configurations is imperative. This is one of the objective of this section. Another objective is to quantify the numerical dissipation of the model. Indeed, when investigating the energetic processes, it is key to ensure that the energy dissipation is due to actual physical processes and not a numerical artefact. CFD models inherently suffer from numerical errors usually inducing significant diffusion. The objective of this part is at least to quantify and if possible minimize this diffusion. The following sections present several validation cases which address this general question of the dissipation computation.

#### 3.3.4.1 CASE 4: Validation of the strain rate computation in the two-phase Couette shear flow

The laminar part of the dissipation equation (3.41) involves the computation of the strain rate which, in this study, is carried out through a user-implemented function object[2]. The main purpose of this section is to validate this function. The case considered is a two-phase Couette flow in a 2 cm long, 1 cm high, 2D domain, involving two Newtonian fluids with different viscosities. The velocity field gradually evolves by shear stress through the domain under the action of a moving wall boundary condition imposed at the top of the domain (constant horizontal velocity ($U_x = V_2 = 0.000224$ (m/s)). The small Reynolds number ($R_e$=0.2) ensures the flow to be laminar. Cyclic boundaries are set at the left and right boundaries, and a no-slip condition is applied to the bottom. The simulated velocity profile is expected to converge to the analytical solution which features two specific constant velocity gradient values in each phase (Figure 3.12). Figure 3.13 shows the converged numerical solution and the comparison with the analytical solution. The correspondence with the analytical solutions is verified for the velocity field as well as the strain rate value.

---

[2] presented in appendix A

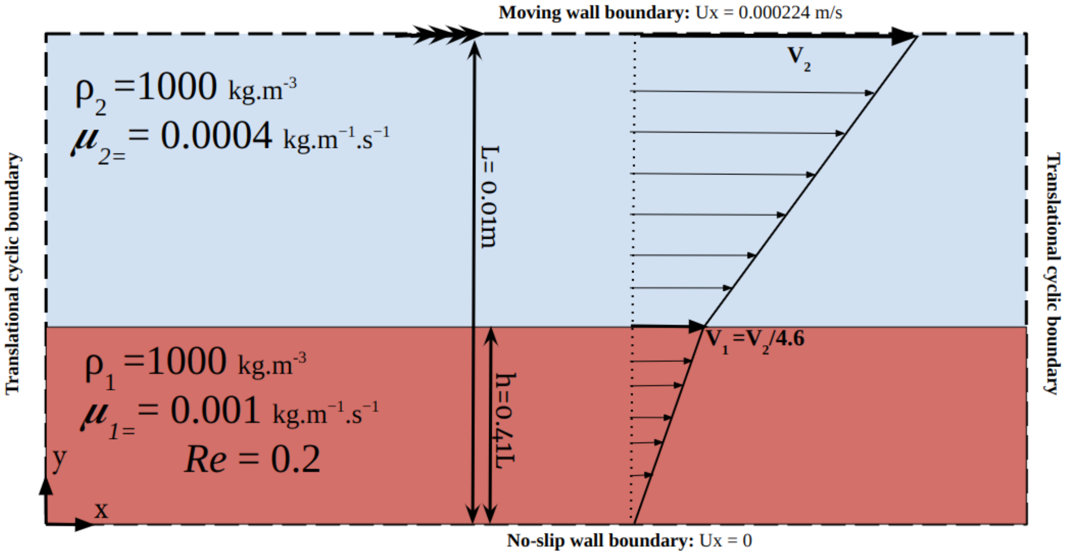

Figure 3.12 – Schematic view of the two-phase Couette flow test case.

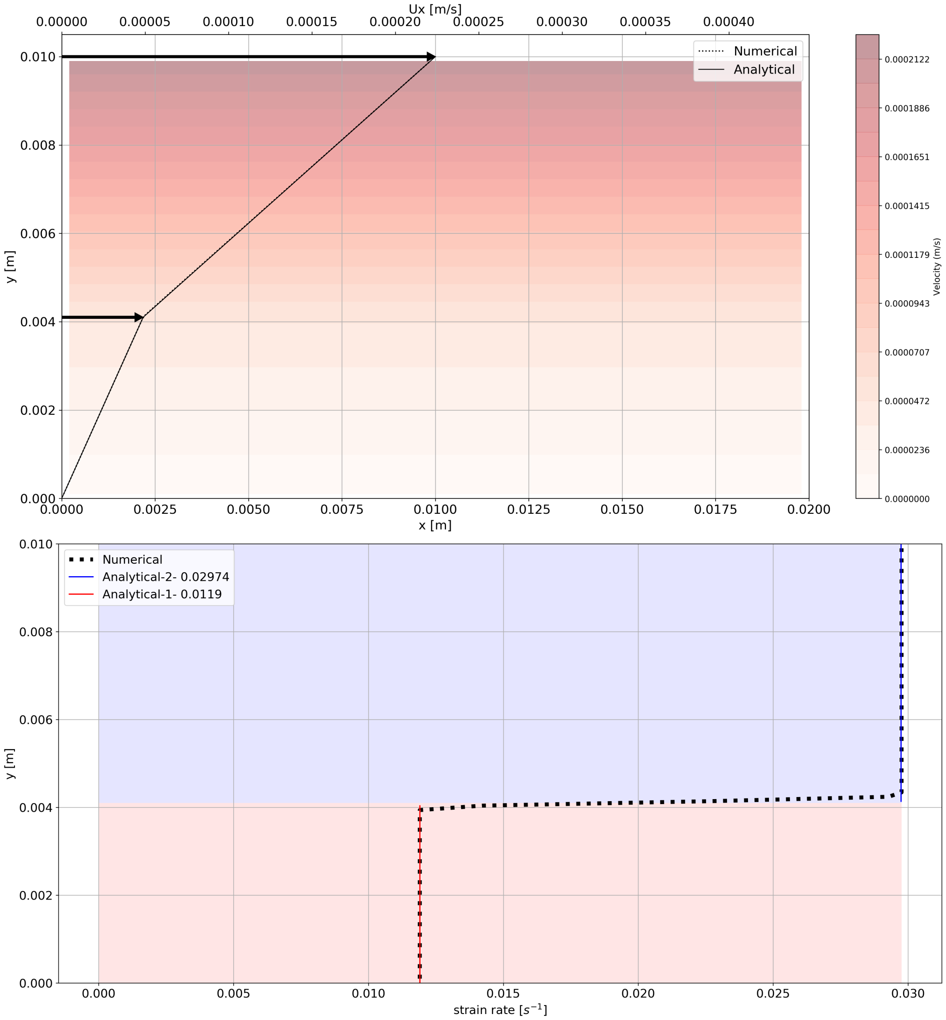

Figure 3.13 – Comparison of modeled and analytical velocity profile and strain rate value at t = 10000 (s).

### 3.3.4.2 CASE 5: Energy conservation in a propagating solitary wave

The solitary wave is a common wave type appearing in the process of wave generated by a subaerial landslide. It occurs generally after different wave transformation processes (dispersion and dissipation). In this case, the wave should be able to properly propagate without being artificially damped by numerical diffusion. The purpose of this section is therefore to control the conservation of energy for a propagating solitary wave over a flat bottom.

The computational domain, similar to the case studied in Wroniszewski et al. (2014) exhibits a length of 72.6 m, a height of 2.2 m and is discretized with square-shaped cells. The solitary wave is generated at the left boundary based on the formulation of Grimshaw (1970) (Figure 3.14). The ratio of wave height to water depth $H/h_0$ is equal to 0.3 and the water depth ($h_0$) is 1.0 ($m$). The bottom boundary condition is set to a "free-slip" condition to eliminate the viscous dissipation at the bottom.

The wave energy is the sum of the kinetic and potential components ($E_w = E_k + E_p$) :

$$E_k = \iint_A \alpha \, (\frac{1}{2} \, |\mathbf{u}|^2) \, \rho \, \, dx \, dy \tag{3.52}$$

$$E_p = \iint_A \alpha \, g \, y \, \rho \, \, dx \, dy \tag{3.53}$$

With the $y$ reference set at the initial water surface. Simulations were carried out for a duration of 20 seconds. There are several sources of errors in this problem. The first one is the initialisation of the water volume fraction. For instance , with three different resolutions ($1056 \times 32$, $2112 \times 64$ and $4224 \times 128$) the error compared to the theoretical value of the water mass at t=0 is 3.54, 0.31 and 0.30% respectively. The second error source comes from the progressive diffusion of the water volume fraction at the interface. Figure 3.15 illustrates the effect of this artificial diffusion on the potential energy variation over time considering only the interface zone cells ($0.05 < \alpha_w < 0.95$) for the three previous tested resolutions. The potential energy increases with an unacceptable rate in the case of the coarsest mesh resolution, while the finest resolution allows to keep a reasonable accuracy over time. Finally, the evolution of the wave energy components is presented on Figure 3.16 for the finer mesh. Kinetic and potential energies are obviously stable over the 20 s computation (difference about 1%), which approximately corresponds to a propagation over about 10 equivalent wave lengths (Figure 3.14). In brief, the results demonstrate that, for a propagating wave, energy conservation can be ensured providing that sufficiently fine cells are used. In the case of the solitary wave, it was necessary to discretize the wave height with almost 20 cells to reach a satisfactory accuracy.

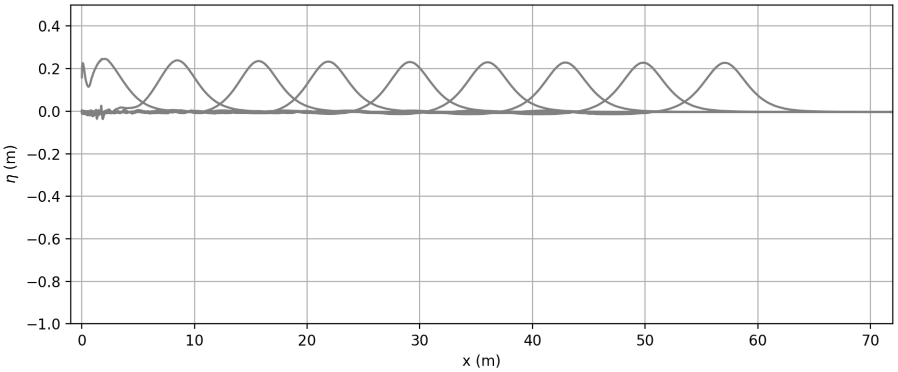

Figure 3.14 – Water surface profile ($H/h_0 = 0.3$) for different time sequences in $4224 \times 128$ mesh resolution model; t= 0.1s, 2.1s, 4.1s, 6.1s, 8.1s, 10.1s, 12.1s, 14.1s, 16.1s, 18.1s from left to right.

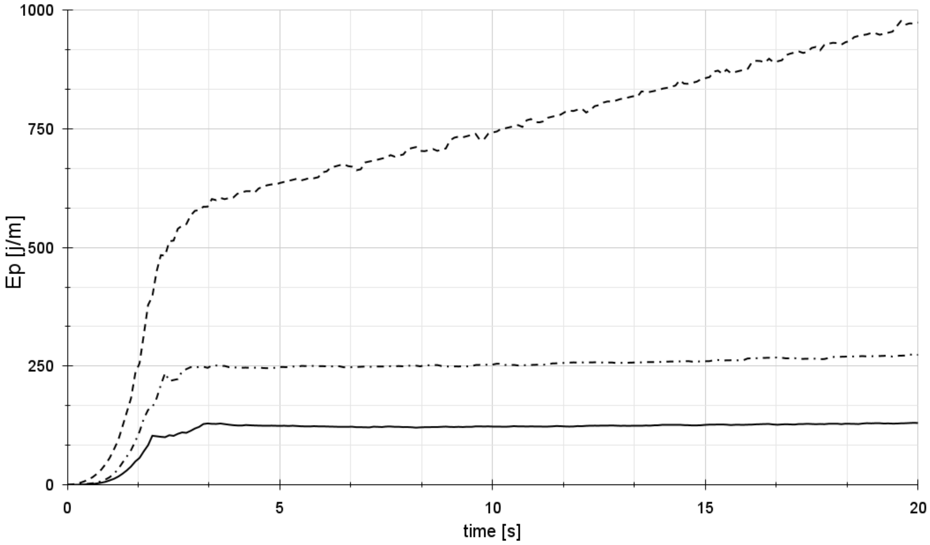

Figure 3.15 – Time variation of the water potential energy restricted to the interface cells ($0.05 < \alpha_w < 0.95$) for different mesh resolution, dashed: $1056 \times 32$, dashdot: $2112 \times 64$ , solid line: $4224 \times 128$.

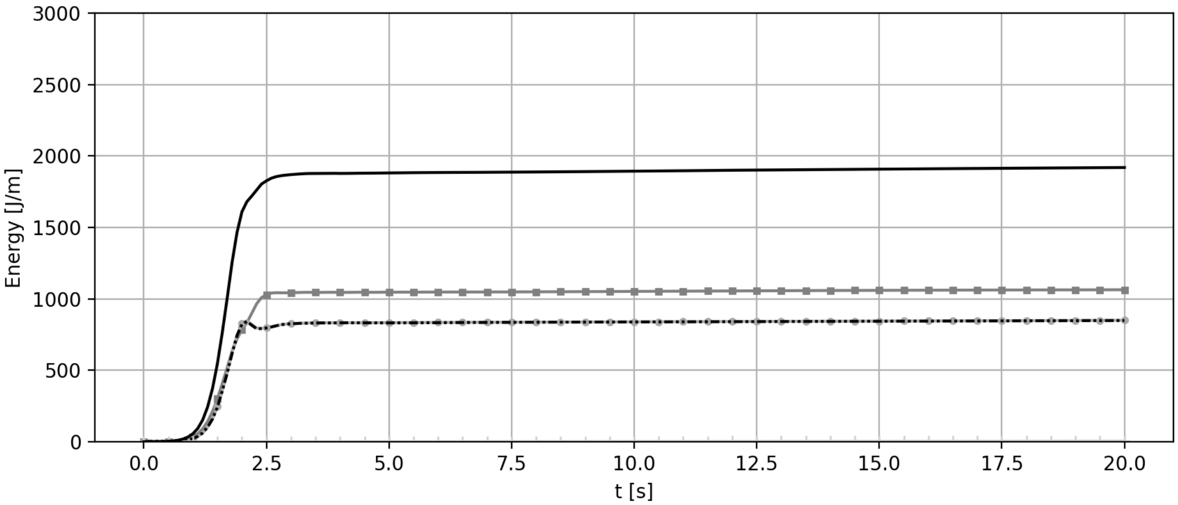

Figure 3.16 – Time evolution of the energy components for the propagating solitary wave case. $H/h_0 = 0.3$ and finest mesh resolution : $4224 \times 128$, solid black line: wave total energy ($E_p + E_k$); grey line with □ mark: wave kinetic energy ($E_k$); grey line with ∘ marks: wave potential energy $E_p$ calculated with Eq. (3.53); dash-dotted line: wave potential energy calculated from the extracted water interface $\eta(x)$; '+': Energy dissipation (negligible in this case).

### 3.3.4.3 CASE 6: Energy conservation in a breaking solitary wave case

Most of the time, a subaerial landslide produces a large wave which is submitted to breaking, either in a gradual way as a turbulent bore or, in a more dramatic way, as a violent plunging breaker. The present section focus on the last case by studying a solitary wave breaking over a slope. To the best of the authors knowledge, there are no theoretical values or measurements giving the amount of energy dissipated in this case. Therefore, the objective here is simply to quantify the amount of energy lost in numerical dissipation and try to minimize this quantity. The physical energy dissipation occurring during the breaking process can be given by two different computations :

1. the difference of the wave energy (potential and kinetic including the TKE), calculated by Equations (3.38) and (3.39), after and before the breaking process,
2. a direct computation of the dissipated energy by integration of the energy dissipation rate given by equation (3.45) .

Theoretically, there should be no difference between the results of the two computations. But practically, there there will be some difference due to discretization errors. Therefore, the difference between the two computations gives an estimation of the numerical dissipation.
The model setup, presented on Figure 3.17, is similar to the experiment described in Li and Raichlen (2003). In this study, a solitary wave propagates over a 10 m flat bottom with a water depth ($h_0$) of 0.3 m. The initial wave height-to-water-depth ratio is ($H/h_0 = 0.3$). After the flat portion, the wave meets a 1:15 slope which induces the breaking and then the run-up of the wave.
The computational domain is made up of two adjacent blocks with the same number of rows and columns for the entire domain. The cell size is constant in the x-direction but gradually skews in the y-direction over the slope (Figure 3.18). The bottom boundary conditions is a no-slip condition.

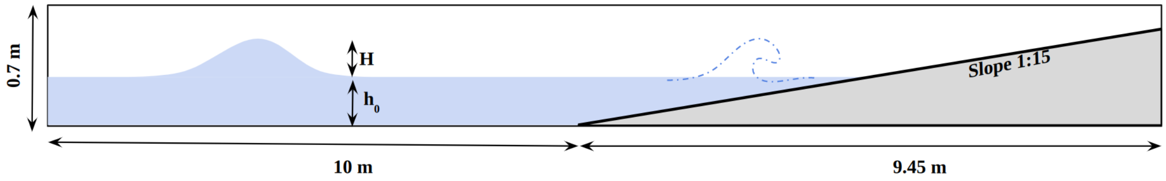

Figure 3.17 – Schematic view of the breaking solitary wave test case (dimensions are not in scale).

For this test case, turbulence model plays a critical role in the energetic balance through the Turbulent Kinetic Energy (TKE) and the TKE dissipation rate $\epsilon$. The following Reynolds-Averaged Navier-Stokes turbulence model types have been considered in the present study :

- standard (linear) $k - \epsilon$
- non-linear $k - \epsilon$
- RNG $k - \epsilon$
- $k - \omega$ SST
- $k - \omega$ SST Buoyancy modified by Devolder et al. (2017)
- $k - \omega$ SST modified by Larsen and Fuhrman (2018)

$k - \epsilon$ and RNG $k - \epsilon$ are common classical models. The non-linear $k - \epsilon$ was found very effective in predicting turbulent kinetic energy profiles for spilling and plunging breaker in Brown et al. (2016). Finally, the $k - \omega$ SST model has been recently modified in Devolder et al. (2017) and Larsen and

Fuhrman (2018) to accurately reproduce the turbulence level in the surf zone. Note that in this test case, the values of the initial turbulent parameters are not critical. Indeed, the time of wave propagation being long before the breaking, these parameters have sufficient time to converge to their physical values.

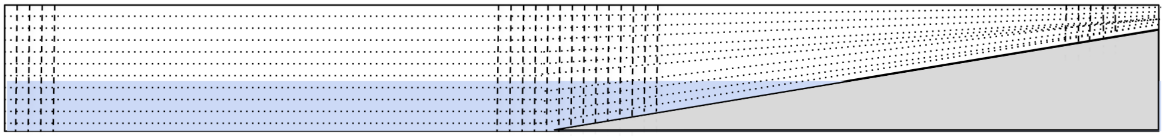

Figure 3.18 – Schematic view of the cell arrangement in the solitary breaking wave test case.

We first verify that the breaking is well reproduced by the model (Figure 3.19).

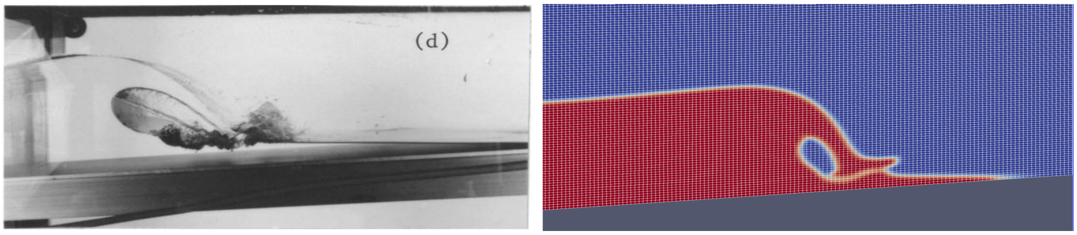

Figure 3.19 – Shape of the wave during breaking in the breaking solitary wave test case ($H/h_0 = 0.4$) on a 1:15 slope, left : snapshot from Li and Raichlen (2003) experiment, right : present simulation with the Devolder et al. (2017) turbulence model.

Figure 3.20 shows the time evolution of different energy components for the $k - \omega$ SST turbulence model Buoyancy modified by Devolder et al. (2017). The wave energy dissipation starts to be non negligible above the slope and increases during the breaking and run-up. This dissipation is mainly due to turbulent processes. Note that during breaking, potential energy is transformed into kinetic energy while during run-up, the reversed process is observed. Figure 3.21 shows the comparison of the physical dissipation and the reverse of the total energy decrease between two different mesh resolutions 5 mm and 2.5 mm cell size.

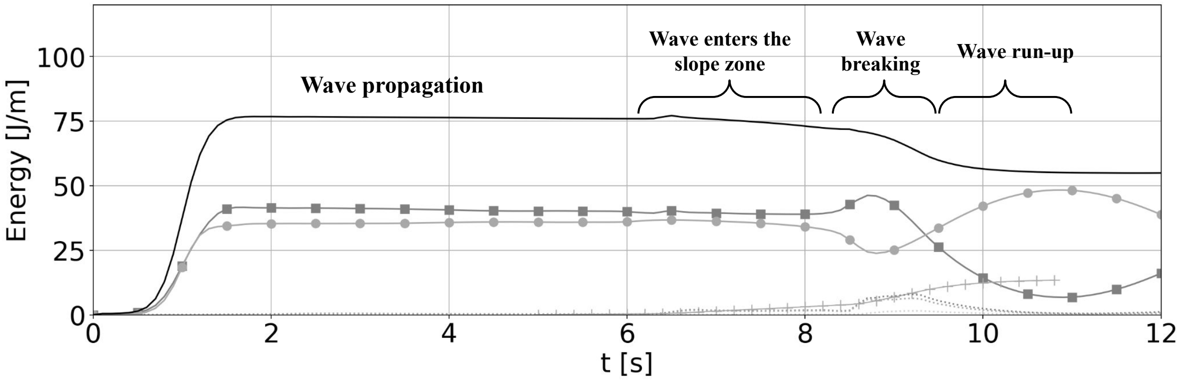

Figure 3.20 – Time evolution of the different energy components for a ($H/h_0 = 0.3$) breaking solitary wave. Turbulence model : $k - \omega$ SST buoyancy modified Devolder et al. (2017), cell size = 5mm. solid line: $E_k + E_p$, grey line with ∘: $E_k$, grey line with □: $E_p$, and grey line with "+": integrated dissipated energy.

The plot starts at t=5 s when the wave is still propagating in the flat-bottom section and ends when the potential energy of the wave starts to decrease, at the end of the run-up. The numerical dissipation increases drastically during the mixing due to the violent breaking on the slope (in this case, the difference between the two curves for 5 mm cell size model (Fig 3.20) is 36% as detailed later in Table 3.10). During the run-up, energy is better conserved, as shown by a stable difference between the two curves. The comparison between the two plots indicates the significant influence of the cell size in achieving a better accuracy in the energy dissipation computation.

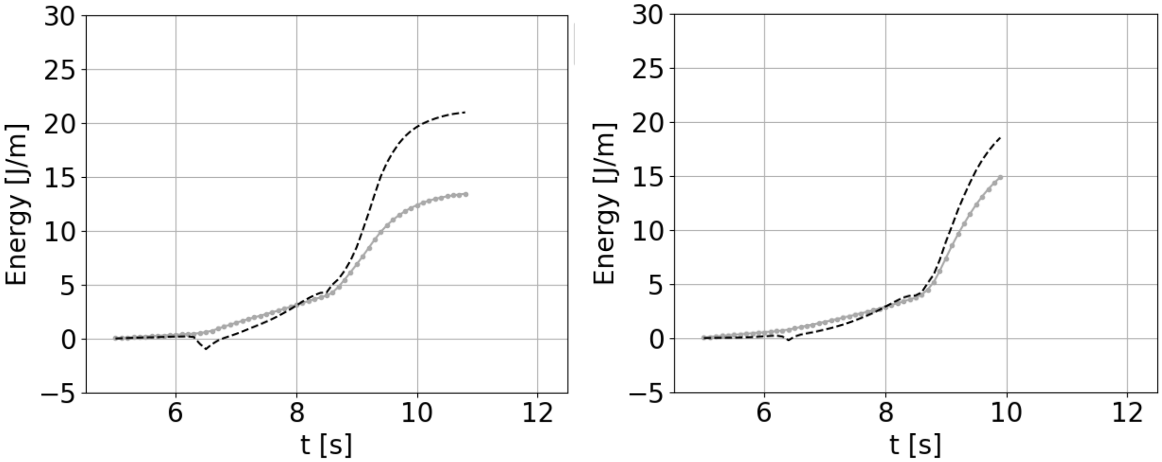

Figure 3.21 – Comparison between the direct computation of the physical energy dissipation (grey line with ∘) and the decrease in total wave energy (black dash line) for the case of Figure 3.20. Note that the last curve has been artificially multiplied by $-1$ to allow a direct comparison. Left panel: for the 5 mm cell size test case, Right panel: same graph for the 2.5 mm cell size test case.

Table 3.10 provides a summary of the results regarding the conservation of energy for the different RANS turbulent models tested. The results show that only the modified $k-\omega$ SST and the $k-\epsilon$ RNG models are able to bound the relative error in the conservation of energy to reasonable values. For those models, the physical dissipation introduced in the turbulence model is lower than the decrease observed in the total wave energy. The decrease in the mesh size allows to reduce the numerical dissipation as illustrated in the case of the Devolder et al. (2017) model but it is obviously at the price of a heavier computation. Note that impulse waves generated by subaerial landslide usually exhibit drastic transformations during their generation and propagation, requiring a large computational domain to be covered in order to properly describe those transformation processes. Therefore, it appears necessary to find a compromise between an acceptable accuracy in the description of the energetic processes and manageable computation times, especially when the computations have to be repeated several times for a parametric study.

Table 3.10 – Solitary breaking wave test case - Summary of the relative error in the conservation of energy for the different RANS models tested.

| Turbulence model | Cells size | $E_{start} - E_{end}$ | $\int_{t=5s}^{t_{max-runup}} \phi \, dt$ | Relative error (%) |
|---|---|---|---|---|
| $k-\omega$ SST(Devolder et al. (2017)) | 2.5 mm | 18.6 | 15.1 | 19 |
| $k-\omega$ SST(Devolder et al. (2017)) | 5 mm | 21.01 | 13.4 | 36 |
| $k-\omega$ SST(Larsen and Fuhrman (2018)) | 5 mm | 20.42 | 14.54 | 29 |
| $k-\omega$ SST | 5 mm | 11.13 | 37.57 | -238 |
| $k-\epsilon$ RNG | 5 mm | 21.47 | 15.68 | 27 |
| $k-\epsilon$ Non-linear | 5 mm | 5.6 | 60 | -971 |
| standard $k-\epsilon$ | 5 mm | 8.8 | 55.35 | -529 |

#### 3.3.4.4 CASE 7: Energy conservation in a progressive bore case

In this section, we study the case of the dissipation of a turbulent bore, a frequent case appearing after a violent breaking of an impulse wave. The bore is generated in a wet dam break process with the same set-up as in Yeh et al. (1989) and Mauriet (2009). The upstream reservoir height is 0.225 m and the downstream height is 0.0975 m (Fig. 3.22). The upstream reservoir is sufficiently large to ensure a steady propagation of the turbulent bore wave until the end of the downstream reservoir.
The turbulence model is the $k-\omega$ SST Buoyancy modified by Devolder et al. (2017). According to Mauriet (2009), the choice of the initial value of the turbulence model variables is critical to represent properly the dissipation. We have conducted several tests to guess the optimal initial values for the model presently used. With `k`=1e-4, `omega`=1, and `nut`=0, the model is found to provide reliable results. The bottom boundary condition is a free-slip condition so that to restrain the dissipation to the breaking processes at the surface and therefore, be able to compare to the hydraulic jump theory. Finally, different uniform meshes are tested to study the influence of resolution in the computation of the dissipation.

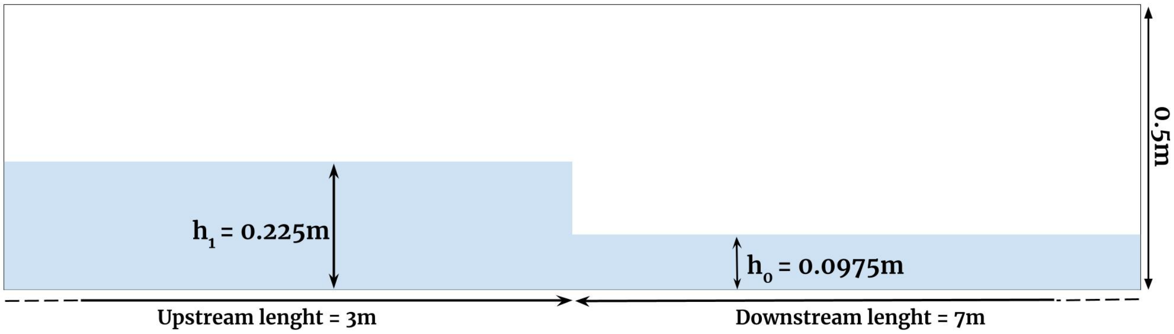

Figure 3.22 – Computational domain used for the study of the progressive turbulent bore from Mauriet (2009).

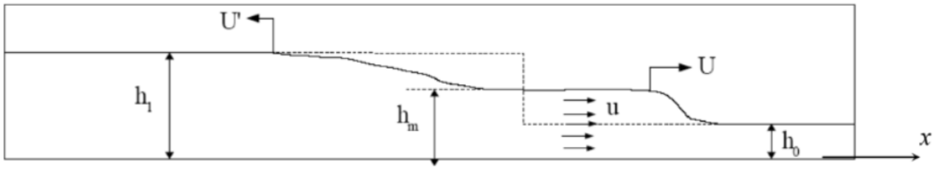

Figure 3.23 – Turbulent bore - definition of parameters from Mauriet (2009).

The theory of the turbulent bore generated in a wet dam break is described in Stoker (1992) §10.6 and §10.8. The shock conditions written around the discontinuity, allows to compute the bore height ($h_m$) (Figure 3.23) :

$$\sqrt{h_1} = \sqrt{h_m} + (h_m + h_0)\sqrt{\frac{h_m + h_0}{8h_m \cdot h_0}} \tag{3.54}$$

In a coordinate system moving at the bore celerity, the flow is stationary. Several balance equations can be written. First, the mass conservation gives : $h_0 U = h_m(U - u)$, hence : $u = U\dfrac{(h_m - h_0)}{h_m}$.
The momentum conservation reads : $\rho U^2 h_0 + \rho g \dfrac{{h_0}^2}{2} - \rho(U-u)^2 h_m - \rho g \dfrac{{h_m}^2}{2} = 0$, which gives : $U^2 = \dfrac{g h_m (h_m + h_0)}{2h_0}$. And finally, the variation of the flow energy through the discontinuity is :

$\Delta E = \{\rho g h_0 + \rho \frac{U^2}{2}\} - \{\rho g h_m + \rho \frac{(U-u)^2}{2}\} = \rho g \frac{(h_m - h_0)^3}{4 h_0 h_m}$ $(J/m^3)$ by using the two previous results. Finally, multiplying by the flow discharge $Uh_0$ gives the dissipation rate : $\Phi = \rho g U \frac{(h_m - h_0)^3}{4 h_m}$ $(J/s)$. With the current set-up, this gives:

- $h_m = 0.154$ [m]
- $U = 1.4$ [m/s]
- $\Phi = 4$ [J/s]

Figure 3.24 shows the results obtained with the model for the turbulent bore test case. On the top panel, we show that the simulated bore height matches the theoretical value, demonstrating that the macroscopic features of the flow are realistic. The bottom panel displays the dissipation computed by the model and the opposite of the energy decrease for different mesh resolutions. The difference between the continuous and the associated dotted lines is the numerical dissipation for the given resolution. This plot shows that the numerical dissipation keeps reasonably bounded for all the simulations but especially for the finer mesh. Moreover, after a transitional regime in the beginning of the simulation (i.e., the first 1.5 s), the dissipation rate calculated by the model (i.e., the slope of the curve) is consistent with the theoretical value. the resolution gradually improving this assertion.

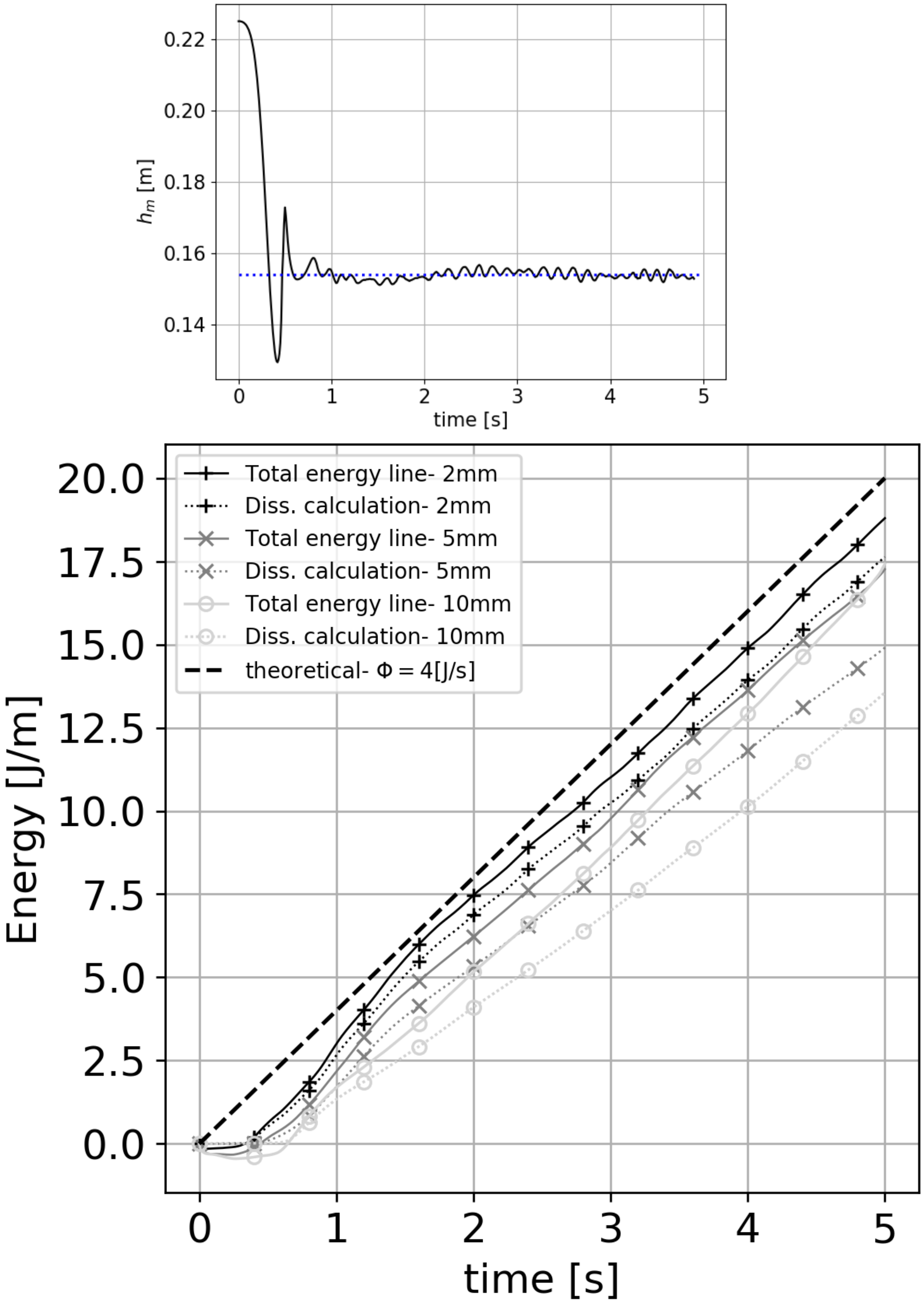

Figure 3.24 – Top panel: comparison of the simulated (2 mm) bore height (taken 60cm behind the bore front) -solid black line- with the expected theoretical value -blue dashed line-. Bottom panel: Comparison between the simulated dissipation -dotted lines- and the opposite of the energy decrease -solid lines- with the expected theoretical value -dashed line- for different cell resolutions.

### 3.3.5 Conclusions and discussion

Our study provided a comprehensive validation of the model OpenFoam (i.e. InterFoam and Multiphase InterFoam), with respect to several important processes involved in waves generated by subaerial landslides including : landslide motion, wave generation by liquid phases interaction, wave breaking inception and wave dispersion. In the mean time, we also tried to investigate energy conservation and quantify the accuracy of the computed dissipation, two aspects largely overlooked in the literature, in the case of a propagating solitary wave, a breaking solitary wave and a turbulent bore. The following conclusions can be drawn from this extensive work :

- The study of the non-newtonian slide propagation cases revealed that approximately 5 numerical cells within the plume thickness, can offer an acceptable level of accuracy in predicting the slide plume propagation speed. Slight discrepancy in the slide front shape with this resolution are nevertheless expected.
- The generation of the wave and the subsequent breaking were correctly reproduced using a fine tuning of the model (i.e., the gate motion) in a dam break case (Jánosi et al., 2004). Approximately 12 cells along the breaking wave height were necessary to obtain this result. Additionally, both two-phase and three-phases OpenFoam solvers were demonstrated to provide very similar results.
- We tried to validate the dispersion processes with the undular bore generation (Soares Frazao and Zech, 2002)with comparable resolutions as in the previous validation cases. The numerical results did not vary significantly with the mesh size and the error was not negligible especially for the wave height. The main frequency of the wave train is more correctly reproduced.
- A few validations cases were devoted specifically to the energetic processes, leading to the selection of an appropriate turbulence model as well as the optimisation of the initial conditions. It was shown that the use of a fin mesh is mandatory to reduce numerical dissipation. But with the CFL constraints, this enhance substantially the CPU time. Therefore a compromise has to be found. Accordingly, with 20 to 25 computational cells over the wave height, we expect the simulations of the wave breaking events to provide an acceptable accuracy in the estimation of the dissipation term.

## 3.4 Numerical experiment

In the following sections, we give preliminary methodological information about the numerical experiments, which results are presented in the next chapter. The model accuracy has been qualified in the previous parts. We now assume that, provided the model setup follows the few recommendations of the previous section, the results can be thought as reasonably accurate. Therefore, the model will be used, now, as a physical experiment to study waves generated by Newtonian and Non Newtonian subaerial landslides.

### 3.4.1 General model set-up

The computational domain is a two-dimensional prismatic tank, 20.3 m long and 1 m high (Figure 3.25 bottom panel). A 45° inclined plane, on the left side of the domain, drives the slide motion for the wave generation.
The simulations are carried out with `"multiphaseInterfoam"` considering three phases (i.e., slide, water, and air). Each phase is initially located in the domain thanks to an individual phase fraction (e.g. `"alpha.water"` for water phase). In the basin, water elevation ($h_0$) is constant and equal to 20 cm. The slide phase is placed over the slope and its characteristics (volume $V_0$ and initial height $h_s$) vary depending on the case. Air completes the two other phases position. The physical parameters of the different phases are presented in the Table 3.11.

Table 3.11 – Physical parameters considered in the numerical experiments

| Parameters | Symbol | Value |
|---|---|---|
| water density | $\rho_w$ | $1000\ (kg \cdot m^{-3})$ |
| air density | $\rho_a$ | $1\ (kg \cdot m^{-3})$ |
| slide density | $\rho_s$ | $[\rho_w$ - $1.338\ \rho_w]$ |
| water kinematic viscosity | $\nu_w$ | $10^{-6}\ (m^2 \cdot s^{-1})$ |
| air kinematic viscosity | $\nu_a$ | $1.48 \times 10^{-5}\ (m^2 \cdot s^{-1})$ |
| slide kinematic viscosity | $\nu_s$ | varies |
| surface tension constant coefficient | $\sigma$ | $0.07\ (N \cdot m^{-1})$ |

A uniform mesh is employed to avoid non-orthogonality and skewness of mesh cells, which are recognized as a challenge for most VOF algorithms. Taking into account the conclusions of the validation study and according to the wave features expected in our numerical experiment (observed between 0.01 and 0.27 m), we selected two cell sizes: 2.5 mm and 5 mm, each with an aspect ratio of one. The smaller mesh size, 2.5 mm, is applied in cases involving the smallest waves to ensure that the mesh resolution adequately captures the wave amplitude. The mesh is generated, first with `"blockMesh"` and, then with `"snappyHexMesh"`. In total, It is composed of maximum 1,251,120 hexahedral cells and 160 prism-shaped cells (Figure 3.25, top panel).
The walls, slope, and bottom boundary conditions are set to "noSlip" for the velocity field and zero-flux for the other fields. The top boundary is an open atmosphere. The total simulation duration is set to 12 s which is sufficient to cover the full wave propagation through the tank for most of the cases. The data output is carried out every 0.05 second.
As for the two-phase flow, it is possible to quantify the numerical dissipation induced by the model for three-phase simulations. On one hand, the evolution of the total mechanical energy of the system

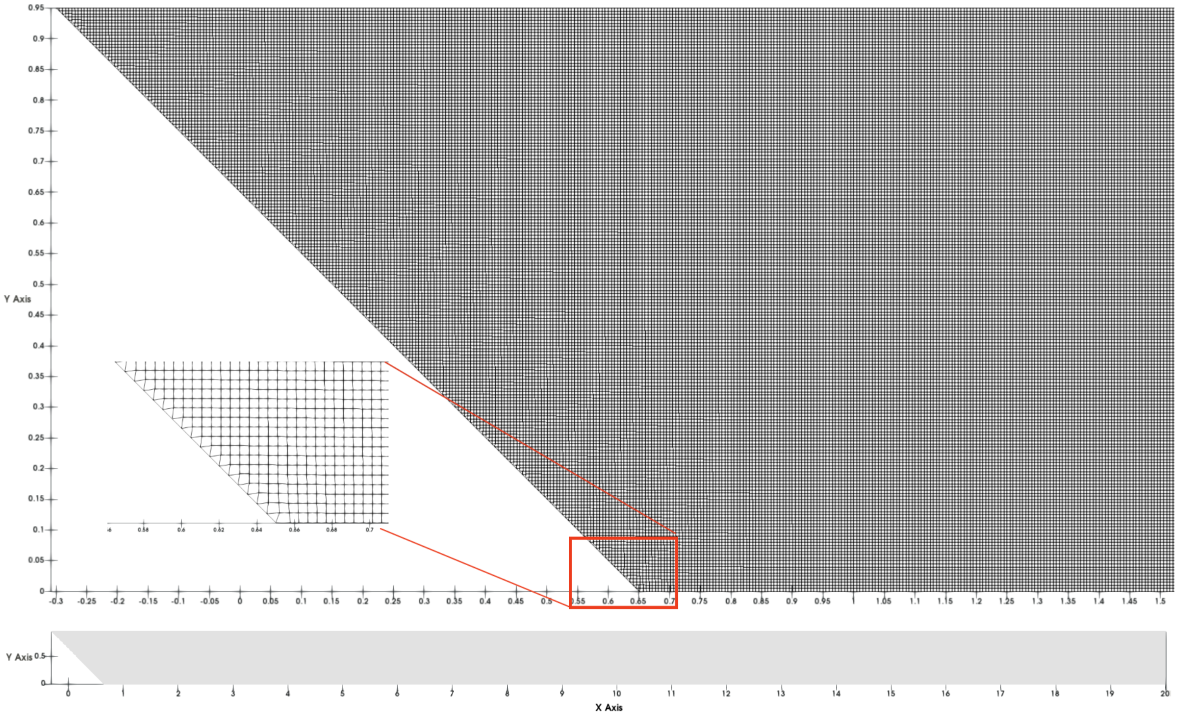

Figure 3.25 – Computational domain used for the numerical experiment. Top panel : detailed view of the mesh arrangement around the slope, Bottom panel : sketch of the numerical tank.

is equal to the sum of all the energy components for all the phases (slide, water, and air), namely : $E_{k,water} + E_{p,water} + E_{k,slide} + E_{p,slide} + E_{k,air} + E_{p,air}$. On the other hand, the physical energy dissipation is the time integration of the dissipated energy rate in each phase, namely : $\int \phi_{water}\, dt + \int \phi_{slide}\, dt + \int \phi_{air}\, dt$. For the various tests we have carried out on this question, it appeared clearly that the numerical scheme used for the convective terms is critical. As an illustration, we compare in Figure 3.26 the performance of the 2nd order "linearUpwind" differencing scheme and 1st order "Upwind" scheme in terms of numerical dissipation. The latter is unconditionally stable but it is also known to be highly diffusive. In these simulations, featuring two different water slides volumes ($h_s = 2h_0$ and $h_s = 2.5h_0$) without initial elevated slide, the waves are breaking violently after their generation. The figure shows that, in these cases, the numerical dissipation take significant values for both schemes. With the LinearUpwind scheme, the final numerical dissipation is respectively 23% and 13% for the two slide cases. With the Upwind scheme, it reaches 58% for the $h_s = 2h_0$ case.

As pointed previously in section 3.1.1, the stability of the model is ensured provided that the convective and diffusive stability conditions are both respected. Indeed, as highlighted by Rauter et al. (2020), in case of violent breaking, the most common case in our simulation, it is, therefore, expected the most critical $CFL_{diff}$ values in those highly turbulent flows, the eddy viscosity term ($\mu_t$) being predominant in equation (3.11).

Here, we impose a very restrictive conditions on the convective CFL (i.e., $\text{CFL}_{conv} = 0.1$) and verify *a posteriori* that the diffusive CFL condition is indeed respected. Figure 3.27 shows the time evolution of the maximum CFL numbers attributed to the convection and diffusion terms for an energetic slide case. The model would be unstable in the grey area. As expected, the $CFL_{conv}$ value of 0.1 imposes a sufficiently strict condition to ensure that the diffusive CFL number remains within the stable range ($CFL_{diff} < 1$) for the entire simulation.

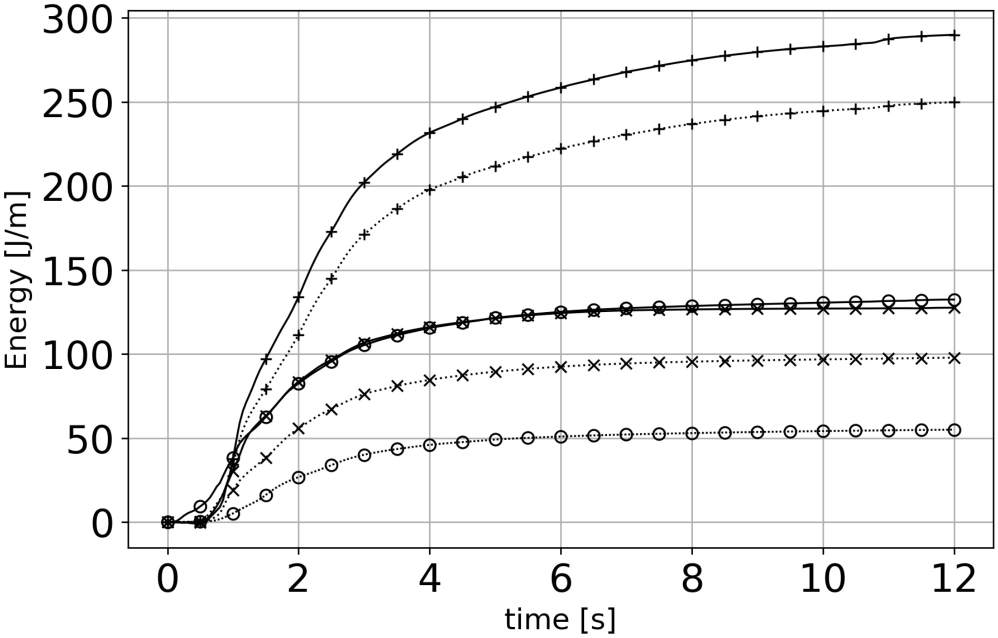

Figure 3.26 – Comparison between total energy decrease (solid lines) and the computed energy dissipation (dotted lines) over time for different water slide cases (no initial elevated slide) and convective terms discretization. (+) : $h_s$=2.5$h_0$ and linearUpwind, (×) : $h_s$=2$h_0$ and linearUpwind, (○) : $h_s$=2$h_0$ and Upwind.

Nevertheless, this condition is very strict and strongly reduces the time step of the simulation. This prevent us from using finer meshes than the one proposed at the beginning of this section, even though the numerical dissipation is expected to be non negligible for this mesh. Finally, the choice of the spatial model resolution is a compromise between the reduction of the artificial dissipation, the respect of the stability criteria and a manageable total simulation duration (considering the planned large number of simulations). To sum up, Table 3.12 shows the final model setup retained for the numerical experiment of the next chapter.

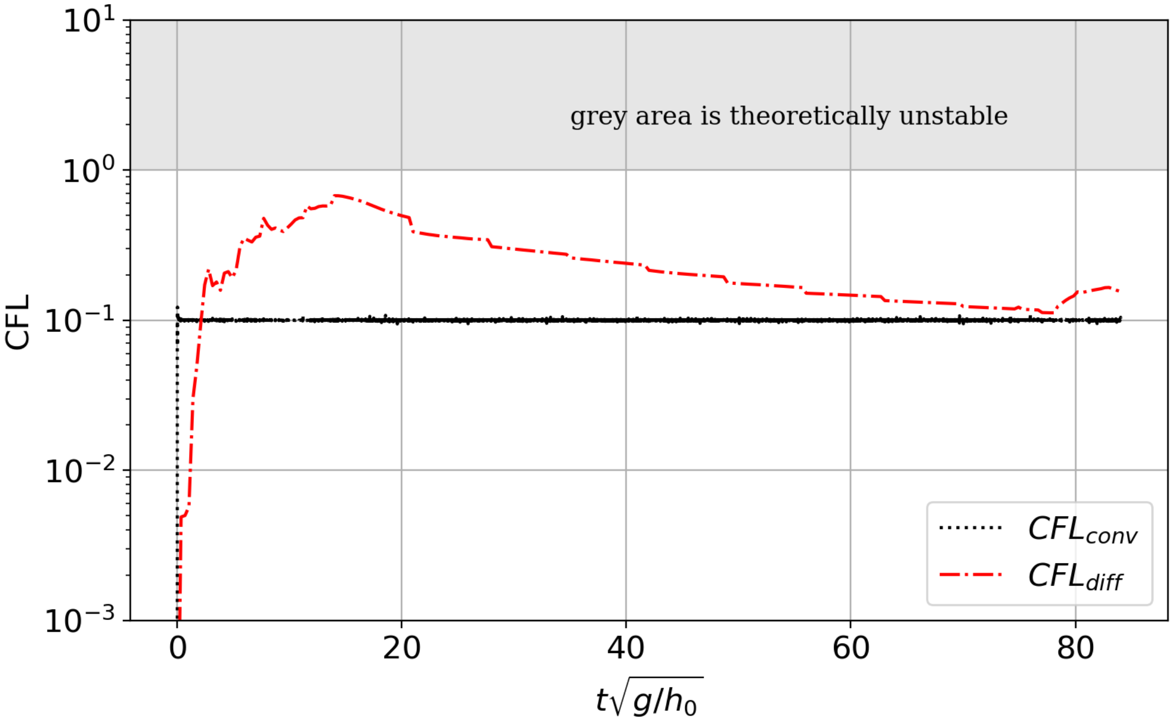

Figure 3.27 – Time evolution of the CFL-numbers related to convection and diffusion terms for an energetic slide case ($h_s = 2.5h_0$ and no initial elevation for slide).

Table 3.12 – Summary of model setup used in the numerical experiment.

| | | |
|---|---|---|
| Solver/ method | multiphaseInterfoam/RANS-VOF | |
| No. phases | 3-phases | `alpha.sed/alpha.water/air.water` |
| water depth ($h_0$) | 0.2 m | - |
| mesh resolution | 2.5/5 mm | - |
| Domain length/height | 20 m × up to 1.05 m | slope angle = 45 degrees |
| BC for `U` field | `noslip`/`pressureInletOutletVelocity` | walls, slope, bottom/top |
| BC for `p` field | `fixedFluxPressure`=0/`totalPressure`=0 | walls, slope, bottom/top |
| BC for `alpha.*` field | `zeroGradient`/`inletOutlet`=0 | walls, slope, bottom/top |
| Turbulence model | k-$\omega$ SST Buoyancy modified | initial values: `k=1e-4, omega= 1, nut= 0` |
| Duration/$\Delta$t/ CFL | 12 s/ 0.01 s/ 0.1 | output frequency: 0.05 s |
| gradient scheme | `linear` | `grad(U), grad(gamma)` |
| divergence scheme | `linearUpwind` | for `div(rhoPhi,U)` |
| Laplacian scheme | `linear corrected` | - |

### 3.4.2 Model set-up for the different phases of this work

In the following, we present the different model set-up for the different phases of this work as introduced in section 2.9 and illustrated in figure 2.11.

#### 3.4.2.1 Phase I: water slide of different volumes with no initial elevation

In this setup, the slide, made up of water, is located adjacent to the water free surface (Figure 3.28), and therefore, enters the basin without initial speed.

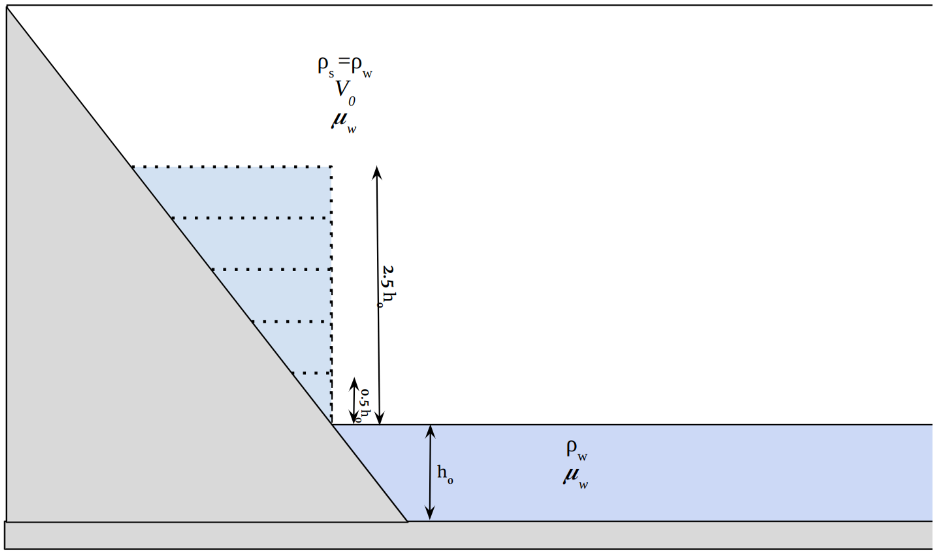

Figure 3.28 – Schematic view of model setup model for the phase I study.

The slide height varies from $0.5h_0$ to $2.5h_0$ with a $0.25h_0$ step. Table 3.13 represents the initial height, mass, and potential energy for the different scenarios simulated.

Table 3.13 – Water-water cases scenarios.

| Case-$h_s$ | Mass ($m_0$) [kg/m] | $E_0^\dagger$ [J/m] |
|---|---|---|
| $0.5h_0$ | 5 | 3.3 |
| $0.75h_0$ | 11 | 11.1 |
| $1h_0$ | 20 | 26.5 |
| $1.25h_0$ | 31 | 51.6 |
| $1.5h_0$ | 45 | 88.9 |
| $1.75h_0$ | 61 | 140.9 |
| $2h_0$ | 80 | 210 |
| $2.25h_0$ | 101 | 298.9 |
| $2.5h_0$ | 125 | 403.5 |

† The reference altitude is the basin's still water level.

In the phase I, we intend to :

- describe the evolution of the impulse wave parameters (amplitude, wavelength, period, celerity, etc.) depending on the slide volume,
- investigate in detail the energetic processes at stake during wave generation and wave transformation including breaking,
- study the respective role of dispersion and dissipation by breaking in the final wave characteristics.

#### 3.4.2.2 Phase II: Newtonian highly viscous slide

This is a first step in our progressive investigation of the role of the slide rheology on the generated impulse wave. Here, the slide is assumed to be Newtonian with the density of water. The setup is similar to the previous one (i.e., Phase I: water-water case) but only one slide volume is considered ($h_s$=$2h_0$). The slide viscosity is varied in order to cover a large range of slide Reynolds numbers $Re_s = \dfrac{\sqrt{g\,h_s} \cdot h_s}{\nu_s}$ as defined in Paris et al. (2021) (from Reynolds number equals to 1120000 (for water) to 10 (very viscous)).

#### 3.4.2.3 Phase III: slides governed by the Herschel-Bulkley law - influence of the rheological parameters on the impulse wave

Phase III considers a visco-plastic slide governed by the Herschel-Bulkley law (Equation (2.16)). In this phase, the model setup is similar to one of the previous sections. The objective here is to progressively study the role of the rheological parameters in the generation of the impulse wave. We first investigate the influence of the yield stress considering a Bingham fluid ($n = 1$) and then varies the value of the power-law index $n$ keeping the other parameters constant.

#### 3.4.2.4 Phase IV: realistic non-newtonian slide with initial elevation

This setup is similar to the previous case, except that, in this case, the slide is placed at different heights with a positive submergence ($h_l$) (Figure 3.29). Therefore, in this configuration, the slide impacts the water basin with a non-zero velocity and a deformed shape. Two slide volumes are considered ($h_s = h_0$ and $h_s = 2h_0$).

In this scenario, the slide rheology follows the Herschel-Bulkley model with parameters corresponding to a real clay-water mixture as documented in Huang and García (1998). These parameters are presented in Table 3.14.

In this phase, the objective is to document the slide shape and velocities at the impact time and study their relation with the energy transfer mechanism and the parameters of the impulse wave. The different test cases of this phase are summarized in Table 3.15.

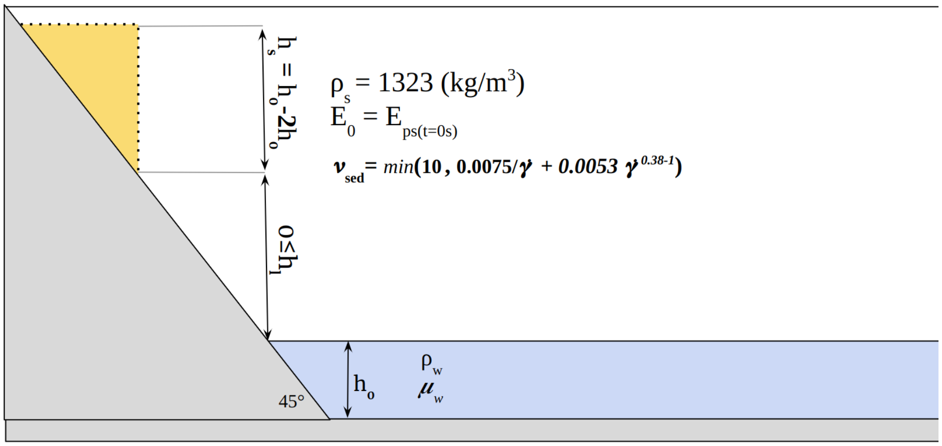

Figure 3.29 – Schematic view of the model setup for the cases with initial elevation.

Table 3.14 – slide parameters used in phase IV.

| **parameters** | **value** |
|---|---|
| $h_s$ | $h_0$, $2h_0$ |
| $h_l$ | $0 < h_0 < 2.5h_0$ |
| density | 1323 [kg/$m^3$] |
| $\tau_0$ | 9.96 [$Pa$] |
| $n$ | 0.38 [-] |
| $k$ | 7.1 [$Pa \cdot s^n$] |

Table 3.15 – Rheological case scenarios with intial elevated slides information.

| $h_s$ | $h_l$ | Mass [kg/m] | $E_0^{\dagger}$ [J/m] |
|---|---|---|---|
| $h_0$ | 0 | 26.46 | 34.6 |
| $h_0$ | $0.25h_0$ | 26.46 | 47.6 |
| $h_0$ | $0.5h_0$ | 26.46 | 61 |
| $h_0$ | $0.75h_0$ | 26.46 | 75 |
| $h_0$ | $1h_0$ | 26.46 | 88 |
| $h_0$ | $1.25h_0$ | 26.46 | 101 |
| $h_0$ | $1.5h_0$ | 26.46 | 114 |
| $h_0$ | $1.75h_0$ | 26.46 | 127 |
| $h_0$ | $2h_0$ | 26.46 | 140 |
| $h_0$ | $2.5h_0$ | 26.46 | 166 |
| $2h_0$ | 0 | 105.84 | 278 |
| $2h_0$ | $0.5h_0$ | 105.84 | 382 |
| $2h_0$ | $1h_0$ | 105.84 | 486 |
| $2h_0$ | $1.5h_0$ | 105.84 | 590 |
| $2h_0$ | $2h_0$ | 105.84 | 690 |

† The reference altitude is the basin's still water level.

# Chapter 4

# Results and discussion

This chapter presents and analyses the results obtained for the cases discussed in the previous chapter. In the last chapter, we concluded the applicability of our numerical method for the study of landslide-induced impulse waves. Section 4.1 and 4.2 present the results of the model scenarios provided in section 3.4.2 are presented, namely the 4 phases of figure 2.11. In section 4.3, we gather all the cases studied previously to find a common way to explain relative energy efficiency transformation.

## 4.1 Phase I: water slide

In this part, the slide volume is varied and the submergence is zero. The objective is to investigate the wave processes from the generation to the end of the transformation phase.

### 4.1.1 Preliminary observations

Figure 4.1 presents the comparison of the waves generated by two different volumes. Clear differences are observable. On the left, the large slide volume generates an extremely large wave which immediately breaks, inducing a significant turbulent dissipation. On the right, the smaller volume generates a smaller wave with a slight and localized breaking and a dispersive wave trail.

Table 4.1 gives a summary of all the qualitative differences which are obvious from these first set of simulations.

Globally, the phenomenon can be divided in classes, they were already pointed out in section 2.5. In the so-called "generation zone", the slide is still actively involved in the wave growth. This zone, complex to define, requires a dedicated in-depth study presented in the next section. The subsequent zones, after the "generation zone", include the "near-field" and "propagation" zones. The duration (or extent) of each zone is case-dependent.

Figure 4.2 provides an illustrative example of these features for a significant slide volume (i.e., $h_s = 2h_0$). The "Near-field" zone starts at the detachment of the leading wave from the slide motion and the strong increase of dissipation at the leading wave crest. In the study of our simulations, we observed two subclasses in the near field zone which we named : "transition" or "strongly breaking" and "weakly

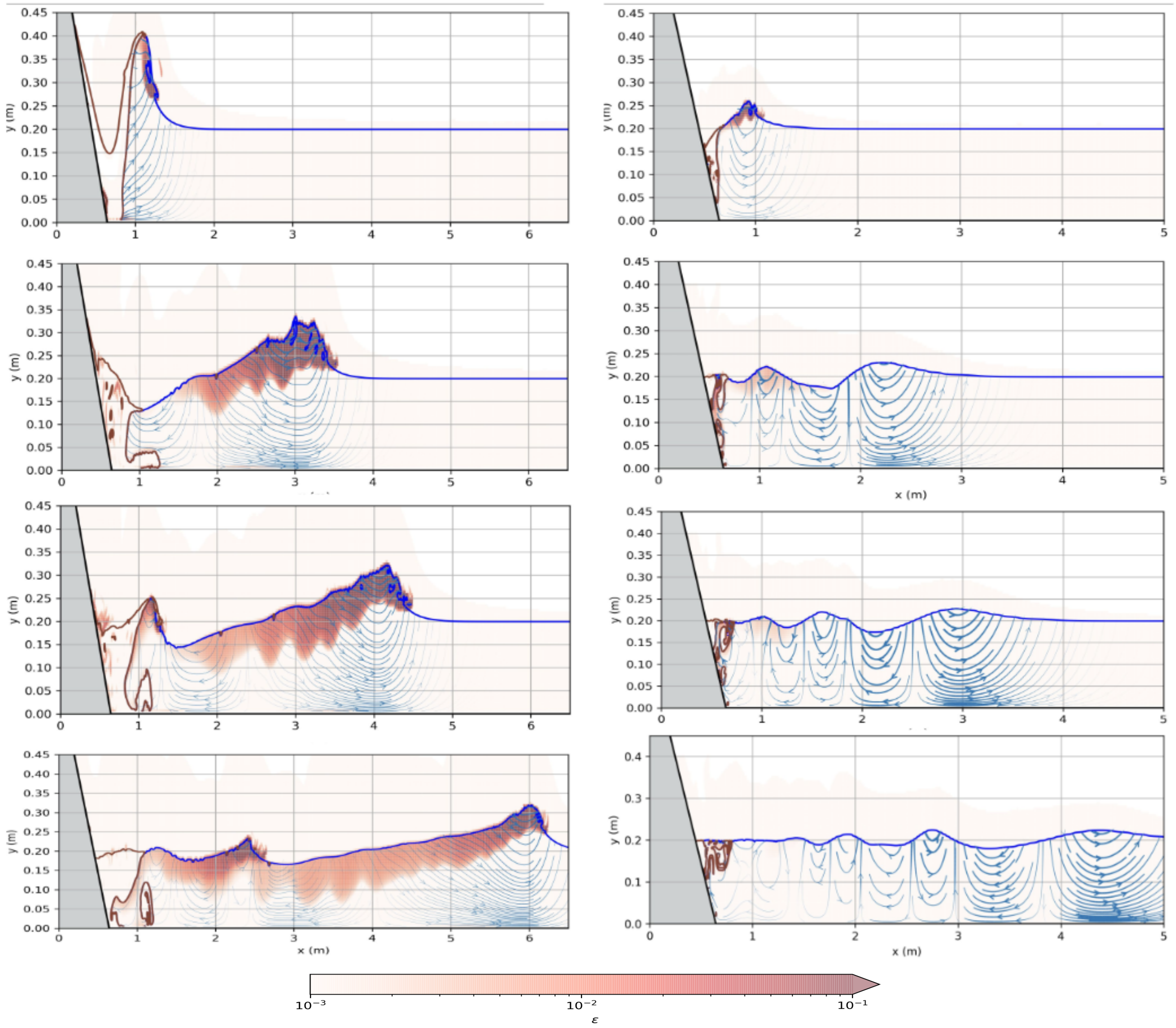

Figure 4.1 – Water slide with no submergence. Snapshots of fluid interfaces, streamlines and turbulent dissipation rate $\epsilon$ (surface field), at t = 0.5 s, 1.5 s, 2 s, 3 s (from top to bottom). Left: $h_s = 2h_0$, right: $h_s = 0.75h_0$ with $h_s$ slide initial height and $h_0$ water depth.

breaking" sub-zones. The primary difference between these sub-zones lies in the wave shape and the magnitude of the turbulent dissipation. In the "transition zone", named in analogy with the outer surf zone (Nairn et al., 1990), the free surface is the direct result of the plunging breaking. It usually exhibits several splash-ups (Lubin et al., 2006) associated with a maximum turbulent dissipation distributed under a large portion of the wave crest. On the other hand, in the "weakly breaking" sub-zone (in analogy to the inner surf zone), the splash-ups are no longer present, the dissipation rate is lower but still present. The waves resemble spilling breakers or turbulent bores depending on the amplitude to depth ratio.

Then, the leading wave undergoes a gradual transition from the "weakly breaking" state to the "propagation" state. This transformation is marked by notable changes in the wave profile, transitioning from a pointed shape to a smoother crest form. Additionally, turbulence generation at the crest ceases. This indicates that the wave approaches a quasi-stable condition in terms of amplitude and propagation celerity, resembling the characteristics of a solitary wave. Note that the previously generated $\epsilon$ field does not disappear immediately but rather remain for a while transported by the wave. As a result,

Table 4.1 – Qualitative differences of general wave characteristics for small and large slide volumes.

| large volume | small volume |
|---|---|
| strong momentum transfer | small momentum |
| large initial wave amplitude | small initial wave amplitude |
| violent and long breaking | short breaking |
| more dissipation | less dissipation |
| less dispersion | more dispersion |
| higher celerity | smaller celerity |
| longer wavelength | shorter wavelength |

slight amount of energy dissipation is still expected.

Finally, for the cases with small slide volumes, the breaking process ends quickly and then the propagation phase quickly starts.

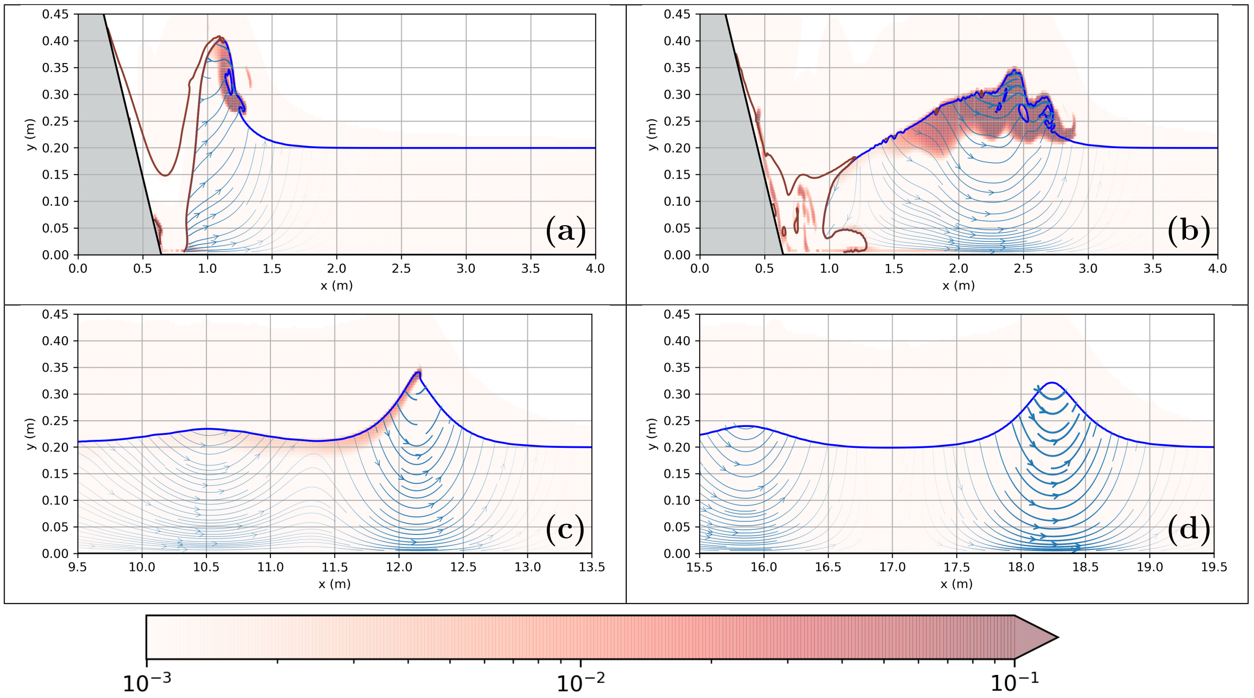

Figure 4.2 – Snapshots of the fluid interfaces, streamlines, and turbulent dissipation rate $\epsilon$ around the leading wave at different zones of the process for water slide with $h_s = 2h_0$. (a): Generation zone at t=0.5 s, (b): Transition sub-zone at t=1.15 s, (c): Weakly breaking sub-zone at t=6.5 s, (d): Propagation zone at t=10 s.

### 4.1.2 Generation stage

The generation process starts as soon as the slide interacts with the water free surface. Few studies have shown that, for subaerial slides, the generation phase is generally very quick. Nevertheless, usually, the end of the generation phase is not really identified in these studies (see section 2.5.1). More generally speaking, there is still a lack of a proper criterion for the determination of the generation stage ending time.

In this section, we try to propose a few indicators to help the definition of this important phase. Figure 4.3 defines the few parameters introduced for that purpose.

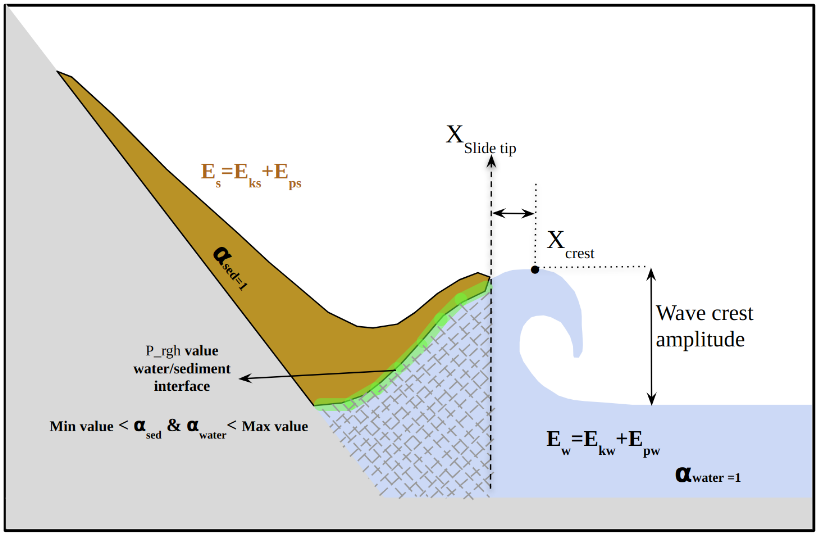

Figure 4.3 – Parameters definition for the study of the generation zone.

An obvious relevant proxy to witness the generation stage ending could be the wave amplitude. It generally grows from zero to a maximum value, time which could be considered as the end of the generation.

Given that generation is intricately linked to the energy transfers between the slide and the water free surface, the termination of this phase could be defined as the conclusion of this process. We shall see later in the document, that such a criterion is not always easy to use due to the superimposition of several processes (i.e., energy transfer from slide to wave and wave dissipation) and the challenge in accurately estimating the wave energy content during its formation.

The dynamic pressure field (`p_rgh` field[1]) at the interface between the slide and the water interface, could also serve as a potential proxy for the momentum transfer between these phases.

The distance between the wave crest and the slide tip might also be indicative to determine the end of the generation. We may consider that both entities are dynamically independent when the leading wave is fully detached from the slide or when the celerity of the slide tip clearly differs from the wave celerity.

We propose in Figure 4.4 an example of the time variation of these parameters. These plots have been obtained in a simulation involving a slide with a significant volume.

With the initiation of the slide motion, a rapid increase is observed for the pressure at the interface, the wave amplitude and the wave energy. The average pressure shows a very quick peak around $t^* = 1.75$ (t= 0.25s) then decreases to a stable value around $t^* = 10.5$ (t= 1.5s). This curve is the witness of the

---

[1] `p_rgh` represents the dynamic pressure resulting from the total pressure field value (`p`) decreased by the hydrostatic pressure ($\rho \cdot g \cdot z$) field.

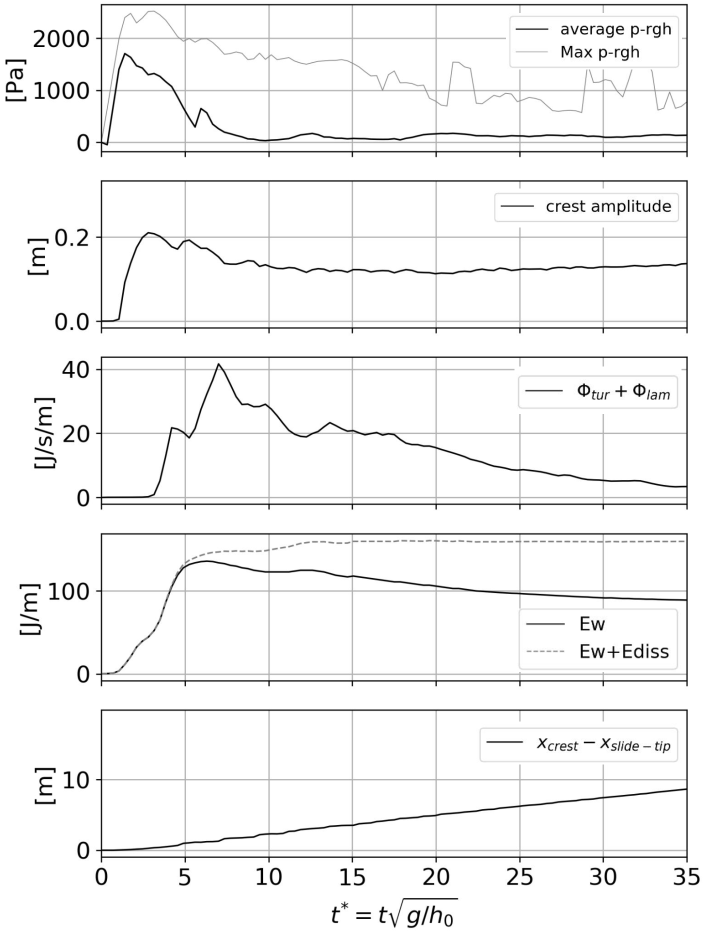

Figure 4.4 – Evolution of indicative parameters during the generation phase. (water slide initial height $h_s = 2h_0$). From top to bottom : dynamic pressure at the slide/water interface, wave crest amplitude, water energy dissipation rate, total wave energy and horizontal distance between the wave crest and slide tip

energy transfer to water, with a sudden increase just after the impact and a progressive decrease due to the slide slowing down.

The wave amplitude follows approximately the same trend but slightly delayed. Interestingly, the wave dissipation due to breaking starts at $t = 0.5s$ while the pressure at the interface is obviously still pushing water. This dissipation is maximum around $t^* = 7$ before the end of the pressure phase. This dissipation translates into the wave energy evolution which starts to decrease around $t^* = 5.6$. Meanwhile, the total wave energy (i.e., taking into account the energy dissipated), which is the witness of the slide transfer, continuously increases. Finally, the wave detaches from the slide around $t^* = 10.5$. This example shows that the maximum wave amplitude or the maximum wave energy are not indicative of the end of the generation phase. The pressure at the interface may be a good proxy to witness the momentum transfer. Note that the interface sometimes shows very complex patterns which makes the interpretation complex (slide entrained in the breaking motion for instance). The wave relative position with respect to the slide tip indicates if the wave is still close to the slide/water interface, but also, considering both celerities, if their motions are disconnected.

Therefore the generation phase needs several criteria to be fully understood, due to the coexistence of positive (generation) and negative (dissipation) energy flux within the wave as well as the difficulty to determine whether the energy flux through the water/slide interface feeds the leading wave, entirely or only partially (which also has to do with the chronology of the slide and wave disconnection).

In the following, we propose another alternative based on a momentum flux calculation. The reasons behind this approach are explained hereafter.

At $t = 0$, the water body and the slide are at rest. All the forces on the water bodies are in equilibrium. These forces include the gravity and the pressure forces on the water contour. As soon as the slide is released, there is a momentum flux through the slide/water common interface (figure 4.5). This momentum flux represents the exchange of momentum from slide to water. As a result, the momentum in the water body gradually increases. The time derivative of the water momentum gives the pressure force acting at the slide/water interface. Additionally, we assume that most of this momentum exchange goes to the free surface waves. Hence the idea of studying the relationship between the momentum flux through the slide/water interface, which is essentially a slide related quantity, to the wave energy.

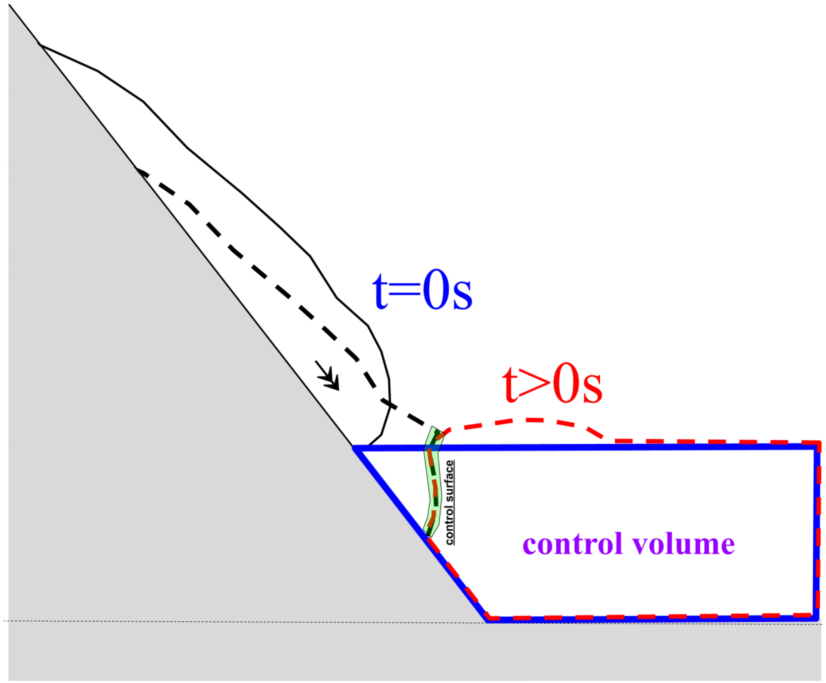

Figure 4.5 – Illustration of the momentum transfer through the slide water interface and control volume considered.

For a proper computation of the momentum flux, the first requirement is the definition of the slide/water interface. In the VOF model, the interface is modelled by the gradient of the phase volume fraction (see Section 3.1.1), transitioning from 1 to 0 within the interface area. Nevertheless, due to numerical diffusion, this transition may exhibit a thickness of several mesh cells depending on the VOF method used.

An example of the variation of the interface thickness is given in Figure 4.6 for one of our simulation. Here the interface is defined with a parameter $\Delta\alpha$ such that $\Delta\alpha < \alpha_{water}, \alpha_{sed} < (1 - \Delta\alpha)$. We test different values of this parameter to find the optimum allowing to locate the whole interface with only one cell. As pointed out in the figure, a relatively large value does not adequately cover the interface length, whereas a very small value leads to an artificially thick interface. The optimum situation is found for $\Delta\alpha \approx 0.2$.

Once the interface zone is delineated, the momentum flux can be computed. The following discretized formulation is employed for cells satisfying $0.2 < \alpha_{water,slide} < 0.8$ (Figure 4.7) :

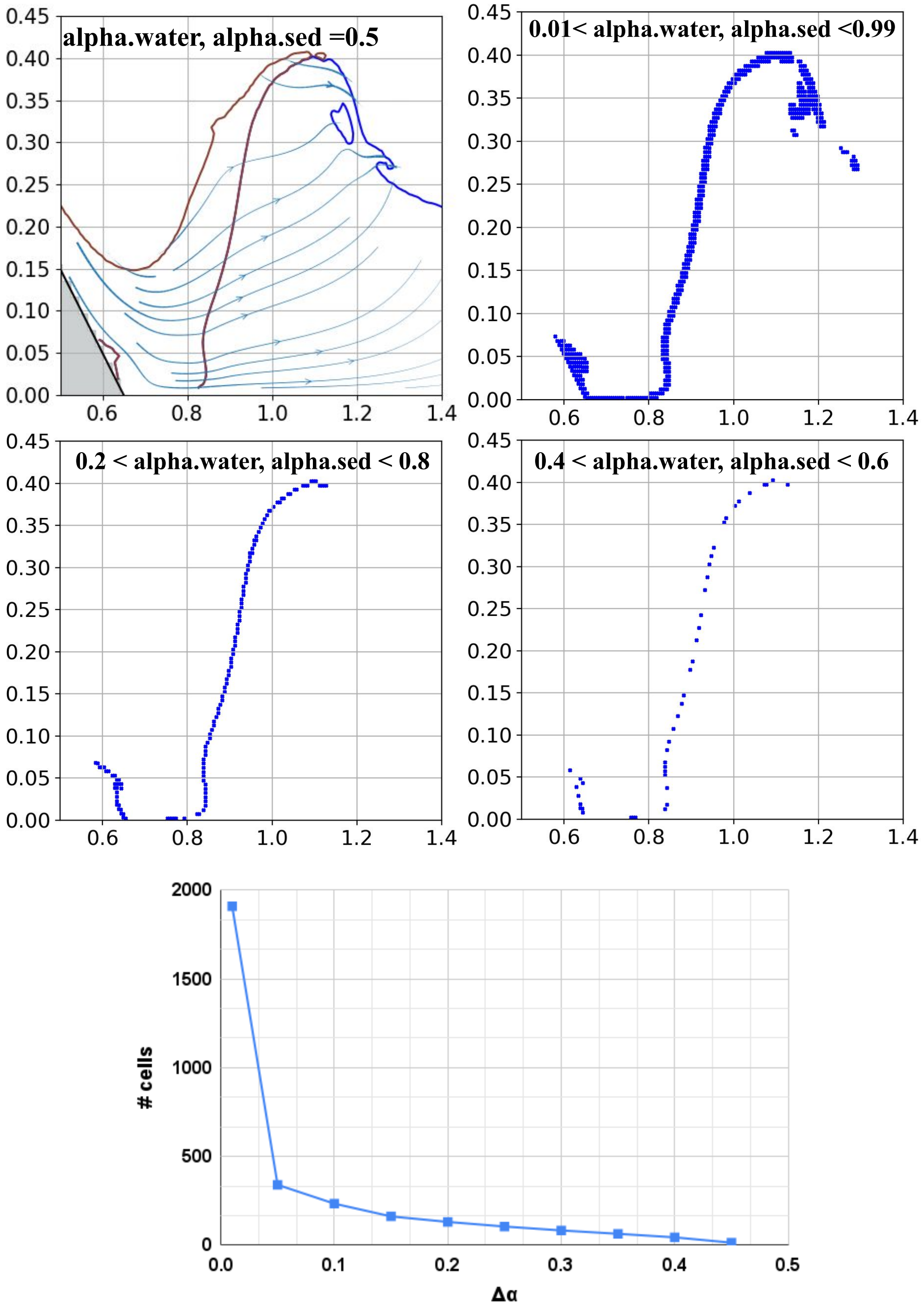

Figure 4.6 – Illustration of the artificial thickness of the slide/water interface for a simulation involving an initial slide height $h_s = 2h_0$. Top panel : Snapshots at $t = 0.5s$ showing the number of cells concerned depending on the interface definition chosen. Bottom panel : plot showing the variation of the number of cells in the interface zone and $\Delta\alpha$ with an interface defined as $\Delta\alpha < \alpha_{water}, \alpha_{sed} < (1 - \Delta\alpha)$

$$\vec{\mathbf{F}} = \sum_{i,j} \left[ \bar{\rho}(i,j) \cdot \vec{\mathbf{U}}(i,j) \cdot (\vec{\mathbf{U}}(i,j) \cdot \vec{\mathbf{n}}(i,j)) \right] \cdot ds(i,j) \tag{4.1}$$

With :

- $\vec{\mathbf{F}}$ : Total momentum flux through the slide water interface (or equivalently slide resulting force on water),
- $\vec{\mathbf{U}}(i,j)$ : local velocity in the mesh cell (i,j),
- $\bar{\rho}(i,j)$ : average cells density depending on the relative share of slide and water in the cell,
- $\vec{\mathbf{n}}(i,j)$ : unit normal vector to the slide/water interface, calculated with the gradient of the $\alpha_{water}$ field (i.e., $\vec{\mathbf{n}}(i,j) = \dfrac{\nabla \alpha_{water}}{|\nabla \alpha_{water}|}$),
- $ds(i,j) = d_{xy} \cdot d_z$ is an approximation of the local slide/water interface surface within the cell $(i,j)$. $d_z$ is the lateral dimension (i.e., here one meter). $d_{xy}$ is the local surface segment in the $xy$ plane. It is calculated by considering that the surface is perpendicular to $\vec{\mathbf{n}}(i,j)$ and should fit within a square cell of side $dx = dy$. Finally, $d_{xy} = \min\left(\sqrt{2}\,dx,\ \dfrac{dx}{\cos\left(\arctan\left(\frac{\vec{\mathbf{n_j}}}{\vec{\mathbf{n_i}}}\right)\right)}\right)$.

$\vec{\mathbf{F}}$ is decomposed into four components ($F_{x(+)}$, $F_{x(-)}$, $F_{y(+)}$, $F_{y(-)}$) with $F_x$ and $F_y$ respectively, horizontal and vertical component of the vector, and $(+)$ and $(-)$, indicating the orientation of the vector (e.g., $F_{x(+)}$ is pointing to the right and $F_{y(-)}$ is downward). This decomposition allows to differentiate, for instance for the horizontal direction, the resulting rightward flux from the leftward one; and similarly for the vertical direction (in this case upward versus downward). The process studied being a two-way process (i.e., energy transfer from slide to water and vice versa), this decomposition allows to better understand the relative contribution of the slide and the water.

As an example, Figure 4.8 shows the time evolution of these four components for two different slide volume during the wave generation process. In these cases, obviously, $F_{x(+)}$ is predominant over the other components and can, therefore, be considered as the primary factor of the wave generation. The time evolution of this variable is also characteristics of the generation process. Indeed, the momentum flux $F_{x(+)}$ exhibits a sudden increase to a peak value followed by a slower decrease, illustrating the transfer to the water body. If the leading wave is still connected to the slide, this transfer would benefit to it, otherwise, it would likely generate a second wave. The plot allows the assessment of the transfer duration and the maximum flux value (e.g., respectively 1 s and 400 ($N.m^{-1}$) for the case $h_s = 2h_0$). The time integration of any of the four components over the generation duration gives the corresponding "impulse" $I$ (impulse of momentum flux or equivalently impulse force) in $N.s.m^{-1}$ or $kg.s^{-1}$. This integrated variable is commonly used in wave impact related studies (Poncet et al., 2022). It is an important variable, for instance controlling the sliding of a breakwater caisson submitted to an extreme wave impact (Lemaire et al., 2018).

In our study, the impulse is calculated by integrating over the first 3 s. This value allows to cover the largest generation duration and for the shorter ones, the impulse decreases quickly after generation and therefore, the remaining time interval, from the end of generation to $t = 3$ s does not really influences the final value.

Figure 4.9 shows the relationship between the horizontal positive impulse $I_{x(+)}$ and the maximum leading wave energy value ($E_{w(max)}$) on one hand, and between the slide initial energy $E_0$ and the resulting $I_{x(+)}$, on the other hand, for different slide volumes. Note that, compared to the generic cases described in table 3.13, here, three additional slide volumes ($h_s = 3h_0$, $h_s = 3.5h_0$, $h_s = 4h_0$) have been added to confirm the trend of the current results. This figure points out a direct linear-like relationship between the logarithmic base 10 of potential slide energy $E_0$ and $I_{x(+)}$ values. On these cases with no submergence and a low viscous fluid (water) for the slide, $I_{x(+)}$ simply linearly increases with $E_0$. A similar relationship exists between $I_{x(+)}$ and the leading wave maximum energy $E_{w(max)}$ occurring during the generation process. Hence, for those particular cases, the horizontal positive impulse $I_{x(+)}$ is obviously a relevant proxy or parameter, to explain or predict the maximum wave

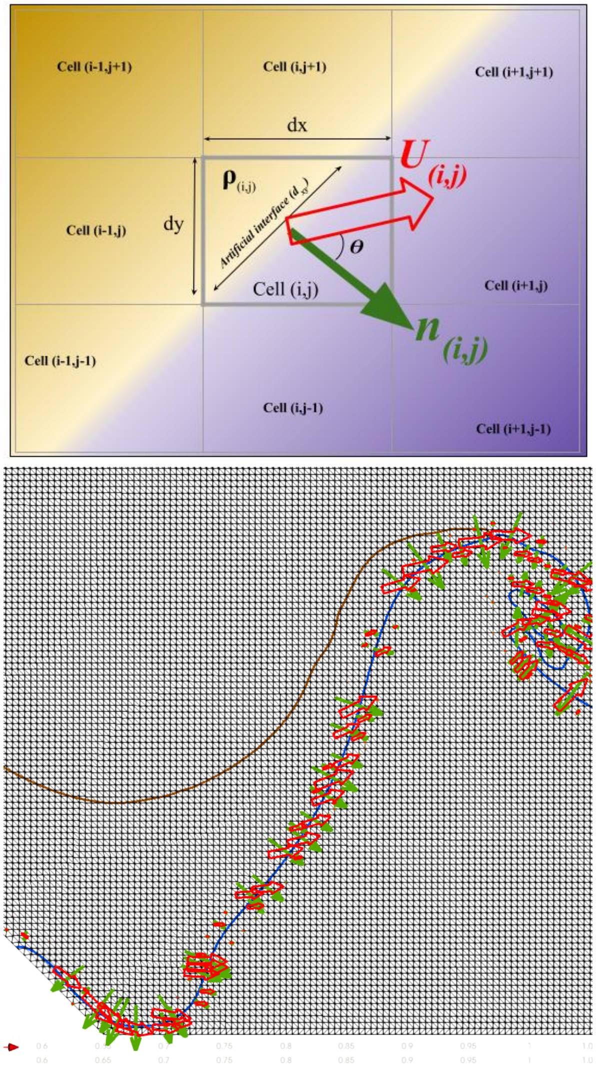

Figure 4.7 – Momentum flux computation at the slide/water interface. Top : Schematic representation of the local variables in the cell. The background color illustrates the gradient of the `alpha.water` field. Bottom: Example of the real distribution of velocities $\vec{\mathbf{U}}$ and normal vectors $\vec{\mathbf{n}}$ along the slide water interface (case $h_s = 2h_0$, $t = 0.4$ s)

generation. We shall see later that the slide rheology makes the interpretation of this parameter more complex.

Finally, to validate the momentum computation, we present, in figure 4.10 a comparison between the horizontal momentum flux and two other estimations of the resulting horizontal force acting on the water body. The first one estimates the variation in time of the water body momentum and the second one is a direct integration of the pressure forces through the slide/water interface. Even though there are some slight differences, between the three curves, which we attribute to numerical inaccuracies, the overall trend is similar.

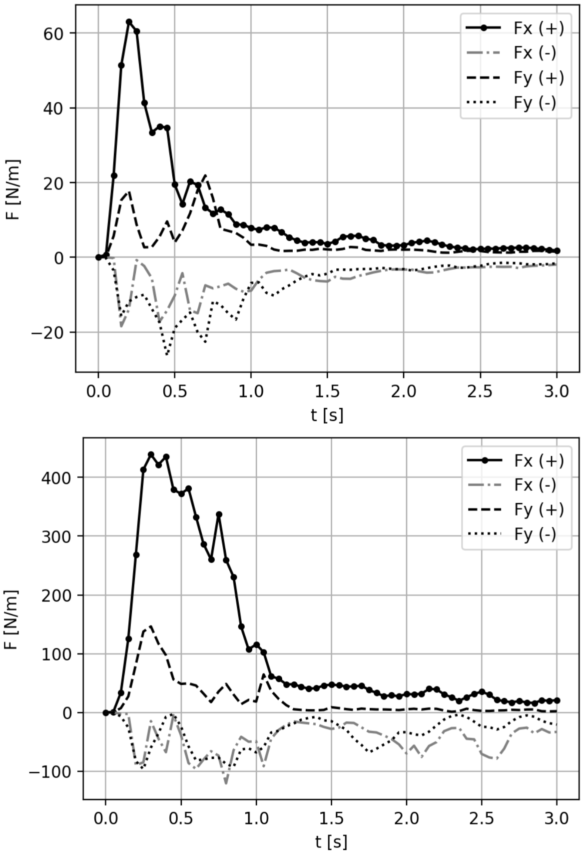

Figure 4.8 – Time evolution of the four components of the momentum flux through the slide water interface for two simulation cases. Left : $h_s = 0.75h_0$. Right : $h_s = 2h_0$.

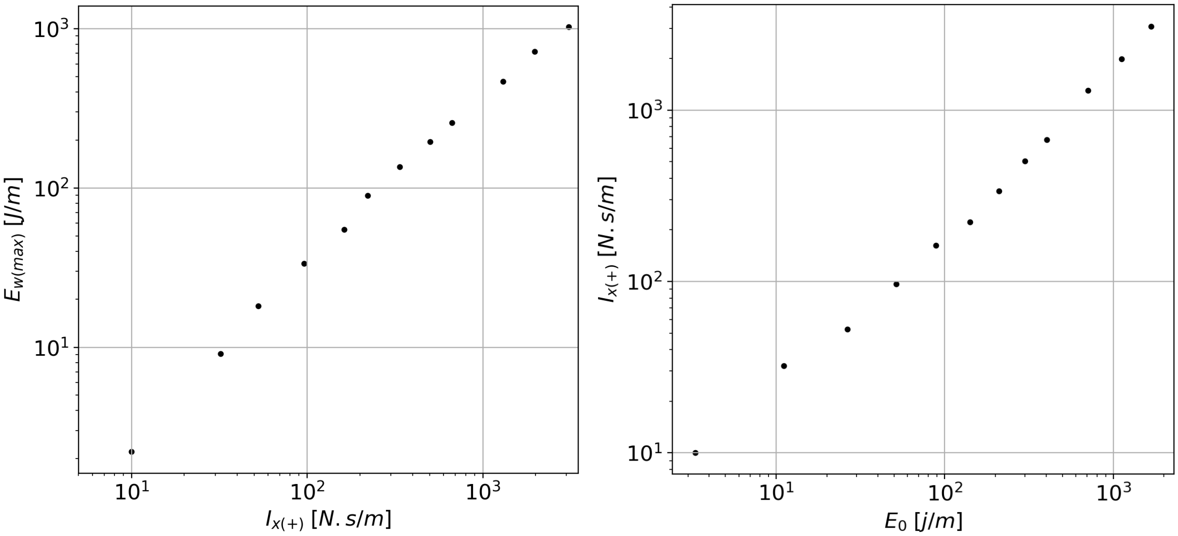

Figure 4.9 – Relationship between the horizontal positive impulse $I_{x(+)}$ and the maximum wave energy $E_{w(max)}$ (left) and the initial energy $E_0$ (right) for subaerial water slide cases with no initial elevation.

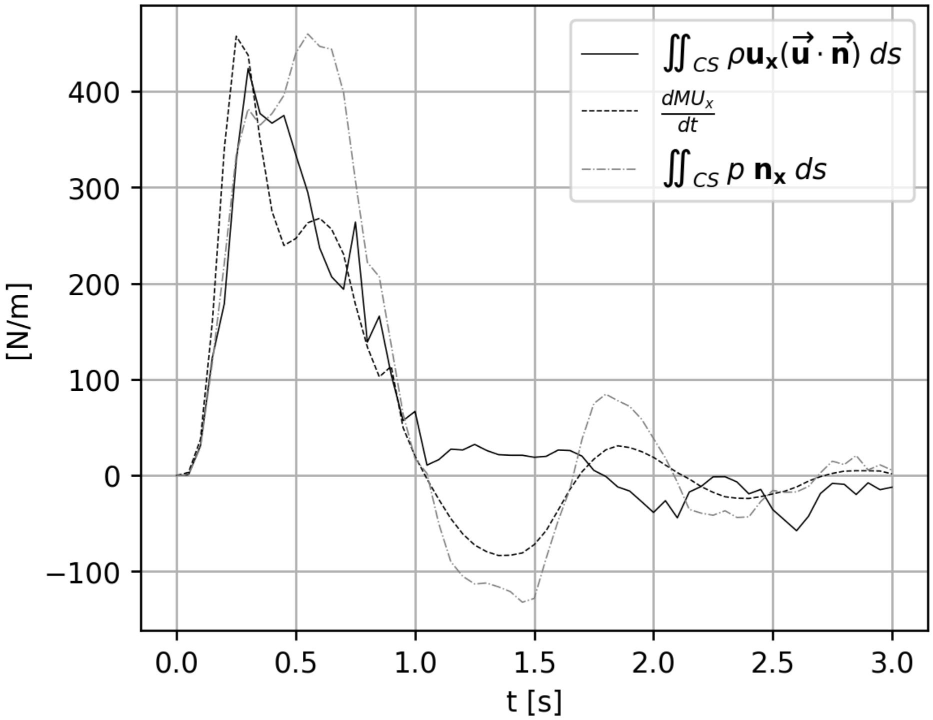

Figure 4.10 – Comparison between the horizontal momentum flux through the slide/water interface, the derivative of the overall water body (see control volume in figure 4.5) of water and a direct integration of the pressure force (p-ρgh field) over the interface (CS) for $h_s = 2h_0$ case.

### 4.1.3 Wave transformation

After the generation, at some point, the leading wave detaches from the slide dynamics to propagate as a free wave. The subsequent evolution of this wave is then entirely determined by its characteristics at this particular time. In this section, we detail the main wave transformation processes : dispersion and breaking.

#### 4.1.3.1 Dispersion

Figure 4.11 shows the time evolution of the water interface at x= 5 m for the slide volumes of table 3.13. As expected, small volume slide cases exhibit the oscillatory-shape profile already described in the literature. For increasing slide volumes, the oscillatory wave train progressively disappears to the profit of a predominant leading wave more and more asymmetrical. Notably, the leading wave non linearity progressively increases to very strong values.

As previously pointed out, after generation, the wave is free and its subsequent evolution depends on its features at this time. Regarding frequency dispersion, the relevant parameters are the relative wavelength $L/h_0$ and the non linearity as measured by the Ursell Number (see section 2.4.2). Figure 4.12 shows these parameters, calculated for the leading wave, in function of the initial slide energy for the cases studied. The relative wavelength ranges from around 5 for the smaller slide volumes to more than 25, for the largest. The usual limit for the shallow water theory (i.e., 20) is given by the red horizontal line in the plot. Note that this limit is valid for monochromatic waves, which is not the case here, therefore, it is only an indicative parameter. Similarly, the estimation of the wavelength is also only indicative, and a more comprehensive investigation should be carried to determine the frequency content of the wave (for instance through a wavelet analysis). Nevertheless, through this qualitative analysis, we can say that the dispersion is expected to be rather limited for the larger volumes, and stronger for the smaller volumes, which is exactly what is observed in Figure 4.11. As indicated just above, for the larger slide volumes, a few trailing waves are nevertheless still present, witnessing a weak dispersion but nevertheless, most of the energy remains in the leading wave.

There is another type of dispersion, called amplitude dispersion, strongly dependent on the non linearity of the wave. The elementary waves with the higher amplitudes propagate faster, resulting in the steepening of the resulting wave. Therefore, in our cases, amplitude dispersion is expected to dominate in the cases involving the larger slide volumes as they generate the most non linear leading waves. It is exactly what is observed in Figure 4.11, with the gradual steepening of the wave for increasing slide volumes.

In summary, in the process studied, the two types of dispersion coexist. Frequency dispersion dominate the cases with the smaller volumes, while amplitude dispersion dominates the larger volume cases.

A wavelet analysis is now conducted in order to give another representation of the dispersion process. The methodology employed is described in section 3.2. The free surface is extracted at different gauge positions in the domain (Figure 4.13). Figure 4.14 shows two examples of the signals obtained for two particular slide volumes. The corresponding wavelet scalograms are presented in Figure 4.15.

In the smaller volume case, in the upstream part of the channel (upper plot), the signal is localized in time and the frequencies are symmetrically distributed over a central frequency of 1 Hz. As the wave train progresses through the channel, a clear separation operates. The wave coming first is a composition of waves of low frequencies centered around 0.5 Hz, in line with the apparent wave period measured in Figure 4.14. Follows a wave train of higher frequencies than 1 Hz but with the most energetic part at this frequency. Therefore, the frequency dispersion literally cut the spectrum in two, the initial lower frequency part composing the final leading wave.

With a larger slide volume ($h_s = 2h_0$), the behavior is different. The frequency content of the initial leading wave is more concentrated on the lower values (around 0.5 Hz). As the wave progresses, this energy seems to spread to even lower values in line with the estimation of the apparent wave period of Figure 4.14. For instance, at the last gauge, significant energy is present at very low frequencies before the main wave reaches the gauge. As in the first case, the frequency dispersion is visible but remains very weak. The initial energy stays bounded to the leading wave. Additionally, a progressive increase of the energy at 1 Hz is observed in the leading wave, reaching very significant values in the last gauge. This is clearly a non linear effect which tends to sharpen the wave and add energy to the crest. This effect is visible in Figure 4.14 with the gradual increase of the leading wave amplitude.

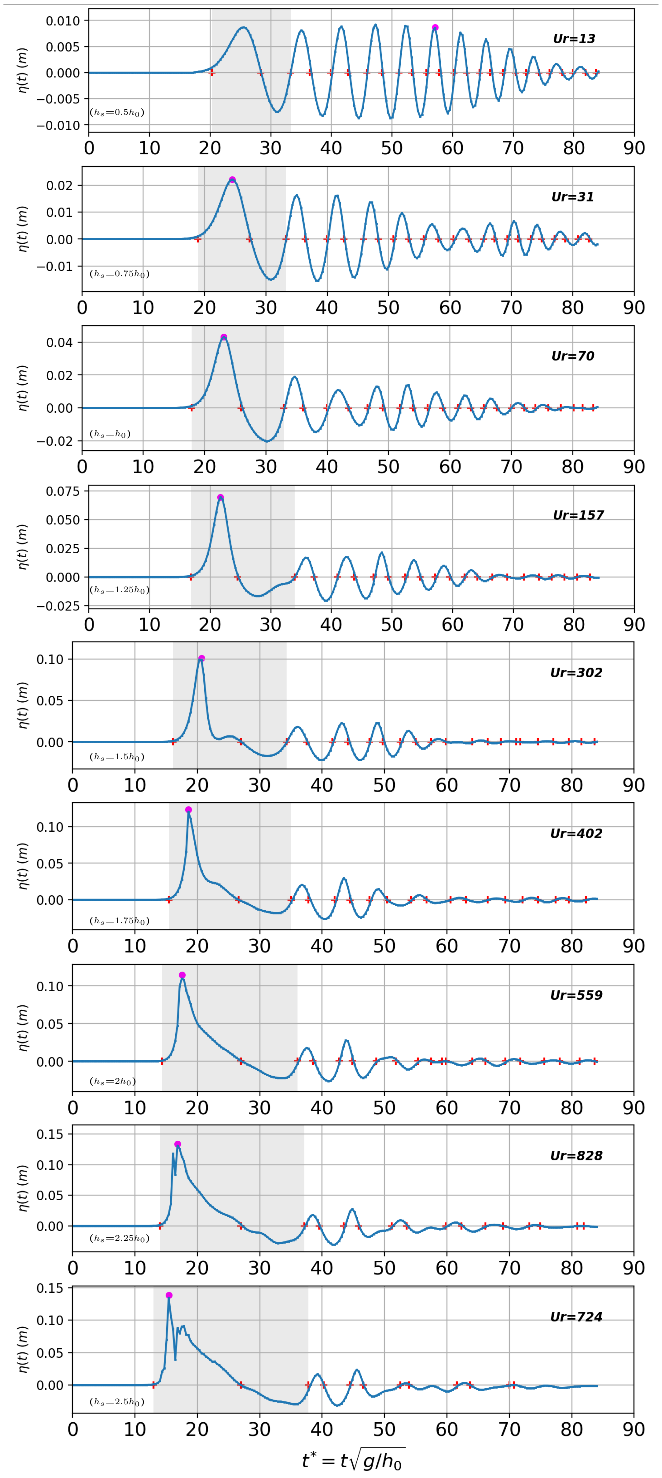

Figure 4.11 – Free surface at $x = 5$m for increasing water slide volumes ($h_s$ from $0.5h_0$ to $2.5h_0$ every $0.25h_0$). The respective times of zero-crossing and maximum wave amplitude are denoted by "+" and "●" markers.

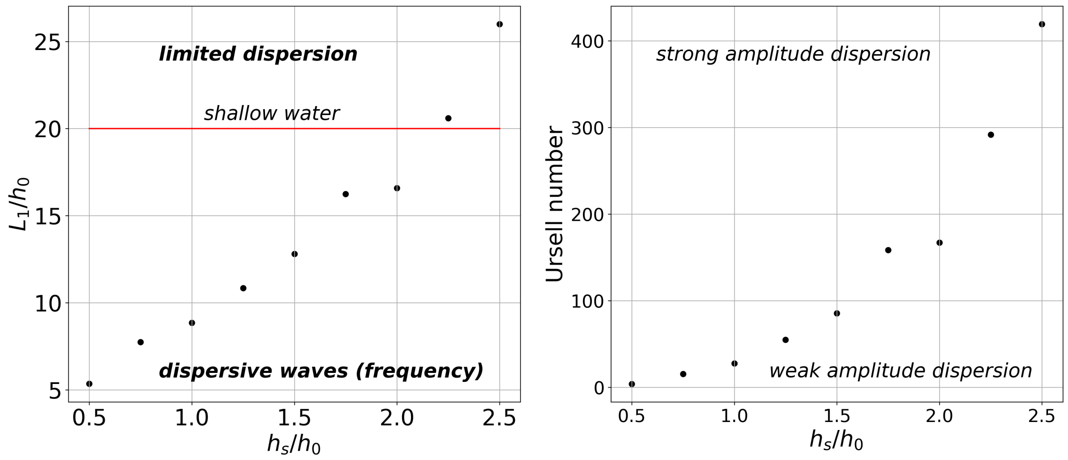

Figure 4.12 – Characteristics of the leading wave just after generation for different initial slide energy. Left : relative wavelength $L_1/h_0$. Right : Ursell number.

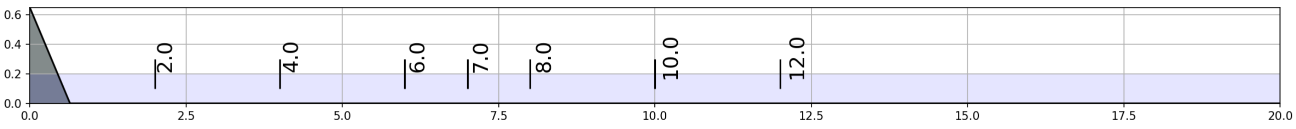

Figure 4.13 – Gauges positions in the domain.

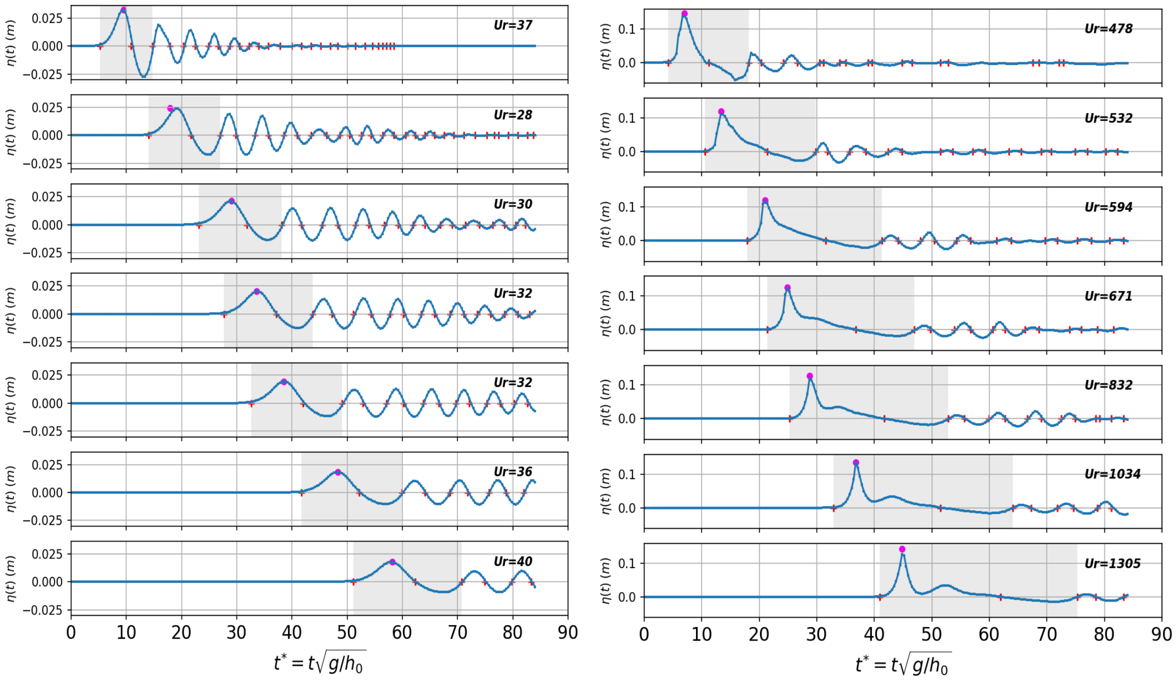

Figure 4.14 – Free surface time series at (from top to bottom) : x= 2m, 4m, 6m, 7m, 8m, 10m, 12m. Left : $h_s = 0.75h_0$, Right : $h_s = 2h_0$ case (right). The leading wave period is depicted by the gray color extent.

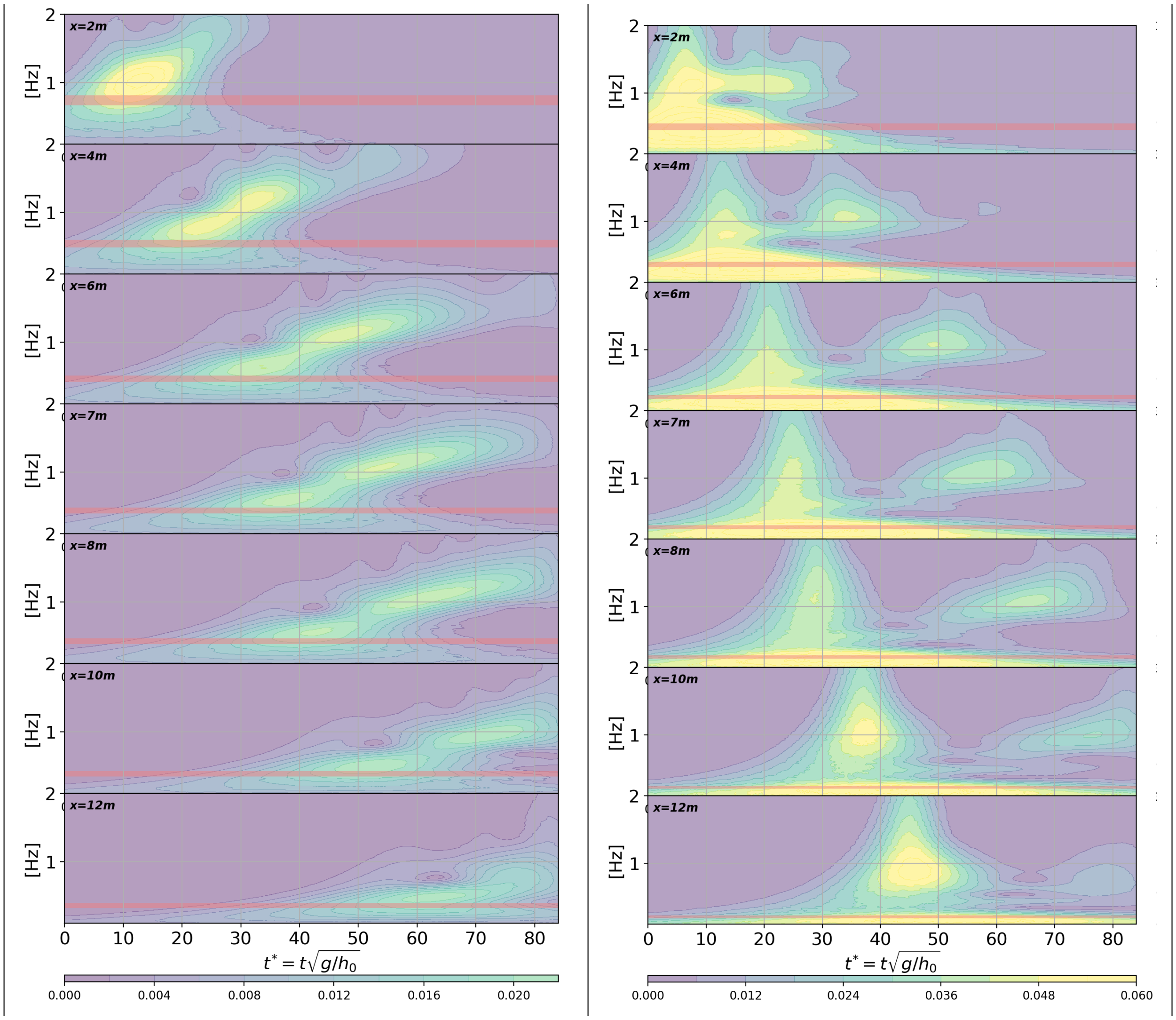

Figure 4.15 – Wavelet scalograms. Left : $h_s = 0.75h_0$, Right : $h_s = 2h_0$. The horizontal pink ribbon indicates the apparent leading wave frequency (± 10 %) corresponding to the grey area in Figure 4.14. The colorbar represents the energy of the signal component at each time/frequency point in $m^2/s$.

#### 4.1.3.2 Wave breaking and energy dissipation

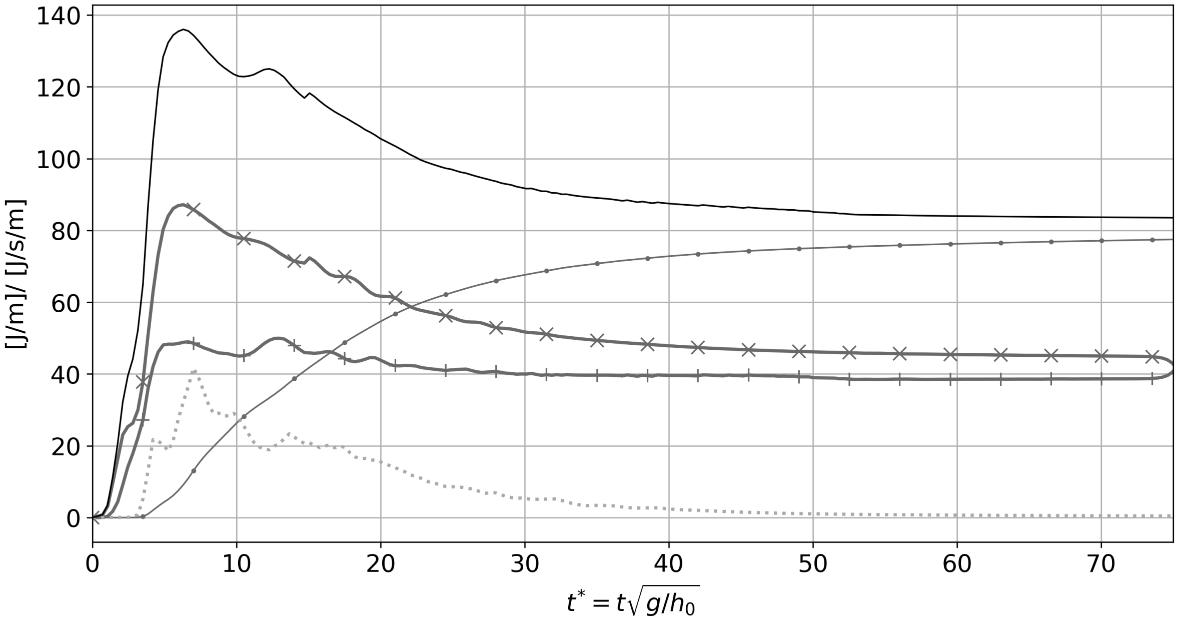

Figure 4.16 – Time evolution of the wave train energy components and dissipation. "×" : $E_k$ $[J/m]$, "+" : $E_p$ $[J/m]$, ● : cumulative dissipation $\int \phi_w \, dt$ $[J/m]$, solid line : wave train total energy $E_k + E_p$ $[J/m]$, dotted line: instantaneous dissipation rate in water $\phi_w)$ $[J/s/m]$. slide case : $h_s = 2h_0$

Figure 4.16 presents the time evolution of the wave train energy and dissipation for a case involving a large slide volume. It is here representative of the leading wave energy evolution as the rest of the waves do not carry much energy and do not undergo strong evolution. Conversely to what is observed for a small volume, here, the leading wave experiences a strong breaking which starts quickly during generation and last until the wave reaches the end of the channel.

The slide motion starts, and, with no submergence, its effect is immediately felt by water, and as a result, the wave energy immediately increases. During this phase, the share between kinetic and potential is not even and most of the slide energy is transformed into wave kinetic energy. At the wave energy peak, the ratio $E_k/E_p$ is around 1.9. As previously mentioned, dissipation by breaking already started before the energy peak time. In this case, the breaking is very violent (Figures 4.1 and 4.2) and the associated dissipation grows very quickly to a peak of about 40 J/s/m at the same time as the energy peak. We know from Figure 4.4 that this time marks the end of the generation. After this, the wave is freed, the breaking process goes on and gradually dissipates mostly the kinetic energy until it reaches a value just slightly superior to the potential energy. At this time the ratio $E_k/E_p$ is around 1.15 and the dissipation rate is almost zero. Interestingly, in this case, the total energy dissipated is almost equal to the final wave train energy.

In Figure 4.17, we give an estimation of the leading wave celerity and compare with other existing theories (see section 2.4.4). During the breaking, the computed wave celerity is larger than any other theories. This is logical as at this time the wave is still under the influence of the slide and both moves at the same celerity. When the dissipation is maximum, the wave is freed. At this time, the celerity matches well with the bore theory (Hughes, 1992). Then the celerity progressively decreases as the wave dissipation vanishes. At this stage, the celerity of the leading wave matches well the solitary wave theories. The shape of the wave is also very similar to the classical solitary wave shape.

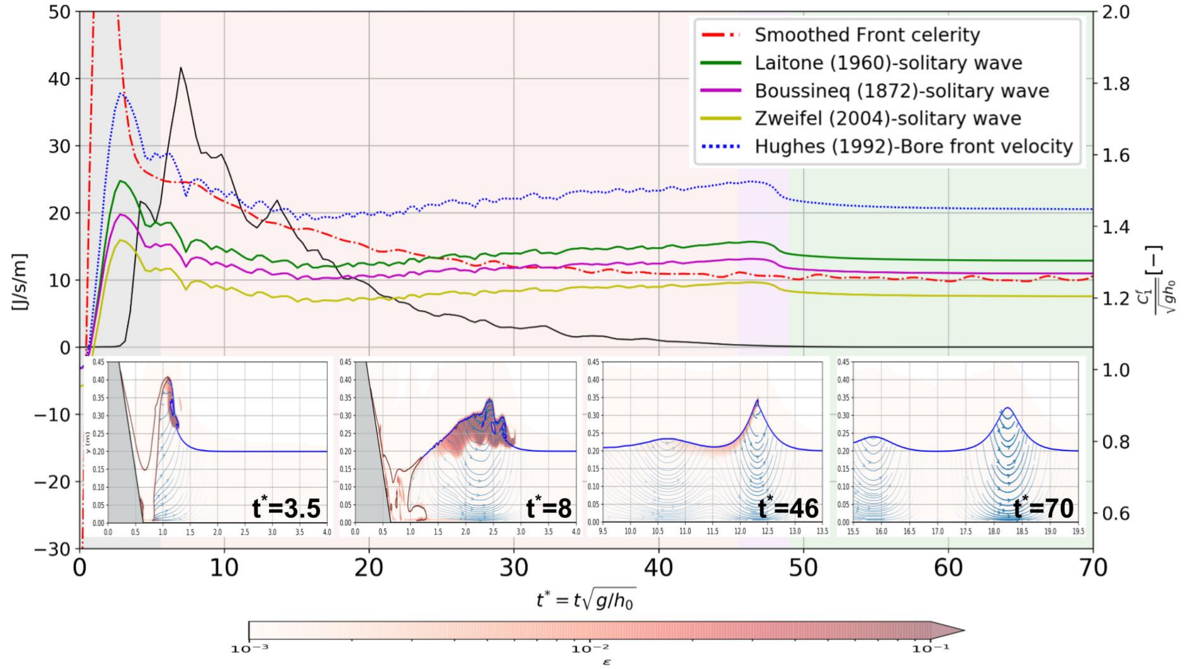

Figure 4.17 – Celerity of the leading wave and comparison with existing theoretical formulas (right y-axis) and leading wave dissipation rate (black solid line - left y-axis). (The wave shape and the dissipation field is also provided in the bottom panels to illustrate the wave regime changes with time). The background color shows the leading wave zone condition at different moments (i.e., generation, transition, weakly breaking, propagation). Slide case : $h_s = 2h_0$

If, in the process of wave generation by subaerial slides, the wave breaking has already been described (Fritz et al., 2004; Bullard et al., 2019), the intrinsic reasons for this breaking were never really investigated. Here, with the help of the model results, it is possible to test the classical breaking criteria (see section 2.4.3) and determine which one explains the best the process observed. Figure 4.18 proposes this investigation for two different slide volumes. The first result is that the breaking of the wave is not due to its steepness, this parameter being, in both cases, much lower than the usual 0.14 breaking threshold. A depth induced breaking would start for a wave amplitude larger than $0.78h_0$. The smaller slide volume case shows that this is not the case, the wave relative amplitude $a_1/h_0$ always being lower 0.4. In the larger slide volume, the situation is less clear as this parameter is larger than one at the time of breaking ($t^*$ around 3.5). $U_{max}/C_1^f$ is usually a parameter able to detect the breaking whatever the depth. Here again, the smaller volume case shows that the usual threshold for this parameter (0.85 (Saket et al., 2017)) is not reached during breaking. This is certainly due to the fact that at this time the wave is not free and the celerity is controlled by the slide motion. Finally, in our case, the ratio of the kinetic to the potential wave energy is what explains the best the breaking. At the beginning $E_p$ is negligible, leading to the very high values of the ratio at the very beginning of the process. When the breaking starts, in both cases, the ratio is around 2, which expresses a strong internal energetic disequilibrium. The wave can not withstand this state and the energy is immediately dissipated in order to reach a better equilibrium.
The situation becomes different as soon as the wave is free and the usual breaking criteria should, at this time, again hold. In the smaller volume case, the breaking is very short. Conversely, in the larger slide volume case, the breaking continues at least until $t^* = 50$ while the generation ceased for $t^* = 6$. Between those two instants, the ratio $a_1/h_0$ vary between the inception of breaking value (0.78) and the 0.6 limit stressed in Bullard et al. (2019), the latter being the value reached in the propagation zone.

Interestingly, the transition to this asymptotic value takes place exactly at the boundary between the weakly breaking and propagation zones. $U_{max}/C_1^f$ also shows a strong decrease in this area. Hence, 0.6 should be the asymptotic ratio reached by the wave amplitude after gradual dissipation due to depth induced breaking.

In summary, in the process studied, the breaking can not be predicted by usual wave breaking criteria simply because the "wave" is not really a wave as long as it is being generated by the slide. During this time, the kinetic to potential energy ratio explains the best the breaking inception. As soon as the wave is freed, the usual breaking criteria should again correctly predict the subsequent evolution regarding breaking.

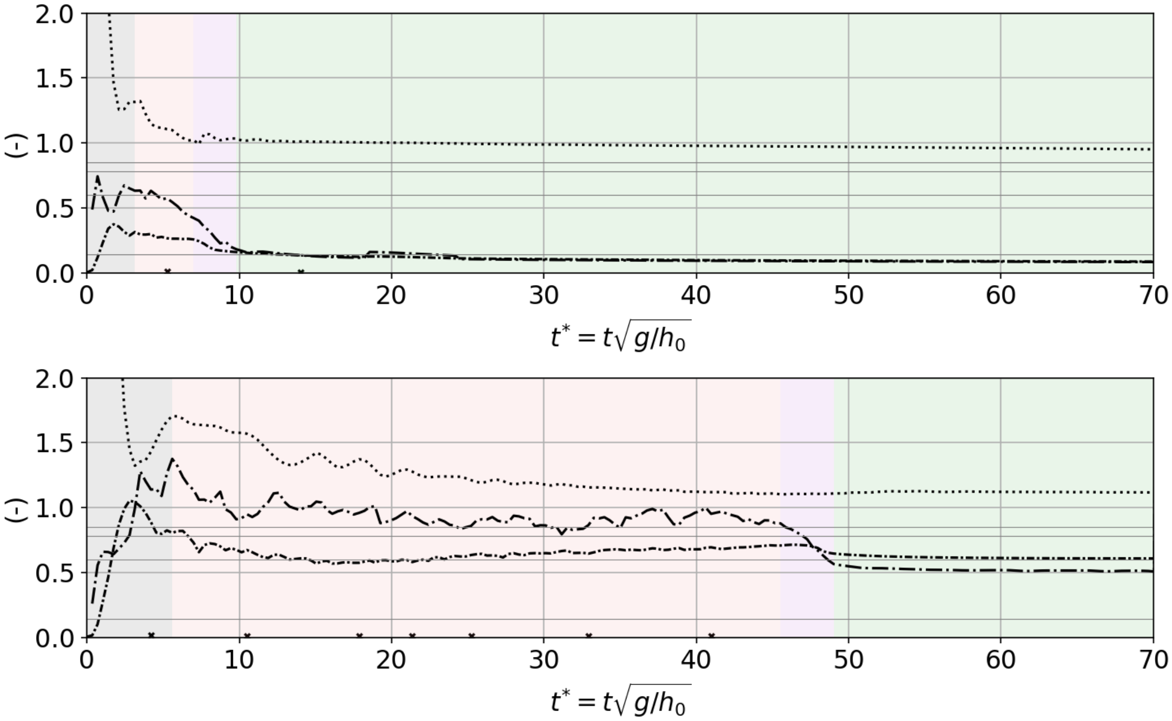

Figure 4.18 – Time evolution of wave breaking related non-dimensionalized parameters and comparison with classical breaking criteria. $a_1/h_0$ (dense dash-dotted line), $a_1/L_1$ (black "×" marks), $E_k/E_p$ (dotted line) and $U_{max}/C_1^f$ (dash-dotted line). Grey horizontal lines stand for classical breaking criteria values : 0.14, 0.6, 0.78, and 0.85. The background color shows the leading wave zone condition at different moments (i.e., generation, transition, weakly breaking, propagation). Slide cases: $h_s = 0.75h_0$ (top) and $h_s = 2h_0$ (bottom)

### 4.1.4 Efficiency of the energetic process

In this section, we consider wave generated by subaerial landslide as an energetic process and investigate its efficiency.

Most of the previous studies related to the same topic, focused on the wave amplitude. Here, we rather considered the wave energy as a more relevant hazard indicator. The relationship between wave energy and amplitude is presented Figure 4.19 for two characteristic times (i.e., just after generation and at the end of the domain). The inter-comparison of the two curves illustrates first the loss of energy during the wave transformation phase (including dispersion and wave breaking). This loss is significant and

reinforce the idea that the maximum wave energy or wave amplitude is not a relevant indicator of the hazard, except if the stake is located in the generation zone. The share of kinetic and potential energy in the total wave energy is as expected very different before and after wave transformation. At the end of the domain there is almost an even share between the two, which also explains the concordance with the linear wave theory. For the larger slide cases, though, the strong non linearity of the leading wave should explain the slight discrepancy with this theory.
The relationship between the wave amplitude and the wave energy is also presented in this plot. The linear wave theory stipulates $E = \frac{1}{8}\rho g {H_1}^2 = \frac{1}{2}\rho g {a_1}^2$, with $H$ and $a$ respectively wave height and amplitude. For fresh water, this gives a coefficient of 4905 for the square term. The fitting to the simulation results gives slightly higher coefficients, but globally, if the amplitude is known, the energy can be calculated and vice-versa. Therefore, there is no really added value to work with the wave energy except if energy transfers are the focus of the study which is the case here.

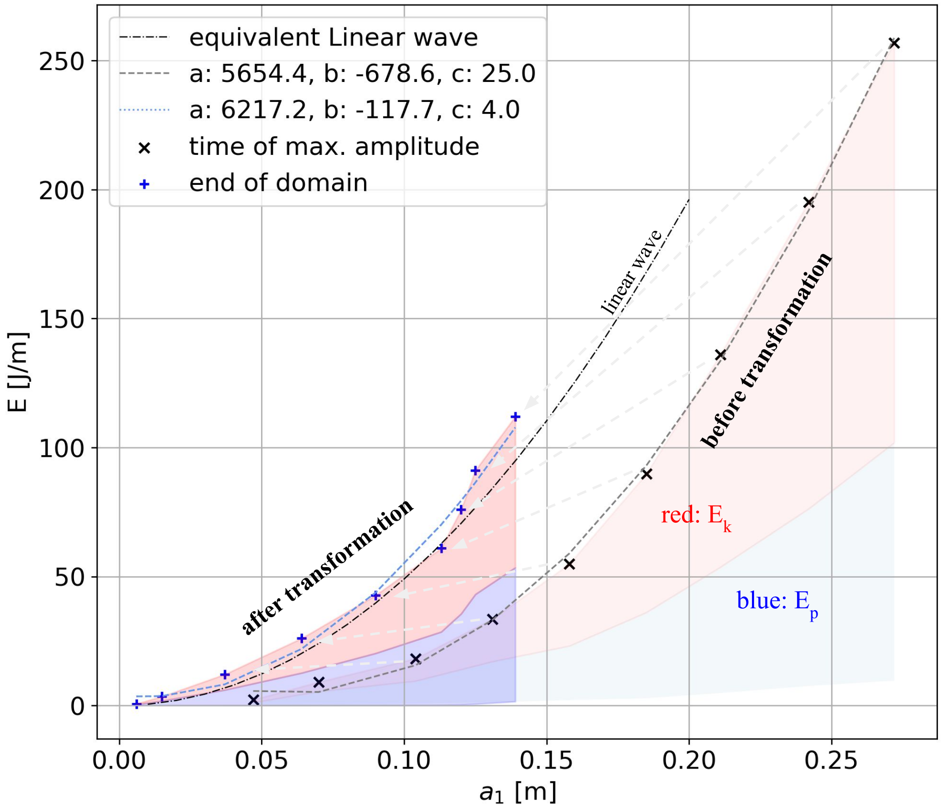

Figure 4.19 – Leading wave total energy after generation ("before transformation" : "×") and at the end of the domain ("after transformation" : "+") versus the leading wave amplitude. The black dash-dotted line represents the energy of a linear wave with an equivalent wave height at t=10s. Colored sections indicate the respective fraction of $E_k$ (red) and $E_p$ (blue) in the total wave energy. The dashed lines are curves fitted on the simulation results leading to maximum energy : $5654x^2 - 678x + 25$ and wave energy at the end of the domain : $6217x^2 - 118x + 4$, respectively.

We now ask the question of the efficiency of the global process transforming the slide energy to the final wave energy including all the wave transformation mechanisms. Figure 4.20 shows interesting information to that respect. First, on the left plot, we can see that the absolute wave energy at the end of the domain increases with the initial slide energy. It means that we expect larger wave energy with larger slide energy, even if all the processes of wave transformation are taken into account especially

including wave breaking. It is probable that this curve would not grow to infinity by increasing slide energy further. There should be a limit in this process that the water reservoir can not withstand. Nevertheless this limit is not reached in our simulations.
On the center plot, the energy lost during wave transformation is plotted against the slide initial energy. Here we distinguished the contribution of the wave breaking and the dispersion. For the latter, this is not really a dissipation per say, but more a fraction of the energy which is transferred from the leading wave to the trailing waves. This energy loss is here evaluated by the difference between the global wave train energy and the leading wave energy. This plot shows for small slide volumes, the leading wave energy is mainly lost due to the dispersion process even though is also occurring. With slide volume increasing, the wave breaking process is more and more predominant compared to dispersion. There is an interesting value of the slide energy around about 2/3 where the energy lost by breaking amounts exactly the one lost by dispersion.
On the right plot, by dividing the leading wave energy by the initial slide energy, we calculate the efficiency of the global energetic process transforming the slide energy to a final leading wave energy. This process shows an optimum for a slide energy around 2/3 corresponding to the case $h_s = 1.25h_0$. For his particular case, the efficiency reaches the maximum value of 50%. For larger slide volumes, the efficiency rapidly decreases to values around 0.3. For small volumes, the efficiency of the process is strongly reduced due to dispersion.

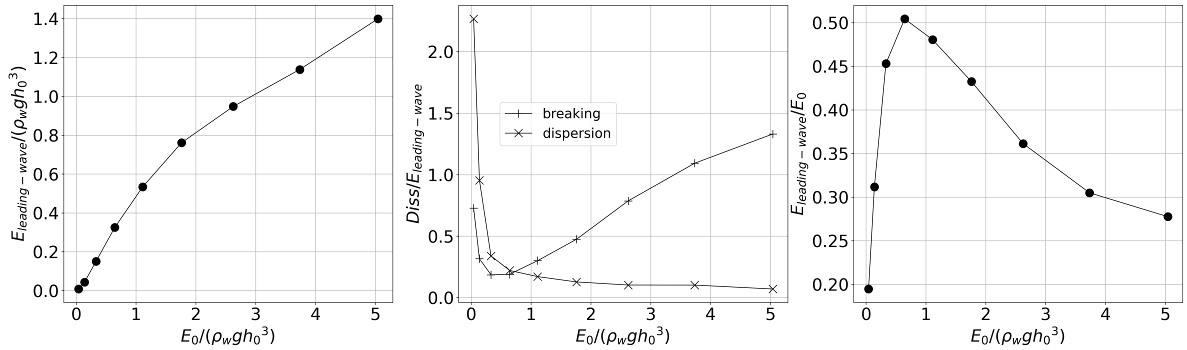

Figure 4.20 – Left : Leading wave energy at the end of the domain (t=10s) versus slide initial energy. Center : Leading wave energy loss respectively due to breaking and dispersion, Right : Efficiency of the energy process from slide energy to final wave energy.

Figure 4.21 summarizes all the previous simulations in the form of three energy curves. This plot illustrates the role of dispersion and breaking for each slide energy case (or equivalently slide volume). This plot type is used recurrently in next sections to allow comparison between the different situations.

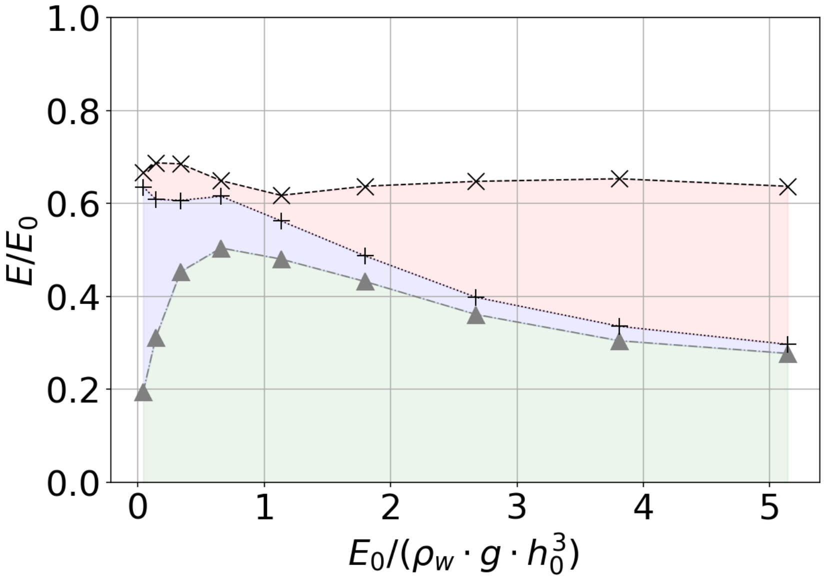

Figure 4.21 – Relative wave energy values for different initial slide energy. × : maximum wave energy $E_{w,max}/E_0$, '+' : final wave train energy $E_{w,t=10s}/E_0$ and triangular markers : final leading wave energy $E_{leading-wave,t=10s}/E_0$. Red : energy dissipated by breaking, purple : energy lost in dispersion, green : final remaining wave energy ($t = 10s$).

## 4.2 Influence of the slide rheology

This section proposes a systematic investigation of the wave sensitivity to several slide rheological parameters, keeping the slide volume and density constant. The methodology follows a progressive approach in which the sensitivity to a specific parameter is assessed by varying its value and observe the changes in the wave generated. To restrain the study in reasonable bounds, the focus is on the generation processes, and therefore, the transformation wave processes such as dispersion and breaking are not investigated further, conversely to the previous part. Once a parameters has been studied, we shift to the next parameter, maintaining the previous parameter to a specific value. This structured approach facilitates a comparative analysis between the results.

### 4.2.1 Phase II: Newtonian slide

We start this study with the influence of the viscosity of a simple Newtonian slide ($h_s = 2h_0$) on the wave generated. The set-up is given in section 3.4.2.2. The slide Reynolds number is calculated as follows $Re = \frac{\sqrt{g\,h_s} \cdot h_s}{\nu_s}$. The highest value corresponds to a water slide, the lowest value ($Re = 10$) to a very viscous slide. In between, the Reynolds number is varied following a logarithmic law.

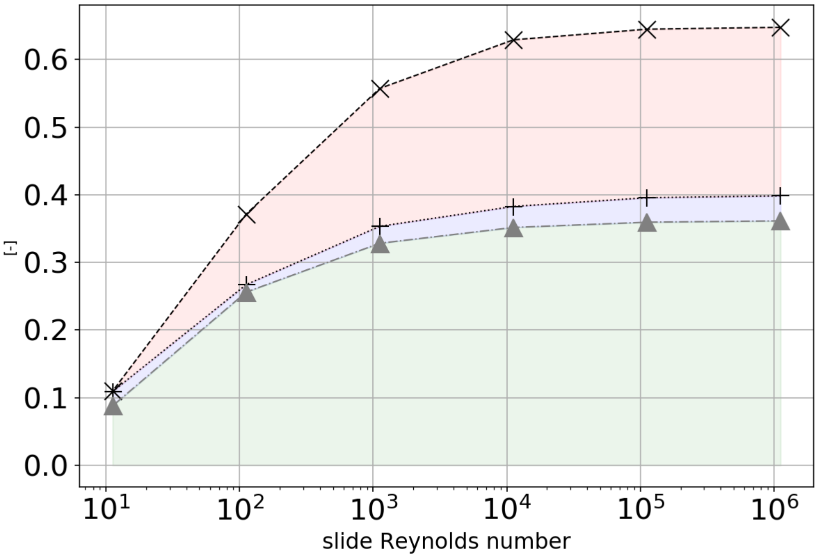

Figure 4.22 – Relative wave energies for different values of the slide Reynolds number for Newtonian slide with $h_s = 2h_0$. Apart from the x-axis, the notation is the same as in Figure 4.21.

Figure 4.22 presents the variation of different wave energies with the slide Reynolds number. The difference between the final wave train energy and the final leading wave energy is used to assess the amount of energy lost by dispersion. Several conclusions can be drawn from this plot.
The influence of the slide Reynolds number is overall weak as long as long as it is larger than $10^3$. For lower values, a drastic decrease of the energy transmitted to the wave is observed. For the most viscous case, the efficiency of the process is only 10% globally (i.e., after generation or at the end of the domain) whereas, for $Re > 10^3$, the generation process has an efficiency of more than 50% and the global process, from the slide energy to the final wave energy, above 30%.
Interestingly, for this particular slide volume, the difference between the wave energy just after generation, and the final wave energy is mainly due to the breaking induced dissipation. Indeed, the

dispersion effect (in purple), stays very limited for all the cases except the most viscous. It means that the behavior of wave after generation is mostly dictated by the slide volume rather than the viscosity. For all those cases, most of the energy is concentrated in the leading wave, whatever the viscosity. It must be noted, nevertheless, that in the most viscous case, the wave is so low that it is not breaking and dispersion is predominant.

Figure 4.23 shows in more details the process of wave generation for different slide viscosities. We can deduce by observing the position of the slide front in a same column of this figure, that the slide motion becomes much slower when the Reynolds number decreases. The slide/water interface is also much more developed for the larger Reynolds. Slide/water interface length and velocity are directly linked to the magnitude of the wave. The subsequent breaking, and therefore the dissipation, is finally dependent on the magnitude of the initial wave as illustrated in the right column of figure 4.23. The result is the curves of Figure 4.22.

### 4.2.2 Phase III: Non-Newtonian slide

In this section, the slide rheology follows the so-called Herschel-Bulkley law (details in section 3.4.2.3). The influence of the yield stress thresholds ($\tau_0$) is first investigated for a Bingham fluid (i.e., $n = 1$). In the Herschel- Bulkley law, the parameter $k$ is homogeneous to a viscosity. Here, this parameter is $10^4$ times the water viscosity which corresponds to the case $Re = 10^2$ in Figure 4.22. It is a case for which the viscosity influence is significant. The yield stress thresholds $\tau_0$ ranges from 0 to 200 [Pa], (0 to 0.05 in non dimensional form). Note that the model shows instabilities for values larger than the limit of this interval.

Figure 4.24 shows the variation of the relative wave energies with the yield stress. The situation with no yield stress corresponds to the case $Re = 10^2$ of the figures 4.22 and 4.23. Between 0 and 0.03, the progressive increase of the yield stress makes the wave energy after generation significantly decrease. Comparatively, the leading wave energy at the end of the channel is relatively stable. It means that the yield stress does not really change the final leading wave energy but rather the amount of the dissipated breaking wave energy. We also note that for these cases, the dispersion is relatively low as most of cases involving this slide volume ($h_s = 2h_0$). Between 0.03 and 0.04, there is a sudden decrease in the final leading wave energy. It corresponds to cases for which the wave after generation is not too unstable and the dissipation by breaking relatively low. For even larger yield stress, the decrease continues but the slope of the curve is comparatively lower (in absolute value). Hence, this figure seems to show that, while the dissipation is important, the final wave energy is not too much affected, but for the cases with no breaking, the wave has no means to adapt, and the decrease of the final leading wave energy is significant. A similar conclusions can be drawn from figure 4.22 but maybe to a lesser extent.

Figure 4.25 shows the distribution of the local viscosity in the slide for the cases located before (top panel) and after (middle panel) the drop of the energy curve observed in Figure 4.24. Note that the case with no threshold would correspond to the case $Re = 10^2$ of figure 4.23. In this case, the viscosity is constant, and equal to $10^4$ the water viscosity which gives a kinematic viscosity of 0.01 $m^2/s$. In figure 4.25, this value corresponds to the dark blue color. Due to the yield stress, the simulations of the Figure 4.25 shows a spatial variation of the viscosity. In particular, we observe a significant increase of this property close to the slide/water interface during the generation ($t = 0.5s$). Due to that, compared to the constant viscosity case, the interface has less ability to deform, and a fraction of the wave is entrained to the left in a back breaking motion. This particularity is not observed in the constant viscosity case on Figure 4.23 second row, even though a backward wave is observed in the slide phase. This difference in the slide interface deformability as well as a likely less important global slide velocity, both may explain the less energetic wave produced with the yield stress. Note that the difference between the two cases (top and middle) of figure 4.25 is not very obvious.

The last parameter investigated is the flow index $n$. In figure 4.24, bottom panel, we observe that the decrease of this parameter (i;e., from 1 to 0.2) slightly increases both the wave energy after generation

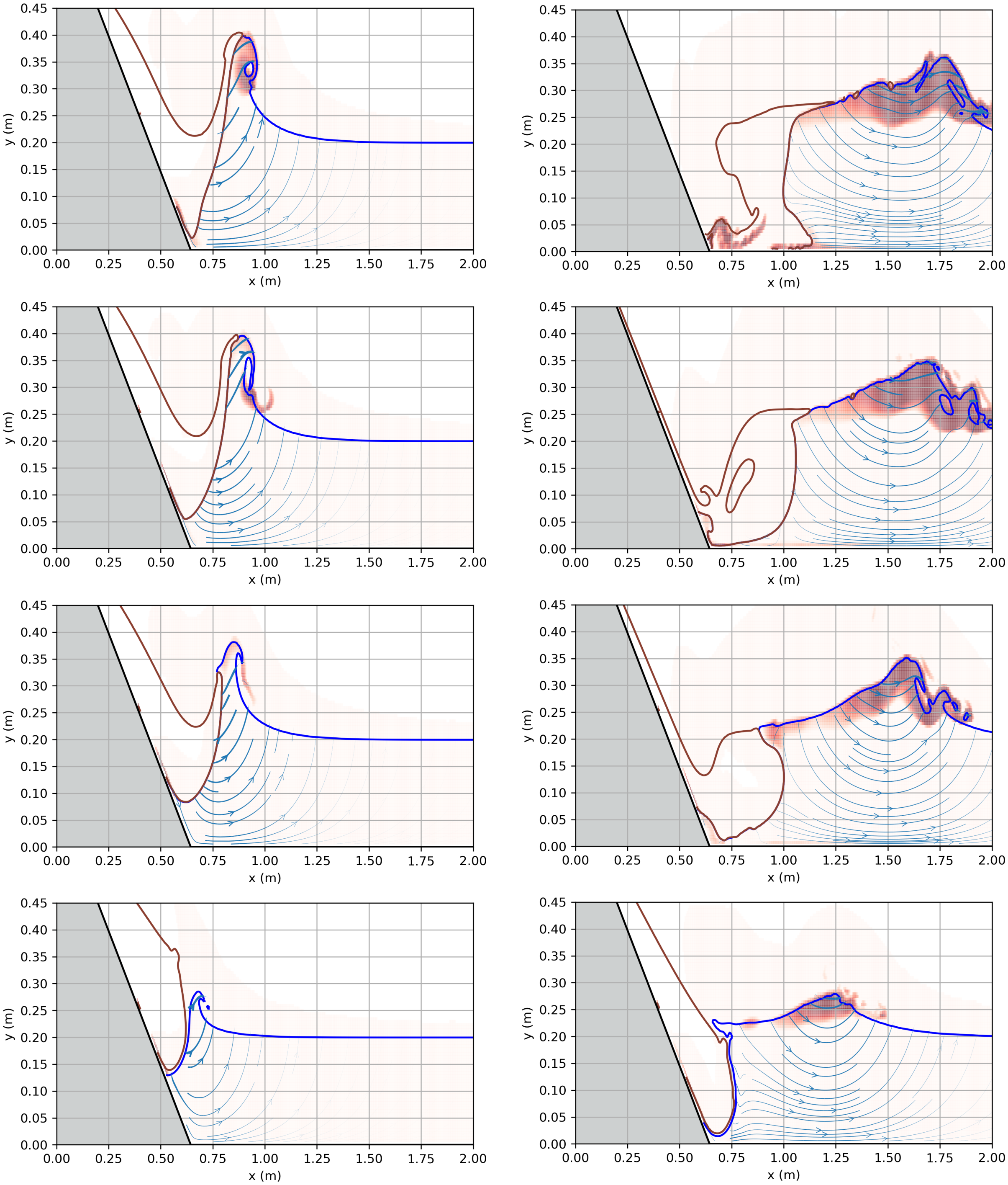

Figure 4.23 – Snapshots of fluid interfaces, streamlines and turbulent dissipation rate $\epsilon$ (surface field), at t=0.35 s (left) and t=0.8 s (right) for a Newtonian viscous slide with $h_s = 2h_0$ and $h_l = 0$. Slide Reynolds numbers from top to bottom cases are: $Re = 10^5$, $Re = 10^3$, $Re = 10^2$, $Re = 10$. The color legend is similar to Fig. 4.2.

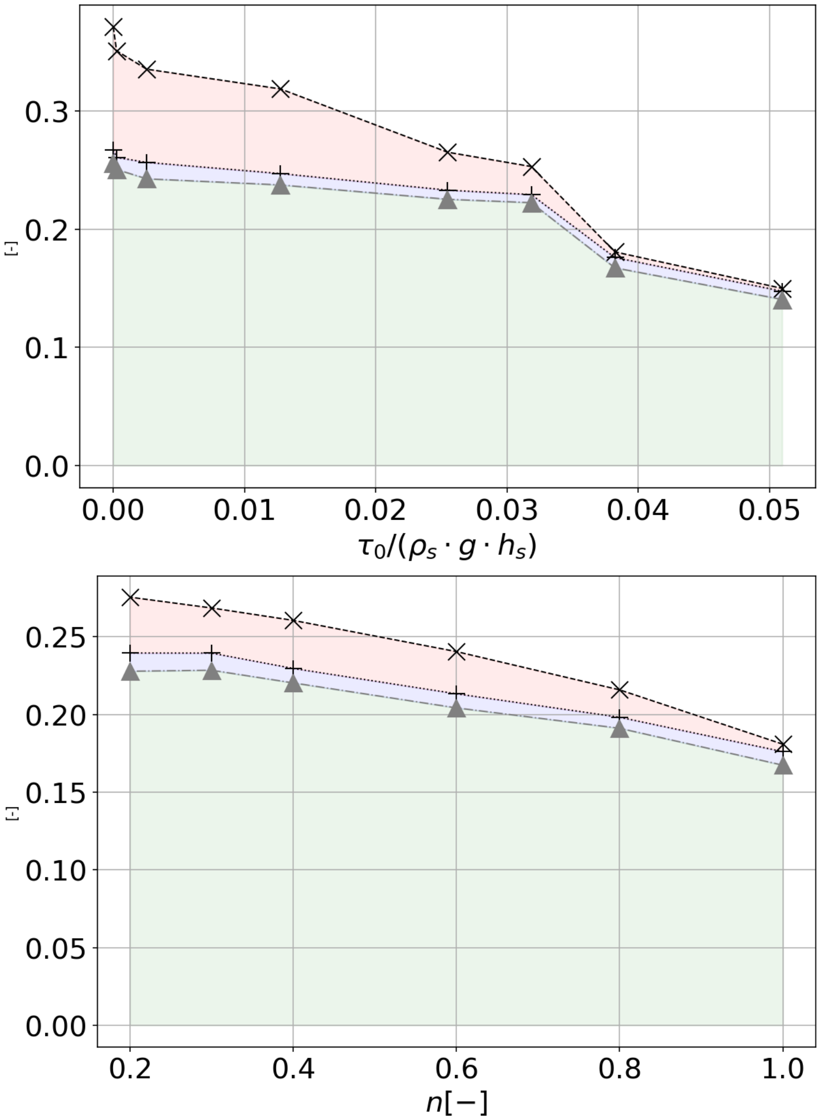

Figure 4.24 – Relative wave energies for different values of : yield stress $\tau_0/(\rho_s \cdot g \cdot h_s)$ for a Bingham fluid $n = 1$ (top panel) and $n$ parameter with $\tau_0/(\rho_s \cdot g \cdot h_s) = 0.0385$ (bottom panel). Herschel-Bulkley Non Newtonian slide with $k$ being $10^4$ times the water viscosity. Slide case : $h_s = 2h_0$ with no initial elevation. Apart from the x-axis, the notation is the same as in Figure 4.21.

and the final wave energy. The reasons stands in the mathematical form of the Herschel-Bulkley law. With lower $n$, the slide is more mobile and more deformable. This is obvious when comparing the bottom and middle panels of figure 4.25. In the case with n=0.3 (bottom panel) the slide is thinner over the slope, witnessing the higher deformability, and the slide/water interface is more developed which finally induces a more efficient horizontal thrust onto the wave. Note that the backbreaking of the wave is also prevented in this case.

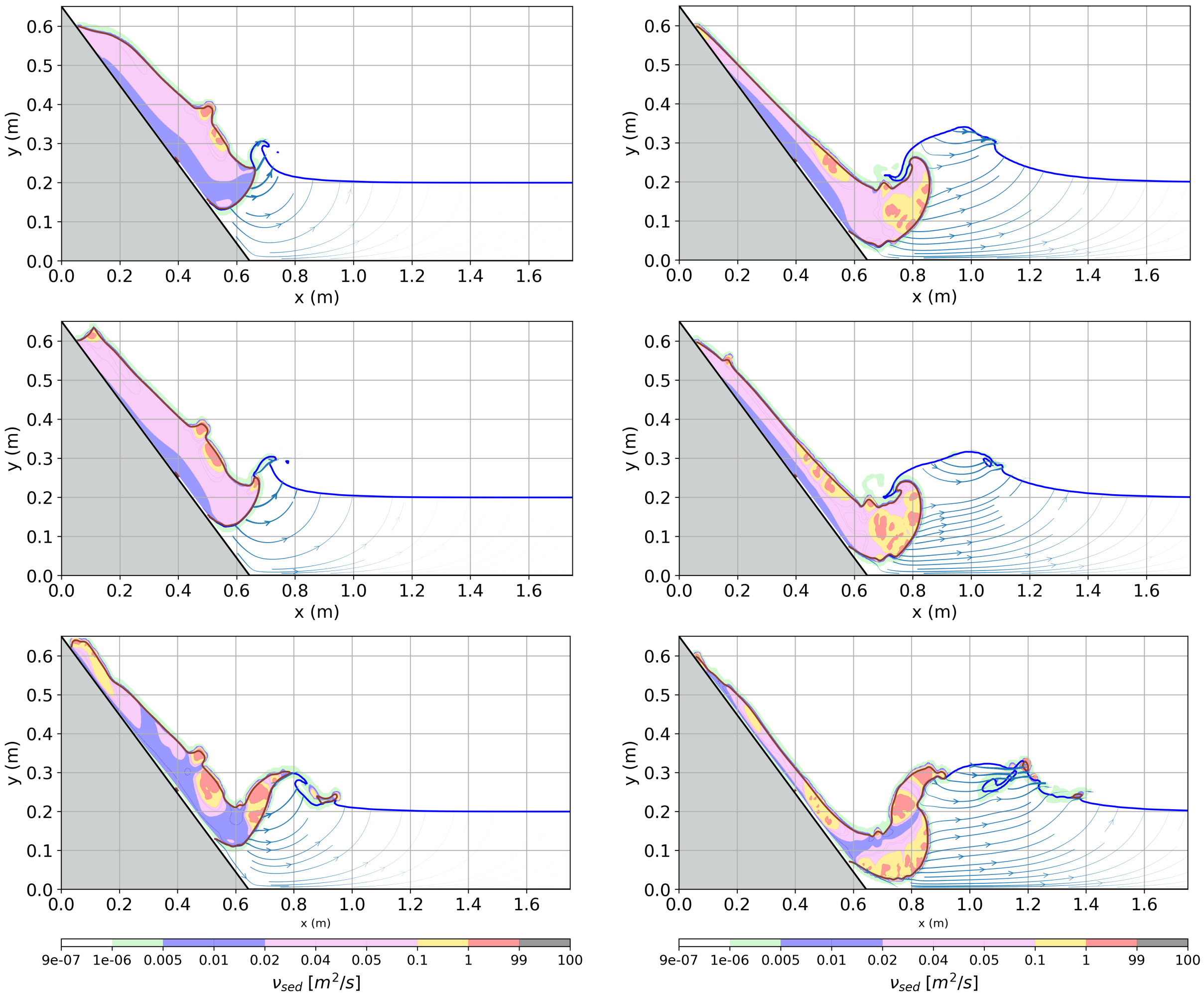

Figure 4.25 – Snapshots of fluid interfaces, streamlines and local slide viscosity (Herschel-Bulkley law) at $t = 0.25s$ (left) and $t = 0.5s$ (right). Top : $n = 1$ and $\tau_0/\rho_s g h_s = 0.031$, middle : $n = 1$ and $\tau_0/\rho_s g h_s = 0.038$, bottom : $n = 0.3$ and $\tau_0/\rho_s g h_s = 0.038$.

### 4.2.3 Phase IV: Slide with initial elevation

So far, all the slides considered in the previous simulations were initially in contact (.i.e, the lowest point of the slide) with the water line. In this section, we now investigate the effect of a slide submergence (i.e., $h_l > 0$) on the wave generation process. The setup studied is detailed in Section 3.4.2.4. As indicated previously, in this section, the slide follows the Herschel-Bulkley model with parameters corresponding to a real clay-water mixture as documented in Huang and García (1998).

Two examples of wave generation with two different slide submergences and volumes are presented in figures 4.26 and 4.27. While the slide characteristics are different, the processes of wave generation share common features.

In both cases, the slide deforms and accelerates before reaching the water line. At the water line, the slide is very thin and its velocity is strong. As a result, the penetration depth into water is much larger than in the case with no initial elevated slide. The slide is so fast that is moves on the water interface as it deforms, creating a cavity and finally a back breaking motion on the slope (or on the bottom for the most energetic case). Vortices and turbulence are generated in this area resulting in strong dissipation. A wave is nevertheless generated, propagating to the right, with or without breaking, depending on the case.

This wave generation pattern is consistent with the observations reported in Bullard et al. (2019) and Rauter et al. (2021).

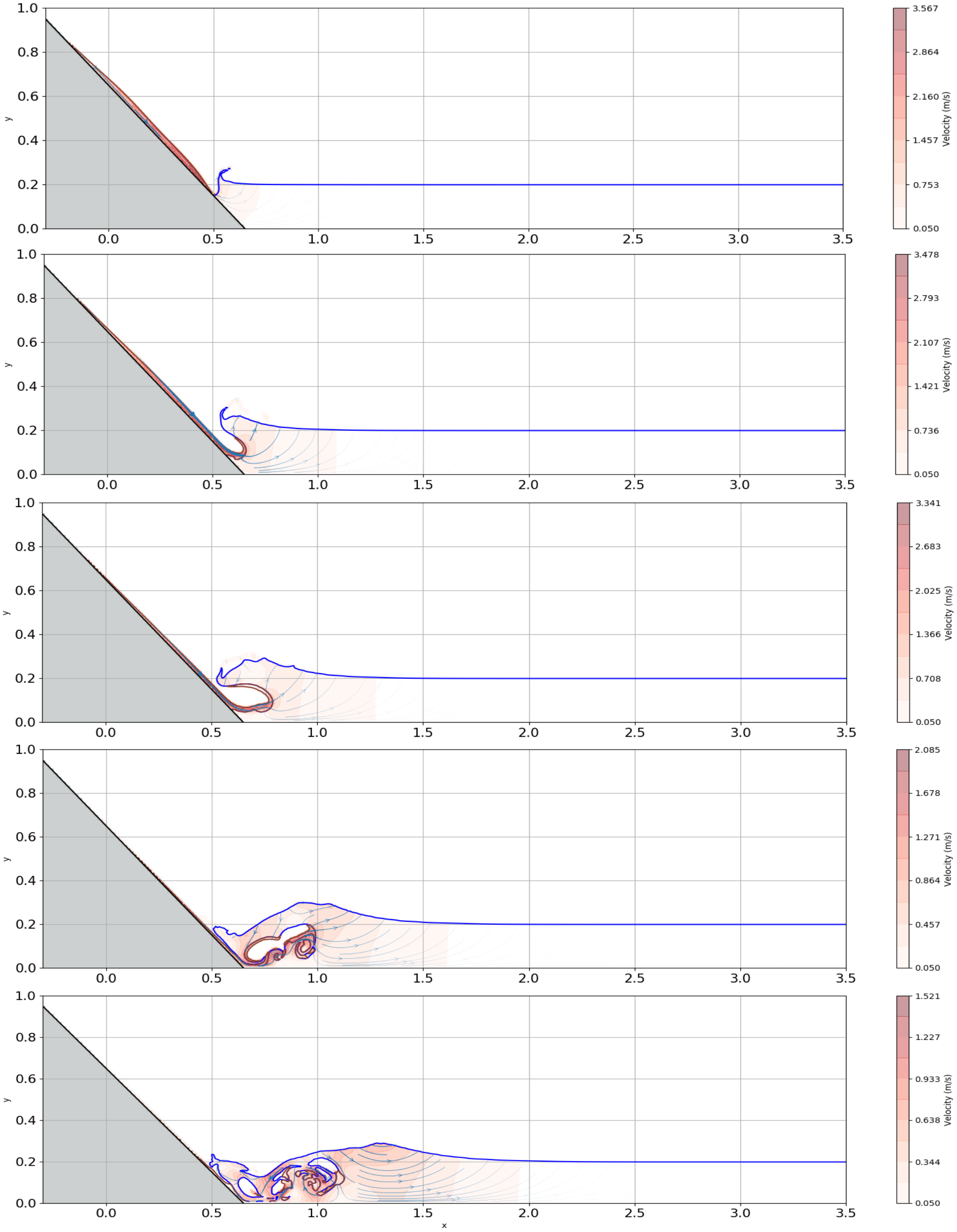

Figure 4.26 – Fluid interfaces, streamlines and velocity magnitude (surface field) at different times (top to bottom: t= 0.4s, 0.5s, 0.6s, 0.8s, 1s) for a slide case with $h_s = h_0$ and $h_l = 2.5h_0$.

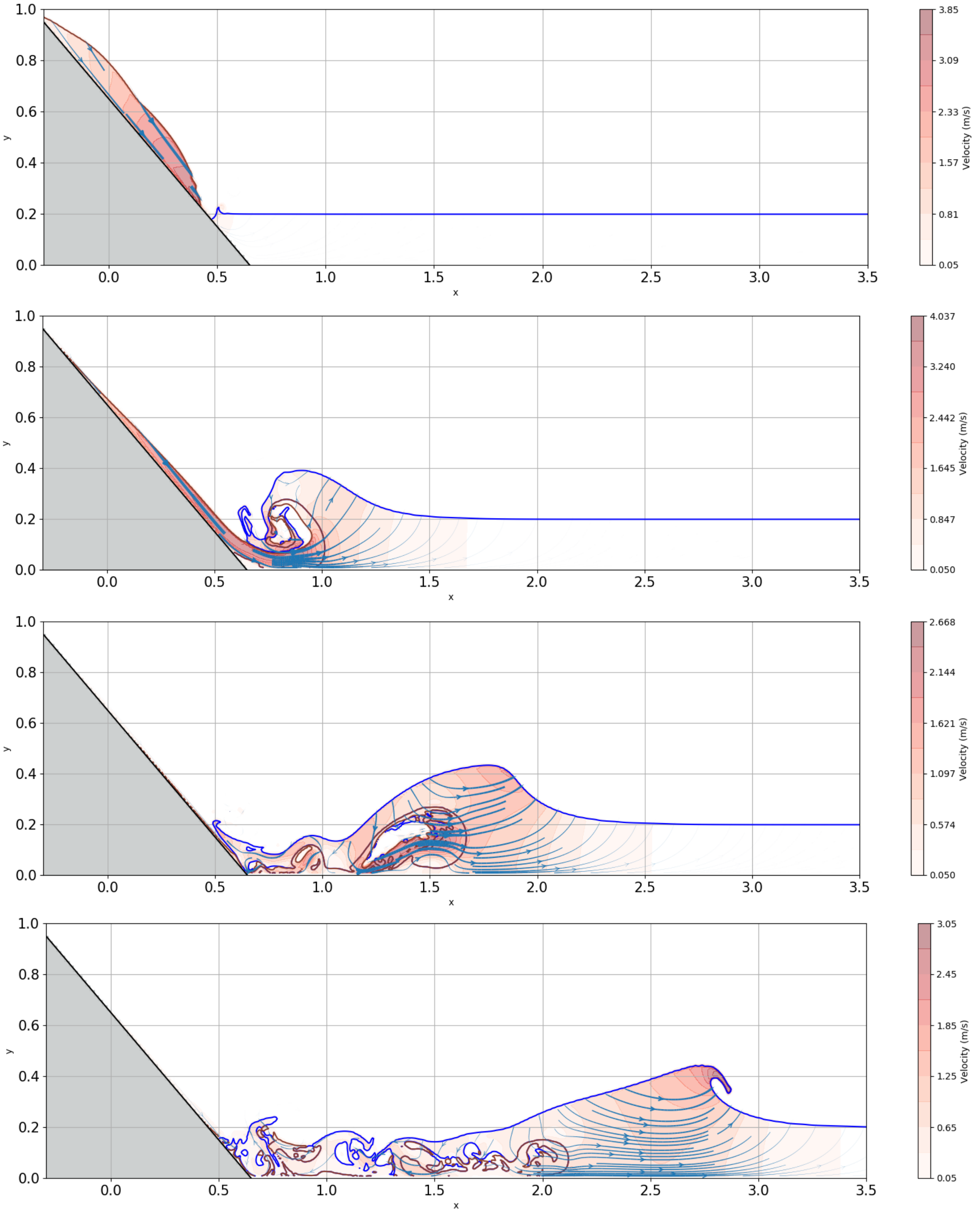

Figure 4.27 – Fluid interfaces, streamlines and velocity magnitude (surface field) at different times (top to bottom: t= 0.3s, 0.6s, 1s, 1.4s) for a slide case with $h_s = 2h_0$ and $h_l = 2.h_0$.

The energetic processes are summarized in figure 4.28. Note that before the slide collides with the water surface, our simulations reveal that, already, up to 5% of the initial slide energy has been dissipated due to the internal friction.

Let us consider first the larger slide volume ($h_s = 2h_0$). The (absolute) wave energy after generation strongly increases with the slide submergence, and so do the dissipation by breaking. As a result, the final wave energy also increases but rather mildly. In this case, the energy loss by dispersion is rather limited. Conversely, the relative wave energy after generation strongly decreases with the submergence. The fraction of the slide potential energy dissipated by breaking is more or less constant, and, as a result, the final relative energy decreases quite similarly as after the generation.

From these curves, we can conclude that the process of transforming the slide energy to the wave energy is less and less efficient with the increase of the submergence. Interestingly, the decrease of efficiency also affects the generation and not only the final wave energy. It is probably due to the effect of the strong dissipation induced by the back breaking of the cavity. The dissipation due to the leading wave breaking is also very efficient to dissipate the slide energy.

Finally, the global efficiency of the energy process (i.e., from slide energy to final wave energy) is quite low and decreases with the submergence (from 0.3 to 0.16).

In the lower volume slide case, the dispersion is obviously playing a much greater role. This is due to the very different wave characteristics after generation (Figure 4.29). In this case, as in the former case, we observe a decrease of the relative wave energy after generation due to the dissipation in the cavity area. From the generation area to the end of the domain, the energy of the leading wave is mainly lost by dispersion except for submergence between 0.5 and 1.25 where some stronger breaking should intervene. The final efficiency of the process ranges from 0.45 to only about 0.13.

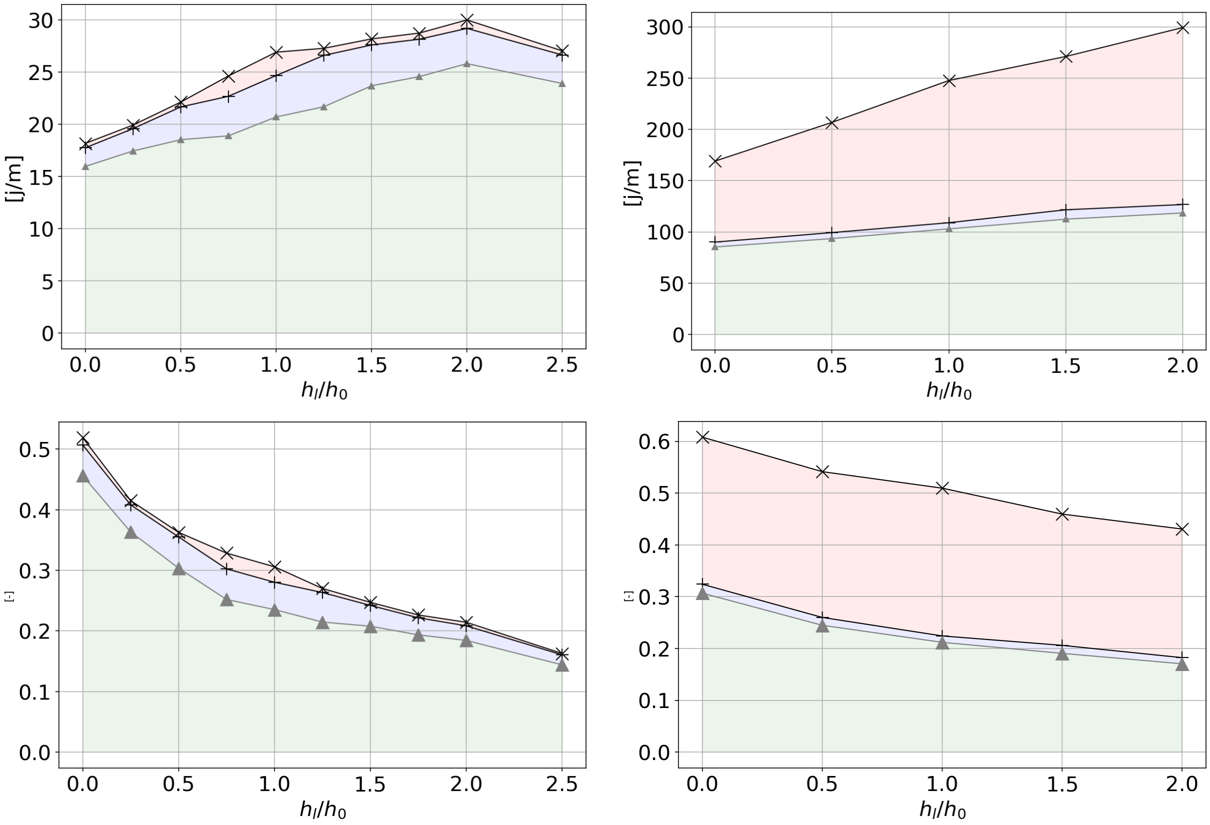

Figure 4.28 – Variation of absolute wave energies (top) and relative wave energies (bottom) with the slide initial elevation. Left : $h_s = h_0$, right : $h_s = 2h_0$. Apart from the x-axis, the notation is the same as in Figure 4.21.

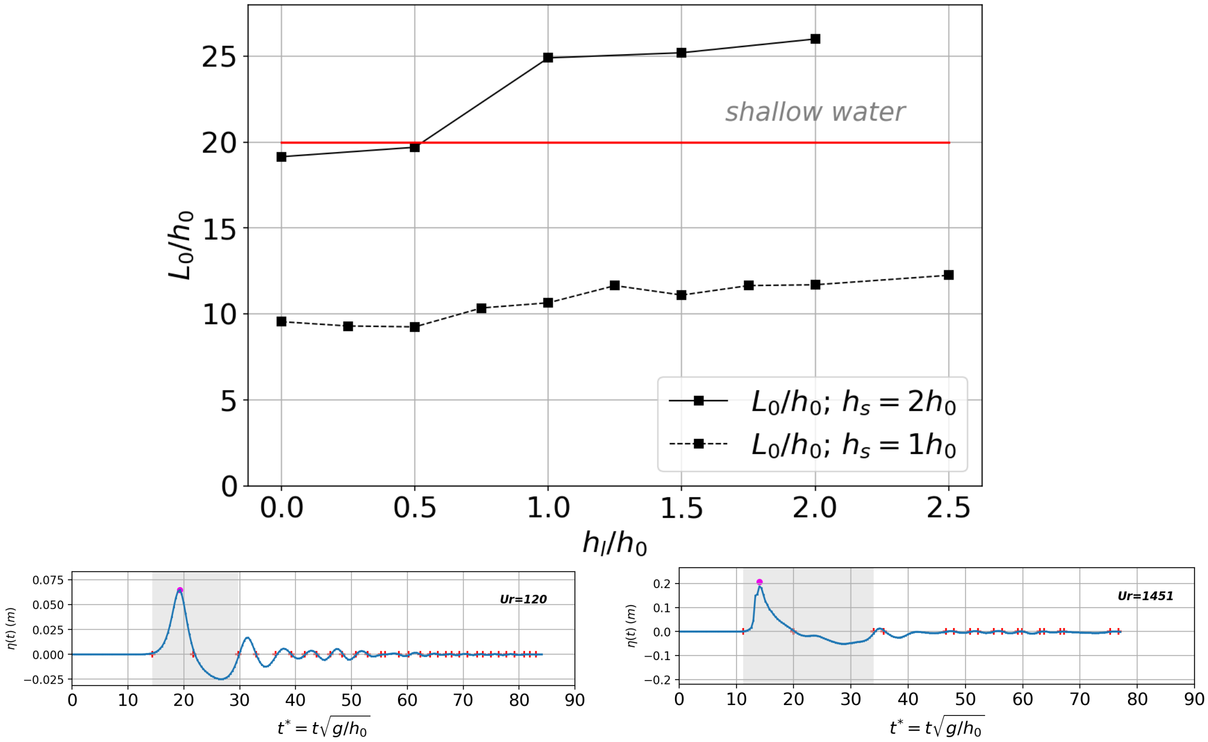

Figure 4.29 – Variation of the wave characteristics for slide with initial elevation cases. Top panel : the relative wavelength measured just after generation for two slide cases, Bottom panel : free surface profiles at $x = 4$m for the corresponding slide cases (left: $h_s = 1h_0$-$h_l = 2.5h_0$, right: $h_s = 1h_0$-$h_l = 2h_0$).

## 4.3 Wave generation : insights from all the cases simulated

In this section, we gather all the cases simulated in this study and try to find a common way to explain the relative efficiency of the wave generation. Table 4.2 summarizes the characteristics of the 44 cases investigated.

Table 4.2 – Data summary of all simulated cases are presented in Figure 4.30 to Figure 4.37.

| cases | $m_0$ $[kg/m]$ | $E_0$ $[J/m]$ | $E_{w(max))}$ $[J/m]$ | $I_{x(+)}$ $[N.s.m^{-1}]$ | $I_{x(-)}$ $[N.s.m^{-1}]$ | symbol |
|---|---|---|---|---|---|---|
| $h_s = 0.5h_0$ (inviscid) | 5.0 | 3.30 | 2.21 | 10.0 | -4.8 | ● |
| $h_s = 0.75h_0$ (inviscid) | 11.0 | 11.10 | 7.64 | 32.3 | -16.2 | |
| $h_s = 1h_0$ (inviscid) | 20.0 | 26.50 | 18.18 | 52.7 | -27.5 | |
| $h_s = 1.25h_0$ (inviscid) | 31.0 | 51.60 | 33.50 | 96.5 | -50.4 | |
| $h_s = 1.5h_0$ (inviscid) | 45.0 | 88.90 | 54.91 | 162.6 | -80.9 | |
| $h_s = 1.75h_0$ (inviscid) | 61.0 | 140.90 | 89.78 | 221.8 | -75.7 | |
| $h_s = 2h_0$ (inviscid) | 80.0 | 210.00 | 135.99 | 338.1 | -134.0 | |
| $h_s = 2.25h_0$ (inviscid) | 101.0 | 298.90 | 195.25 | 502.8 | -225.4 | |
| $h_s = 2.5h_0$ (inviscid) | 125.0 | 403.50 | 256.98 | 671.1 | -292.4 | |
| $h_s = 3h_0$ (inviscid) | 180.0 | 707.51 | 465.27 | 1305.5 | -707.9 | |
| $h_s = 3.5h_0$ (inviscid) | 245.0 | 1122.95 | 717.19 | 1982.2 | -1155.5 | |
| $h_s = 4h_0$ (inviscid) | 320.0 | 1675.71 | 1025.31 | 3087.4 | -2119.3 | |
| $\nu_s = 10\nu_w$ (viscous) | 80.0 | 210.00 | 135.41 | 230.7 | -101.2 | × |
| $\nu_s = 100\nu_w$ (viscous) | 80.0 | 210.00 | 132.10 | 150.0 | -69.7 | |
| $\nu_s = 1000\nu_w$ (viscous) | 80.0 | 210.00 | 117.01 | 90.5 | -1.1 | |
| $\nu_s = 10000\nu_w$ (viscous) | 80.0 | 210.00 | 78.00 | 7.5 | -0.1 | |
| $\nu_s = 100000\nu_w$ (viscous) | 80.0 | 210.00 | 23.05 | 0.0 | 0.0 | |
| $\tau_0 = 1$[Pa] (Bingham) | 80.0 | 210.00 | 73.72 | 87.3 | -0.9 | + |
| $\tau_0 = 10$[Pa] (Bingham) | 80.0 | 210.00 | 70.45 | 80.9 | -0.7 | |
| $\tau_0 = 50$[Pa] (Bingham) | 80.0 | 210.00 | 66.94 | 72.1 | -1.4 | |
| $\tau_0 = 100$[Pa] (Bingham) | 80.0 | 210.00 | 55.69 | 58.0 | -1.5 | |
| $\tau_0 = 125$[Pa] (Bingham) | 80.0 | 210.00 | 53.15 | 55.3 | -1.3 | |
| $\tau_0 = 150$[Pa] (Bingham) | 80.0 | 210.00 | 37.98 | 40.1 | -1.0 | |
| $\tau_0 = 200$[Pa] (Bingham) | 80.0 | 210.00 | 31.50 | 31.9 | -0.9 | |
| n=0.8 (H.B law) | 80.0 | 210.00 | 45.32 | 52.5 | -1.3 | ★ |
| n=0.6 (H.B law) | 80.0 | 210.00 | 50.49 | 102.2 | -32.6 | |
| n=0.4 (H.B law) | 80.0 | 210.00 | 54.71 | 136.9 | -96.2 | |
| n=0.3 (H.B law) | 80.0 | 210.00 | 56.39 | 136.6 | -140.5 | |
| n=0.2 (H.B law) | 80.0 | 210.00 | 57.84 | 130.4 | -121.4 | |
| $h_s = 1h_0$-$h_l = 0$ | 26.5 | 35.11 | 18.17 | 48.6 | -10.7 | ▲ |
| $h_s = 1h_0$-$h_l = 0.25h_0$ | 26.5 | 48.26 | 19.93 | 71.8 | -33.9 | |
| $h_s = 1h_0$-$h_l = 0.5h_0$ | 26.5 | 61.41 | 22.13 | 113.0 | -67.2 | |
| $h_s = 1h_0$-$h_l = 0.75h_0$ | 26.5 | 74.54 | 24.64 | 139.3 | -102.9 | |
| $h_s = 1h_0$-$h_l = 1h_0$ | 26.5 | 87.60 | 26.92 | 170.3 | -125.8 | |
| $h_s = 1h_0$-$h_l = 1.25h_0$ | 26.5 | 100.87 | 27.29 | 203.4 | -153.3 | |
| $h_s = 1h_0$-$h_l = 1.5h_0$ | 26.5 | 114.02 | 28.19 | 240.7 | -194.9 | |
| $h_s = 1h_0$-$h_l = 1.75h_0$ | 26.5 | 127.17 | 28.75 | 264.5 | -260.9 | |
| $h_s = 1h_0$-$h_l = 2h_0$ | 26.5 | 140.31 | 30.01 | 282.1 | -278.2 | |
| $h_s = 1h_0$-$h_l = 2.5h_0$ | 26.5 | 166.42 | 27.04 | 371.1 | -324.6 | |
| $h_s = 2h_0$-$h_l = 0$ | 105.8 | 277.83 | 169.04 | 362.9 | -109.5 | ■ |
| $h_s = 2h_0$-$h_l = 0.5h_0$ | 105.8 | 382.25 | 206.81 | 508.2 | -163.6 | |
| $h_s = 2h_0$-$h_l = 1h_0$ | 105.8 | 486.50 | 247.62 | 870.6 | -535.6 | |
| $h_s = 2h_0$-$h_l = 1.5h_0$ | 105.8 | 590.48 | 271.07 | 1258.4 | -952.7 | |
| $h_s = 2h_0$-$h_l = 2h_0$ | 105.8 | 694.97 | 299.28 | 2586.2 | -2349.9 | |

Figure 4.30 first presents the relationship between the wave energy after generation (i.e., the maximum wave energy) and the initial slide energy. If for water/water cases, the relation is linear and close to $y = 0.6x$, when increasing the submergence, a lower slope is observed, which is the sign of a lower

efficiency. More importantly, the dataset corresponding to different rheological parameters shows that significantly different wave energy values can be obtained with the same initial slide energy.

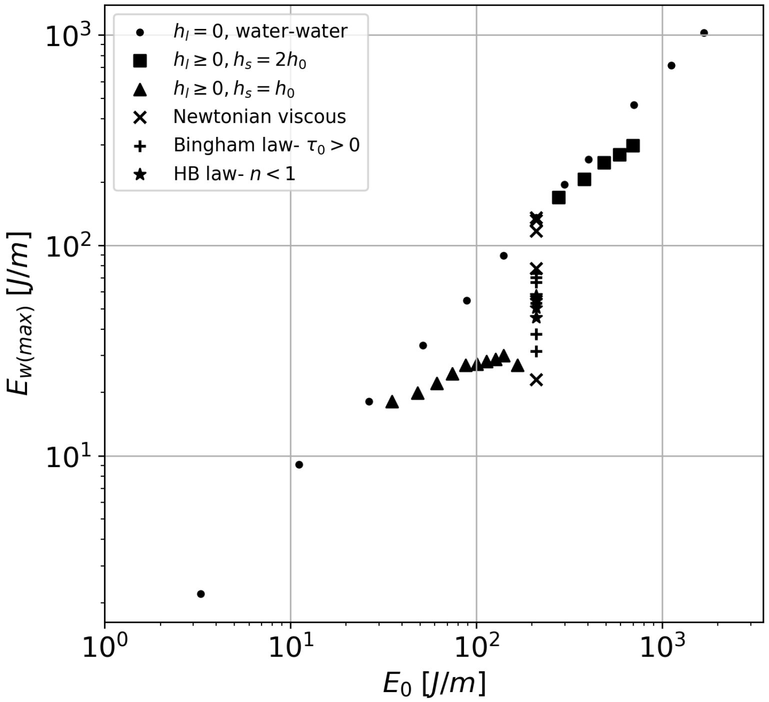

Figure 4.30 – Relationship between the maximum wave energy ($E_{w(max)}$) and the initial slide energy ($E_0$) for all the cases simulated.

As pointed out in the literature review chapter, the slide mass is often invoked as being the most important parameter to predict the maximum wave amplitude (Rauter et al., 2021). We also investigated this hypothesis in figure 4.31. This plot shows that the slide mass is indeed a good predictor of the maximum wave energy. The two sets of simulations with similar mass values (i.e., 26.4 and 105.8 kg/m, respectively) but different initial slide energy (in red) due to the submergence, demonstrate that this extra initial energy is not an important parameter to predict the transferred wave energy. Nevertheless, mass is not sufficient for an accurate prediction. The slide rheology information is also required as pointed out by the significant dispersion observed for the points with the same mass (m=80 kg/m) but different rheology parameters (The most viscous case among the Newtonian slide simulations being the lowest).

In the following, we try to consider the slide momentum flux and the impulse, as introduced previously in section 4.1.2, in this analysis. Note that the term impulse refers to the integral in time of the momentum flux, but can similarly be considered as the slide force impulse as shown in figure 4.10.

The understanding of the global energetic process transforming slide energy to wave energy can maybe be further improved by introducing the concept of the momentum flux. In figures 4.32 and 4.33, we try to use the horizontal positive impulse $I_x(+)$ as a proxy. The first figure shows how the slide energy is transferred to the impulse. While the second one shows how this impulse then transfer to the wave energy.

From Figure 4.32, we can observe that the energy of the water slides with no submergence or the Herschel-Bulkley slides with submergence, is proportional to the horizontal thrust exerted on the water body. Conversely, cases with no submergence, do not show this correlation with the thrust as evidenced by the vertically aligned set of points. In addition, the vertically aligned set of points corresponding to "low-mobility" rheological slides with the same value of $E_0$ shows that the great range

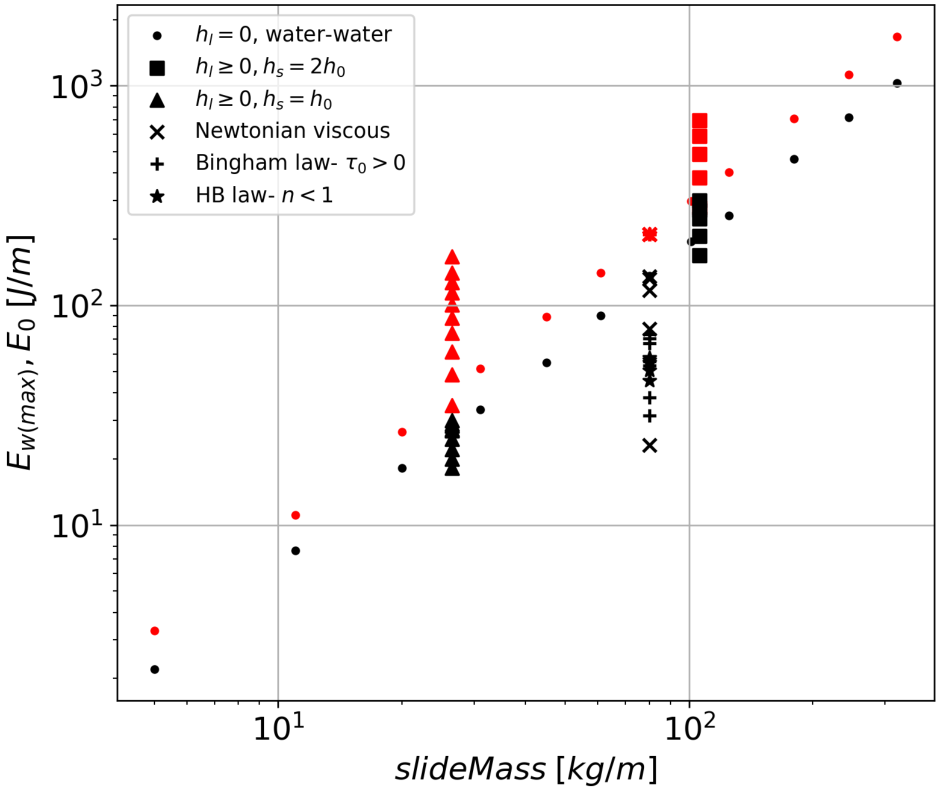

Figure 4.31 – Relationship between the slide mass and : black - the maximum wave energy ($E_{w(max)}$), red - the initial slide energy ($E_0$) for all the cases simulated.

of thrusts can obtained depending on the rheological parameters and that the efficiency is usually lower than for the previous group of simulations (i.e., water/water and slide with initial elevation).
Figure 4.33 now examines the capacity of the slide horizontal positive thrust to produce wave energy. While for the water/water cases, the slope is comparable to the previous figure, for the cases with initial elevated slides, it is strongly reduced evidencing a significant loss of efficiency when producing the wave. Now considering the set of simulations in which the rheological parameters were varied, while they were globally not efficient to produce the thrust to the water body, the efficiency of this thrust is high compared to the other cases.
This plot also demonstrates that the horizontal positive impulse $I_{x(+)}$ is not sufficient in itself to describe the phenomenon as a common value of this parameter of, say 100, may lead to very different wave energy after generation.
In Figure 4.34, the time variation of the slide momentum flux components is presented for two simulations with initial elevation. These simulations corresponds to the snapshots of figure 4.26 and 4.27. In comparison to water/water cases in which the submergence is equal to 0 (figure 4.8), here, we note a relative increase of the influence of the negative components and especially $F_x(-)$ which reaches the same level in absolute value as $F_x(+)$. We recall that the latter was predominant in the water/water cases. The relative increase of $F_x(-)$ is attributed to the cavity formation and the subsequent back breaking, visible in figures 4.26 and 4.27. In these stages, a significant fraction of the slide surface is pushing water to the left, hence the growth of $F_x(-)$.
As in the case of a water slide (figure 4.8), we remark that $F_y$ coexists with $F_x$ but its magnitude is lower.
From the observations made in the previous paragraph, we make the following assumptions. First, $I_{x(-)}$

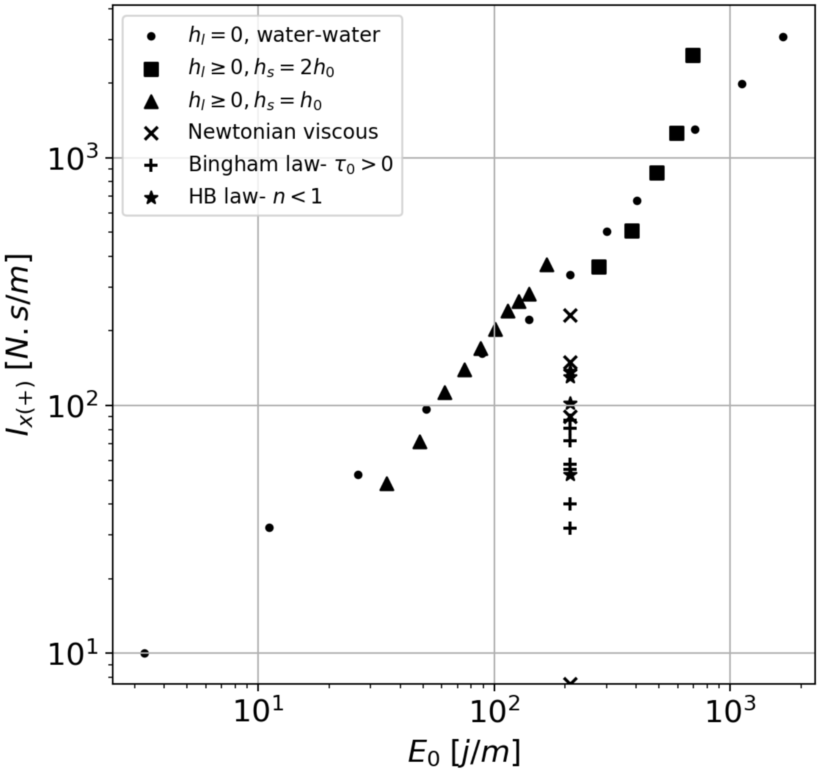

Figure 4.32 – Relationship between the positive horizontal impulse ($I_{x(+)}$) and the initial slide energy $E_0$ considering all the simulations.

plays a role in the wave generation process and therefore it should be considered in our investigations in conjunction with $I_{x(+)}$. Second, the magnitude of the vertical component being generally lower than the horizontal components, the latter is neglected in the following approach. Third, the positive horizontal impulse $I_{x(+)}$ is supposed to favor the growth of the wave energy, while conversely, the negative horizontal impulse will limit it by redirecting the energy to the left part of the domain. Therefore, $I_{x(+)}$ is supposed to have a "constructive" on the wave energy growth, while $I_{x(-)}$ will have a "destructive" effect, which in summary gives :

$$\mathbf{E_0} \Rightarrow \mathbf{E_s} \rightleftharpoons \underbrace{\begin{cases} I_{x(+)} \ (\textbf{constructive} \quad \textbf{role}) \\ I_{x(-)} \ (\textbf{destructive} \quad \textbf{role}) \end{cases}}_{participation\,in\,E_w\,growth} \rightleftharpoons E_{w(max)}.$$

Where $E_s$ is the slide energy at impact.

In figure 4.35, we have superimposed the $I_{x(-)}$ values in red onto the plot already presented in figure 4.32 relying $E_0$ to $I_{x(+)}$. This way, for each case, we can assess the relative importance of $I_{x(-)}$ and $I_{x(+)}$.

For the water/water cases, the trends is not very clear but there is a tendency for both components to be closer to each other for larger slide energy. Nevertheless, both values are never equal. In this set of simulations, the appearance of $I_{x(+)}$ and seems particularly related to the presence of slide material over the wave crest, subsequently entrained in the breaking. In this case, as in this area the slide material is split into small pieces, it is difficult to ensure the accuracy of the parameter studied and hence its significance. Because they are vertically aligned, the difference between $I_{x(+)}$ and $I_{x(-)}$ for the set of points corresponding to different rheologies is difficult to assess.

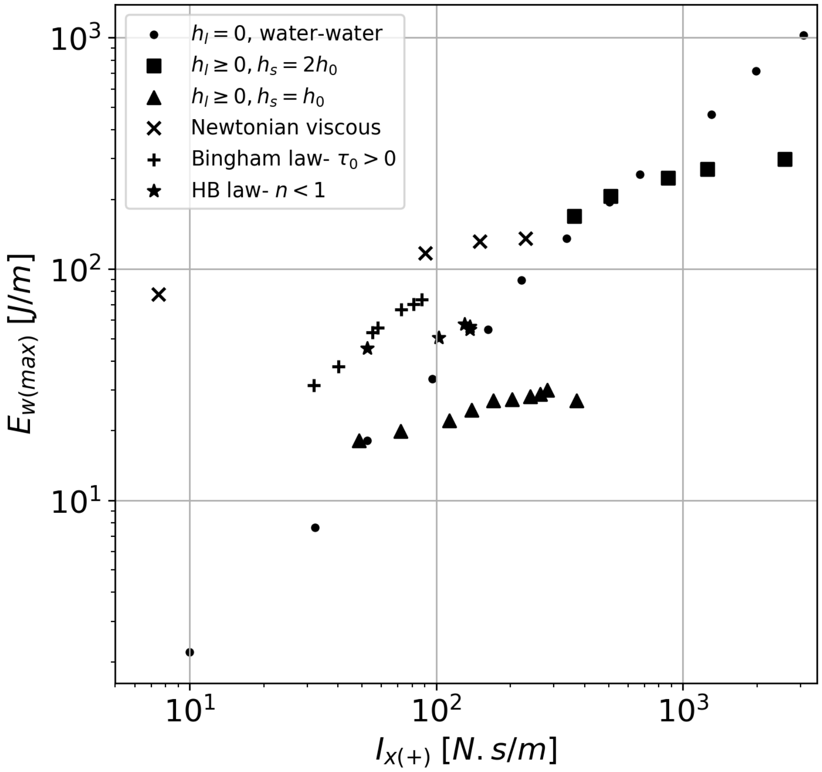

Figure 4.33 – Relationship between the positive horizontal impulse ($I_{x(+)}$) and the maximum wave energy $E_{w(max)}$ considering all the simulations.

Conversely, this figure allows to draw a very clear conclusion for the cases with slide with initial elevation. For both, the triangle or the square markers, red and black converge progressively to the same values when the submergence is increased. It means, that with more initial elevation, the proportion of positive and negative horizontal impulses tends to 1.
In figure 4.36 we tried to introduce the effect of $I_{x(-)}$. The variable investigated is the ratio $E_{w(max)}/I_{x(+)}$, which can be seen as the efficiency of $I_{x(+)}$ to produce wave energy.
On the left plot, only $I_{x(+)}$ is used to explain $E_{w(max)}/I_{x(+)}$. In this plot, we observe different behaviors. With increasing submergence, the process is less and less efficient as evidenced by the decreasing slopes observed for the corresponding sets of simulations. For the water/water cases, the efficiency is slightly increasing with the volume then slightly decreasing. The "rheological" set is characterized by a high efficiency, especially for the slide behaving like solids (i.e., Bingham cases with high yield stress or Herschel Bulkley cases with n values not departing too much from 1). The cases with higher mobility behaves closer to the water/water set. Globally, this plot does not show a clear trend which tends to demonstrate that $I_{x(+)}$ is not self sufficient.
On the right plot, we introduce a new parameter defined as : $EIR = (I_{x(+)} - |I_{x(-)}|)/I_{x(+)}$ for Efficient Impulse Ratio. By calculating the difference between $I_{x(+)}$ and $I_{x(-)}$, we try somehow to quantify the "efficient" part of the impulse. By dividing by $I_{x(+)}$ we obtain a parameter varying between 0 and 1. We put both plots side to side to be able to identify the points with their ordinates. With this way of plotting the data, except for 2 or 3 outliers, there is a global trend appearing. The cases with high submergences values have low EIR. Their EIR increase with the diminution of the submergence and so do the energetic efficiency $E_{w(max)}/I_{x(+)}$. All the water/water cases show approximately the same efficiency $E_{w(max)}/I_{x(+)}$ and on the EIR scale, they are also very close to each other. Finally, with the variation of the slide rheology, and in particular when the mobility of the slide is strongly reduced

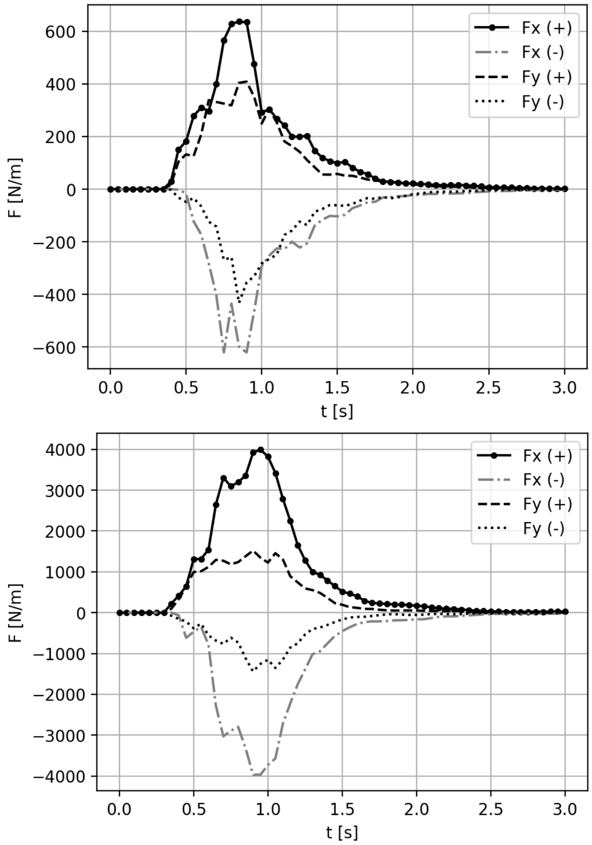

Figure 4.34 – Time evolution of the four components of the momentum flux through the slide water interface for two simulation cases. top : $h_s = 1h_0$ and $h_l = 2.5h_0$, bottom : $h_s = 2h_0$ and $h_l = 2h_0$.

for instance due to the yield stress, the energy efficiency $E_{w(max)}/I_{x(+)}$ increases, and so do the EIR. The final figure of this study (figure 4.37) shows the relationship between the global energy process from $E_0$ to $E_{w(max)}$ and the EIR. On this plot, the water/water cases are the most efficient to transfer the slide energy to the wave with a maximum around 68%. Then we find the low initial elevation cases, which involve quite mobile slides. But their efficiency decrease with the submergence and so do the EIR. Finally, with low mobility, the slides on the bottom right part of the plot have the highest EIR but their global efficiency is strongly reduced by their capacity to produce $I_{x(+)}$ as already pointed out.

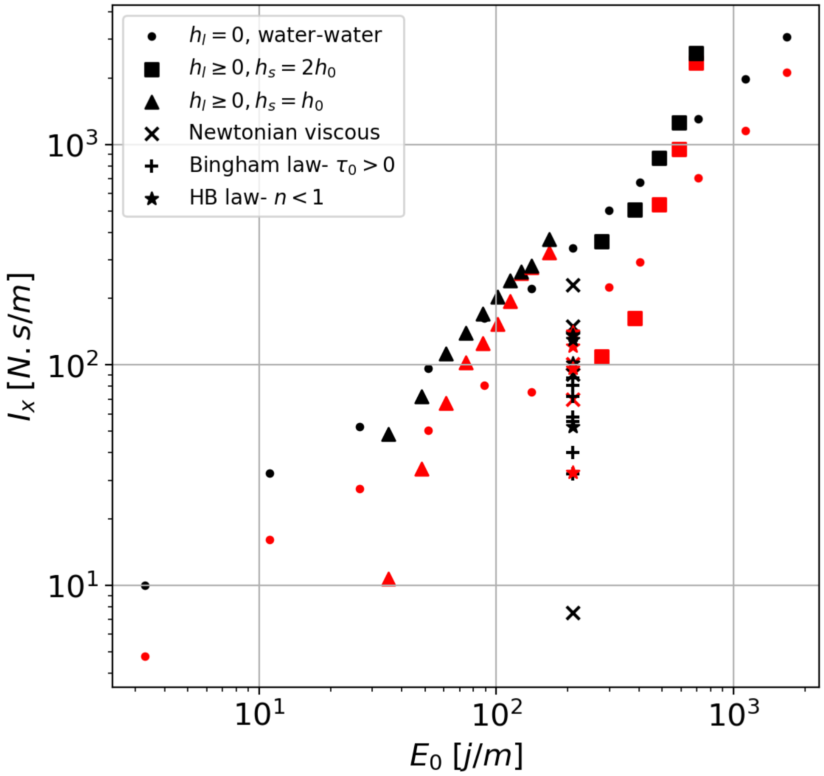

Figure 4.35 – Same as figure 4.32 with $I_{x(-)}$ values in red.

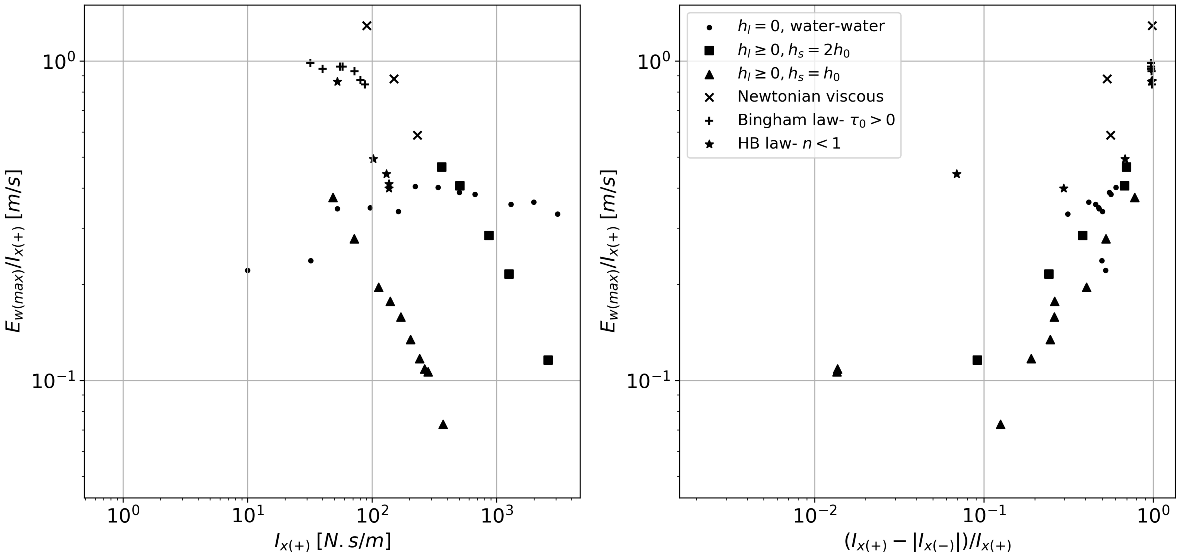

Figure 4.36 – Efficiency of $I_{x(+)}$ to generate wave energy $E_{w(max)}$. Left : in function of $I_{x(+)}$ only, right : introducing the effect of $I_{x(-)}$ through the new parameter $EIR = (I_{x(+)} - |I_{x(-)}|)/I_{x(+)}$.

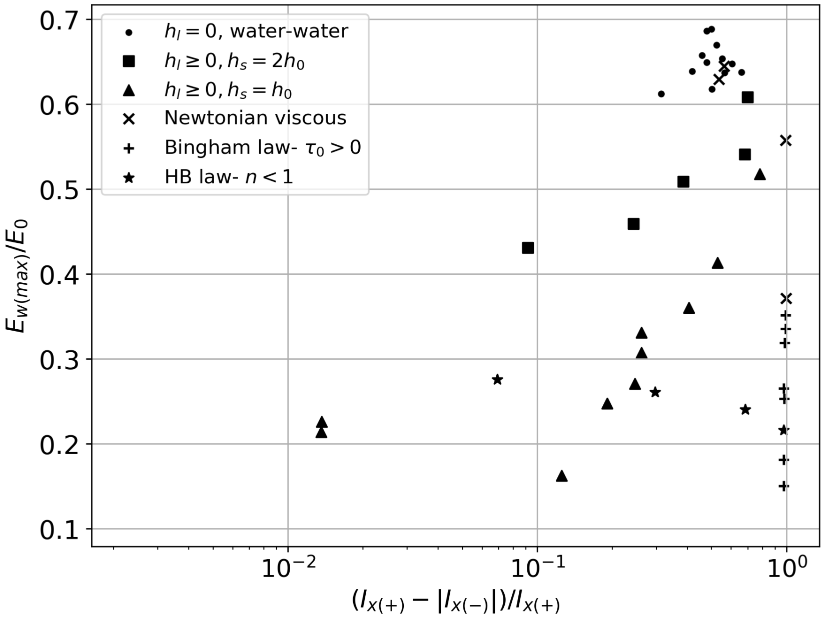

Figure 4.37 – Global energetic efficiency $E_{w(max)}/E_0$ against $EIR = (I_{x(+)} - |I_{x(-)}|)/I_{x(+)}$ for all the test cases.

# Chapter 5

# Conclusion and perspectives

## 5.1 Goals of the work and approach followed

This thesis aimed at improving the understanding of the generation and subsequent transformations of the impulse wave generated by a sub-aerial slide. We specifically studied fluid-like slides with more or less complex rheological laws representing, in reality, particular landslides such as mud-flow. For that purpose, a numerical model, namely Multiphase - InterFoam, was used. The originality of our approach was to look specifically at the energetic processes.

To achieve this goal, several steps were taken.

The first step was to assess the model suitability and accuracy to describe the process studied. We performed a series of validation cases, each designed to cover a specific aspect of the main problem. This exercise basically resulted in the best choices of numerical parameters and in an acceptable compromise concerning the mesh resolution, relative to the wave height for instance, to achieve an accurate result or, at least, an acceptable one.

To this purpose, several more or less idealized situations were investigated : the motion of a rheological Herschel-Bulkley law fluid on a slope, the generation of an impulse wave and the breaking inception or the wave dispersion processes, both investigated through wet dam break experimental data.

To achieve a comprehensive understanding of the energetic processes at stake in this phenomenon, it was necessary to carefully determine each component of the energy transfers including dissipation (physical and inevitably, numerical) and validate them, through, again, a step-by-step approach.

This procedure started with a two-phase Couette test with the goal to validate the "strain rate" computation accuracy as the main factor in the viscous energy dissipation term. Then a test involving a propagating solitary wave showed the influence of the cell dimensions on the accuracy of the wave potential energy as well as on the global conservation of the energy. Energy conservation was also tested in the case of a solitary wave breaking. At this step, the most appropriate turbulence model was determined by minimizing the numerical dissipation. Nevertheless, the numerical dissipation could only be partially limited due to CPU constraint. In the final validation case, we investigated the accuracy of the physical dissipation in turbulent bores by comparing with the theoretical formulae. We achieved a satisfactory accuracy after the optimisation of the turbulence initial parameters.

Once the model validated and the final set-up determined, we followed two main axes of study:

1. a detailed investigation of the whole energy transfer process from the initial slide to the final leading wave energy focusing on the wave transformation processes, and considering water slides with different volumes,
2. a more global investigation of the changes in the energy transfers by progressively increasing the slide rheological complexity (up to realistic clay-water characteristics) and the submergence.

## 5.2 Conclusion of current work

In the water slide study, the volume variation changed drastically the wave physics. Indeed, the volume has been shown to control the wave type, the breaking type and the spatial distribution of the usual zones (generation, near field, etc.). We demonstrated that, in the range of the volumes tested, the leading waves were strongly non linear and that the propagation celerity depended on the breaking condition and could be accurately estimated either by the theoretical bore or solitary wave formulations, depending on the stage. Additionally, the study of the generation stage showed that the leading wave breaking and energy dissipation occurred before the end of the energy transfer from slide to wave.

The physical dissipation was shown to be maximum at the beginning of the breaking in the so-called transition zone. This zone can overlap with the generation zone. The breaking was also shown to be controlled by the excessive energy received by the wave during generation, resulting in a kinetic to potential energy ratio above 2. Depth or steepness are not the reason of breaking but they can intervene as secondary factors in particular cases.

The ratio of the maximum wave energy (i.e., just after generation) to the initial slide energy was found to be quite stable around 0.6. Nevertheless, after generation, the wave processes involved may differ significantly depending on the slide volume. Oscillatory-type waves redistribute the leading wave energy to the rest of the wave-train mainly by frequency dispersion. Conversely, the larger slides generate non dispersive waves which breaking almost entirely controls the final wave energy. Hence, the two superimposing processes (i.e., dispersion and breaking) shape the final energy content of the leading wave. They are counter-effective, namely, when one is strong the other one is weak. Consequently, although the absolute value of the leading wave energy increases with the slide volume, the global efficiency of the energy transfer process (i.e., the ratio of the final leading wave energy to the slide energy) shows an optimum for an intermediate slide volume.

The next phase of the thesis was dedicated to the rheology and submergence effects. Regarding the rheology, the slides with more mobility (low viscosity) were demonstrated to be more efficient in transferring their energy to the impulse wave. In addition, among all the tested rheological parameters, the yield stress was shown to be the more influential parameter in reducing this efficiency. Different slide submergences were also tested. The energy transfer efficiency is shown to decrease with submergence. This is due to the way the very violent slide interacts with water, creating large cavities, back breaking and therefore very strong local dissipation.

The final stage consisted of gathering all the cases and trying to determine the important parameters which may explain the behavior observed. We first confirmed the previous findings of the literature, that the slide mass is a very important parameter to explain the maximum energy of the wave. Nevertheless, mass is not sufficient as it can not explain the variation observed when varying the rheological properties of the slide.

We then investigated the concept of the momentum flux and its time integrated version, the impulse, in order to better understand the generation stage. We assumed the horizontal impulse to be the main contributor of the wave growth and decomposed it into positive (constructive) and negative (destructive) components. The positive component, by pushing the water mass, raises the wave energy level while the negative one, represents the returned energy to the slide. The latter directly relates to the post-impact slide dynamics which, in turn, depends on the impact mechanism and the slide rheological parameters.

We finally defined a new parameter called Efficient Impulse Ratio (EIR), which measures the fraction of horizontal impulse left for wave generation. This parameter explains well the ability of the positive impulse to generate the wave. Hence, water slides with arbitrary volumes have similar EIR, while slide submergence, for a realistic rheology, decreases the EIR and hence the efficiency. Finally, the slides with low mobility (high viscosity or yield stress) exhibit the highest efficiency ratios even though the absolute wave energy remains weak due to the small impulse produced.

### 5.2.1 Proposition for further studies

The present work suffers from a few limitations which are underlined hereafter.

First, our results are entirely based on numerical simulations. Even though a careful validation of the model has been carried out, this research could benefit from new physical data involving high mobility slides (such as water) in a 2D channel. Previous work have been conducted in this direction (Bullard et al., 2019) but the effort should be continued, involving for instance, higher viscosities or more complex fluid rheologies.

Second, the parameters studied in this work are very limited in numbers. Many other possible parameters such as density, slope angle, slide initial shape, three dimensionality, non-uniform water depth in the basin, etc. could and should be considered in future research.

Last, if the EIR gives an interesting perspective, it is not yet predictive as, so far, no direct relationship has been established between this parameter and the initial slide characteristics. It would be interesting to investigate this relationship to better understand for instance how the negative impulse depends on the slide characteristics. The vertical components of the impulse have been neglected and they should be looked at more carefully. Finally, the high efficiency of the low mobility slides ask for further investigations. To this respect, it would be interesting to try increasing the generation of impulse, for this type of slide by, for instance, limiting the friction with the slope, and verify if the EIR is affected or not.

# Chapter 6

# Bibliography

Akae, T. and Low, P. F. (1988). Interparticle bond energy and rheological properties of clay suspensions. *Journal of Colloid and Interface Science*, 124(2):624–631.

Alene, G., Irshad, S., Thakur, V., Perkis, A., and Bruland, O. (2022). Integration of Numerical Simulation of flow landslides into Virtual Reality: A framework.

Ancey, C. and Cochard, S. (2009). The dam-break problem for Herschel–Bulkley viscoplastic fluids down steep flumes. *Journal of Non-Newtonian Fluid Mechanics*, 158(1):18–35.

Ataie-Ashtiani, B. and Nik-Khah, A. (2008). Impulsive waves caused by subaerial landslides. *Environmental Fluid Mechanics*, 8(3):263–280.

Balmforth, N. J., Craster, R. V., Rust, A. C., and Sassi, R. (2007). Viscoplastic flow over an inclined surface. *Journal of Non-Newtonian Fluid Mechanics*, 142(1):219–243.

Battershill, L., Whittaker, C. N., Lane, E. M., Popinet, S., White, J. D. L., Power, W. L., and Nomikou, P. (2021). Numerical Simulations of a Fluidized Granular Flow Entry Into Water: Insights Into Modeling Tsunami Generation by Pyroclastic Density Currents. *Journal of Geophysical Research: Solid Earth*, 126(11):e2021JB022855.

Beverly, C. and Tanner, R. (1992). Numerical analysis of three-dimensional bingham plastic flow. *Journal of Non-Newtonian Fluid Mechanics*, 42(1):85–115.

Bolin, H., Yueping, Y., Xiaoting, C., Guangning, L., Sichang, W., and Zhibing, J. (2014). Experimental modeling of tsunamis generated by subaerial landslides: two case studies of the Three Gorges Reservoir, China. *Environmental Earth Sciences*, 71(9):3813–3825.

Bougouin, A., Paris, R., and Roche, O. (2020). Impact of fluidized granular flows into water: Implications for tsunamis generated by pyroclastic flows. *Journal of Geophysical Research: Solid Earth*, 125(5).

Boussinesq, J. (1872). Théorie des ondes et des remous qui se propagent le long d'un canal rectangulaire horizontal, en communiquant au liquide contenu dans ce canal des vitesses sensiblement pareilles de la surface au fond. *Journal de Mathématiques Pures et Appliquées*, pages 55–108.

Boussinesq, J. (1877). *Essai sur la théorie des eaux courantes.* Mémoires présentés par divers savants à l'Académie des Sciences 23(1). Impr. nationale. Google-Books-ID: QAuWqaSZqvEC.

Brackbill, J. U., Kothe, D. B., and Zemach, C. (1992). A continuum method for modeling surface tension. *Journal of computational physics*, 100(2):335–354.

Brown, S. A., Greaves, D. M., Magar, V., and Conley, D. C. (2016). Evaluation of turbulence closure models under spilling and plunging breakers in the surf zone. *Coastal Engineering*, 114:177–193.

Bullard, G. K., Mulligan, R. P., Carreira, A., and Take, W. A. (2019). Experimental analysis of tsunamis generated by the impact of landslides with high mobility. *Coastal Engineering*, 152:103538.

Carotenuto, C., Merola, M. C., Álvarez Romero, M., Coppola, E., and Minale, M. (2015). Rheology of natural slurries involved in a rapid mudflow with different soil organic carbon content. *Colloids and Surfaces A: Physicochemical and Engineering Aspects*, 466:57–65.

Chhabra, R. P. and Richardson, J. F. (1999). *Non-Newtonian flow in the process industries: fundamentals and engineering applications.* Butterworth-Heinemann, Oxford; Boston, MA. OCLC: 182747857.

Clous, L. and Abadie, S. (2019). Simulation of energy transfers in waves generated by granular slides. *Landslides*, 16(9):1663–1679.

Coussot, P. (1994). Steady, laminar, flow of concentrated mud suspensions in open channel. *Journal of Hydraulic Research*, 32(4):535–559.

Coussot, P. (1997). *Mudflow Rheology and Dynamics.* Rotterdam: Balkema.

Coussot, P., Laigle, D., Arattano, M., Deganutti, A., and Marchi, L. (1998). Direct determination of rheological characteristics of debris flow. *Journal of hydraulic engineering*, 124(8):865–868.

Coussot, P. and Meunier, M. (1996). Recognition, classification and mechanical description of debris flows. *Earth-Science Reviews*, 40(3):209–227.

Coussot, P. and Piau, J. M. (1994). On the behavior of fine mud suspensions. *Rheologica acta*, 33(3):175–184.

Coussot, P. and Piau, J.-M. (1995). The effects of an addition of force-free particles on the rheological properties of fine suspensions. *Canadian geotechnical journal*, 32(2):263–270.

Couston, L.-A., Mei, C. C., and Alam, M.-R. (2015). Landslide tsunamis in lakes. *Journal of Fluid Mechanics*, 772:784–804.

Cruden, D. and Varnes, D. (1996). Landslides types and processes. in: Turner, a.k., schuster, r.l. (eds.), landslides: Investigation and mitigation. *Special Report, 247. Transportation, Research Board, National Research Council, Washington, DC*, pages 36–75.

Dahl-Jensen, T., Larsen, L. M., Pedersen, S. A. S., Pedersen, J., Jepsen, H. F., Pedersen, G., Nielsen, T., Pedersen, A. K., Von Platen-Hallermund, F., and Weng, W. (2004). Landslide and tsunami 21 november 2000 in paatuut, west greenland. *Natural Hazards*, 31:277–287.

Dasgupta, P. (2003). Sediment gravity flow—the conceptual problems. *Earth-Science Reviews*, 62(3-4):265–281.

Datei, C. (2005). *Vajont: la storia idraulica.* Cortina.

Davies, H. (2017). *Aitape Story: The Great New Guinea Tsunami of 1998.* Halstead Press.

De Kee, D., Chhabra, R., Powley, M., and Roy, S. (1990). Flow of Viscoplastic Fluids on an Inclined Plane: Evaluation of Yield Stress. *Chemical Engineering Communications*, 96(1):229–239.

De Lange, S. I., Santa, N., Pudasaini, S. P., Kleinhans, M. G., and de Haas, T. (2020). Debris-flow generated tsunamis and their dependence on debris-flow dynamics. *Coastal Engineering*, 157:103623.

Dean, R. G. and Dalrymple, R. A. (1991). *Water Wave Mechanics for Engineers and Scientists*, volume 2 of *Advanced Series on Ocean Engineering*. World scientific.

Deike, L., Popinet, S., and Melville, W. K. (2015). Capillary effects on wave breaking. *Journal of Fluid Mechanics*, 769:541–569.

Devolder, B., Rauwoens, P., and Troch, P. (2017). Application of a buoyancy-modified k-omega SST turbulence model to simulate wave run-up around a monopile subjected to regular waves using OpenFOAM®. *Coastal Engineering*, 125:81–94.

Devolder, B., Troch, P., and Rauwoens, P. (2018). Performance of a buoyancy-modified k-omega and k-omega SST turbulence model for simulating wave breaking under regular waves using OpenFOAM®. *Coastal Engineering*, 138:49–65.

Dumergue, L. E. and Abadie, S. (2022). Numerical study of the wave impacts generated in a wet dam break. *Journal of Fluids and Structures*, 114:103716.

Evers, F. M. (2017). *Spatial Propagation of Landslide Generated Impulse Waves*. PhD thesis, ETH Zurich.

Evers, F. M. and Hager, W. H. (2015). Impulse Wave Generation: Comparison of Free Granular with Mesh-Packed Slides. *Journal of Marine Science and Engineering*, 3(1):100–110.

Fine, I. V., Rabinovich, A. B., Bornhold, B., Thomson, R., and Kulikov, E. A. (2005). The grand banks landslide-generated tsunami of november 18, 1929: preliminary analysis and numerical modeling. *Marine Geology*, 215(1-2):45–57.

Fritz, H. M. (2002). *Initial phase of landslide generated impulse waves*. Doctoral Thesis, ETH Zurich.

Fritz, H. M., Hager, W. H., and Minor, H.-E. (2004). Near Field Characteristics of Landslide Generated Impulse Waves. *Journal of Waterway, Port, Coastal, and Ocean Engineering*, 130(6):287–302.

Fritz, H. M. and Liu, P. C. (2001). An Application of Wavelet Transform Analysis to Landslide-Generated Impulse Waves. *Ocean Wave Measurement and Analysis*, pages 1477–1486.

Geertsema, M., Menounos, B., Bullard, G., Carrivick, J. L., Clague, J., Dai, C., Donati, D., Ekstrom, G., Jackson, J. M., Lynett, P., et al. (2022). The 28 november 2020 landslide, tsunami, and outburst flood–a hazard cascade associated with rapid deglaciation at elliot creek, british columbia, canada. *Geophysical research letters*, 49(6):e2021GL096716.

Greenshields, C. (2018). *OpenFOAM v6 User Guide: 7.3 Transport/rheology models*.

Grimshaw, R. (1970). The solitary wave in water of variable depth. *Journal of Fluid Mechanics*, 42(3):639–656.

Grossmann, A. and Morlet, J. (1984). Decomposition of Hardy Functions into Square Integrable Wavelets of Constant Shape. *SIAM Journal on Mathematical Analysis*, 15(4):723–736.

Han, L., Wang, P., and Yu, T. (2022). Wave types and energy conversion of impulse waves generated by landslides into mountain reservoirs. *Scientific Reports*, 12(1):4035.

Harbitz, C. B., Glimsdal, S., Løvholt, F., Kveldsvik, V., Pedersen, G. K., and Jensen, A. (2014). Rockslide tsunamis in complex fjords: From an unstable rock slope at Åkerneset to tsunami risk in western Norway. *Coastal Engineering*, 88:101–122.

Hato, M. J., Zhang, K., Ray, S. S., and Choi, H. J. (2011). Rheology of organoclay suspension. *Colloid and Polymer Science*, 289(10):1119–1125.

Heinrich, P. (1992). Nonlinear Water Waves Generated by Submarine and Aerial Landslides. *Journal of Waterway, Port, Coastal, and Ocean Engineering*, 118(3):249–266.

Heller, V. (2007). Landslide generated impulse waves: Prediction of near field characteristics. *Mitteilungen / Versuchsanstalt für Wasserbau, Hydrologie und Glaziologie der Eidgenössischen Technischen Hochschule Zürich*, 204.

Heller, V. (2008). *Landslide generated impulse waves: Prediction of near field characteristics.* PhD thesis, ETH Zürich., Zürich. Mitteilungen 204, Versuchsanstalt für Wasserbau, Hydrologie und Glaziologie (VAW), H.-E. Minor,.

Heller, V., Bruggemann, M., Spinneken, J., and Rogers, B. D. (2016). Composite modelling of subaerial landslide–tsunamis in different water body geometries and novel insight into slide and wave kinematics. *Coastal Engineering*, 109:20–41.

Heller, V. and Hager, W. (2011). Wave types of landslide generated impulse waves. *Ocean Engineering*, 38(4):630–640.

Heller, V. and Hager, W. H. (2010a). Impulse product parameter in landslide generated impulse waves. *Journal of waterway, port, coastal, and ocean engineering*, 136(3):145–155.

Heller, V. and Hager, W. H. (2010b). Impulse Product Parameter in Landslide Generated Impulse Waves. *Journal of Waterway, Port, Coastal, and Ocean Engineering*, 136(3):145–155.

Heller, V. and Spinneken, J. (2015). On the effect of the water body geometry on landslide–tsunamis: Physical insight from laboratory tests and 2D to 3D wave parameter transformation. *Coastal Engineering*, 104:113–134.

Hernández-Madrigal, V. M., Mora-Chaparro, J. C., and Garduño-Monroy, V. H. (2011). Large block slide at san juan grijalva, northwest chiapas, mexico. *Landslides*, 8:109–115.

Herschel, W. H. and Bulkley (1926). Konsistenzmessungen von gummi-benzollösungen. *Kolloid-Zeitschrift*, 39(4):291–300.

Heyns, J. A. and Oxtoby, O. F. (2014). Modelling surface tension dominated multiphase flows using the vof approach. In *6th European Conference on Computational Fluid Dynamics*, pages 7082–7090.

Higman, B., Shugar, D. H., Stark, C. P., Ekström, G., Koppes, M. N., Lynett, P., Dufresne, A., Haeussler, P. J., Geertsema, M., Gulick, S., et al. (2018). The 2015 landslide and tsunami in taan fiord, alaska. *Scientific reports*, 8(1):12993.

Hirt, C. W. and Nichols, B. D. (1981). Volume of fluid (VOF) method for the dynamics of free boundaries. *Journal of Computational Physics*, 39(1):201–225.

Hogg, A. J. and Matson, G. P. (2009). Slumps of viscoplastic fluids on slopes. *Journal of Non-Newtonian Fluid Mechanics*, 158(1):101–112.

Huang, X. and García, M. H. (1997). A Perturbation Solution for Bingham-Plastic Mudflows. *Journal of Hydraulic Engineering*, 123(11):986–994.

Huang, X. and García, M. H. (1998). A herschel–bulkley model for mud flow down a slope. *Journal of Fluid Mechanics*, 374:305–333.

Huber, A. (1980). *Schwallwellen in Seen als Folge von Felsstürzen.* Doctoral Thesis, ETH Zurich.

Hughes, M. G. (1992). Application of a Non-Linear Shallow Water Theory to Swash following Bore Collapse on a Sandy Beach. *Journal of Coastal Research*, 8(3):562–578.

Iafrati, A. (2011). Energy dissipation mechanisms in wave breaking processes: Spilling and highly aerated plunging breaking events. *Journal of Geophysical Research: Oceans*, 116(C7):2011JC007038.

Imran, J., Parker, G., Locat, J., and Lee, H. (2001). 1D Numerical Model of Muddy Subaqueous and Subaerial Debris Flows. *Journal of Hydraulic Engineering*, 127(11):959–968.

Iverson, R. M. (2005). Debris-flow mechanics. *Debris-flow hazards and related phenomena*, pages 105–134.

Jasak, H. (1996). *Error analysis and estimation for the finite volume method with applications to fluid flows.* PhD thesis, Imperial College London (University of London).

Jeong, S. W., Locat, J., Leroueil, S., and Malet, J.-P. (2010). Rheological properties of fine-grained sediment: the roles of texture and mineralogy. *Canadian Geotechnical Journal*, 47(10):1085–1100.

Julien, P. Y. and Lan, Y. (1991). Rheology of Hyperconcentrations. *Journal of Hydraulic Engineering*, 117(3):346–353.

Jánosi, I., Jan, D., Szabó, K. G., and Tél, T. (2004). Turbulent drag reduction in dam-break flows. *Experiments in Fluids*, 37(2):219–229.

Kamphuis, J. W. and Bowering, R. J. (1970). Impulse Waves Generated by Landslides. *Coastal Engineering*, pages 575–588.

Kessel, T. v. and Kranenburg, C. (1996). Gravity current of fluid mud on sloping bed. *Journal of Hydraulic Engineering*, 122(12):710–717.

Komatina, D. and Jovanovic, M. (1997). Experimental study of steady and unsteady free surface flows with water-clay mixtures. *Journal of Hydraulic Research*, 35(5):579–590.

Lacaze, L. and Kerswell, R. R. (2009). Axisymmetric granular collapse: A transient 3D flow test of viscoplasticity. *Physical Review Letters*, 102(10):108305.

Laitone, E. V. (1960). The second approximation to cnoidal and solitary waves. *Journal of Fluid Mechanics*, 9(3):430–444.

Lander, J. F. (1996). *Tsunamis Affecting Alaska, 1737-1996.* Number 31. US Department of Commerce, National Oceanic and Atmospheric Administration.

Larsen, B. E. and Fuhrman, D. R. (2018). On the over-production of turbulence beneath surface waves in Reynolds-averaged Navier–Stokes models. *Journal of Fluid Mechanics*, 853:419–460.

Latter, J. (1981). Tsunamis of volcanic origin: summary of causes, with particular reference to krakatoa, 1883. *Bulletin volcanologique*, 44:467–490.

Le Méhauté, B. (1976). *An Introduction to Hydrodynamics and Water Waves*. Springer Berlin Heidelberg, Berlin, Heidelberg.

Lee, S. H.-H. and Widjaja, B. (2013). Phase concept for mudflow based on the influence of viscosity. *Soils and Foundations*, 53(1):77–90.

Lemaire, N., Martin-Medina, M., and Abadie, S. (2018). Étude du déplacement d'un caisson de digue verticale induit par un impact de vague de type" flip-through". In *XVèmes Journées Nationales Génie Côtier\textendash Génie Civil La Rochelle, 29 au 31 mai 2018*, pages 457–464. Paralia CFL.

Li, Y. and Mo, P. (2019). A unified landslide classification system for loess slopes: A critical review. *Geomorphology*, 340:67–83.

Li, Y. and Raichlen, F. (2003). Energy Balance Model for Breaking Solitary Wave Runup. *Journal of Waterway, Port, Coastal, and Ocean Engineering*, 129(2):47–59.

Liu, P. C. (2000). WAVELET TRANSFORM AND NEW PERSPECTIVE ON COASTAL AND OCEAN ENGINEERING DATA ANALYSIS. In *Advances in Coastal and Ocean Engineering*, volume 6, pages 57–101. WORLD SCIENTIFIC.

Lubin, P., Vincent, S., Abadie, S., and Caltagirone, J.-P. (2006). Three-dimensional large eddy simulation of air entrainment under plunging breaking waves. *Coastal engineering*, 53(8):631–655.

Maciel, G. d. F., Santos, H. K. d., and Ferreira, F. d. O. (2009). Rheological analysis of water clay compositions in order to investigate mudflows developing in canals. *Journal of the Brazilian Society of Mechanical Sciences and Engineering*, 31:64–74.

Mauriet, S. (2009). *Simulation d'un écoulement de jet de rive par une méthode VOF*. phdthesis, Université de Pau et des Pays de l'Adour.

McFall, B. C. and Fritz, H. M. (2016). Physical modelling of tsunamis generated by three-dimensional deformable granular landslides on planar and conical island slopes. *Proceedings of the Royal Society A: Mathematical, Physical and Engineering Sciences*, 472(2188):20160052.

Menter, F., Ferreira, J., Esch, T., and Konno, B. (2003). The sst turbulence model with improved wall treatment for heat transfer predictions in gas turbines. gas turnine congress (international) proceedings. tokyo. paper no. *Tokyo. Paper*, (IGTC2003):059.

Menter, F. R. (1994). Two-equation eddy-viscosity turbulence models for engineering applications. *AIAA journal*, 32(8):1598–1605.

Middleton, G. and Hampton, M. (1973). Sediment gravity flows: mechanics of flow and deposition. in: Middleton, g.v., bouma, a.h. (co-chairmen), turbidites and deep water sedimentation. *Soc. Econ. Paleontol. Mineral., Pac. Sect., Short Course*, (3-4):89–114.

Miyamoto, K. et al. (2010). Numerical simulation of landslide movement and unzen-mayuyama disaster in 1792, japan. *Journal of Disaster Research*, 5(3):280–287.

Mohammed, F. and Fritz, H. M. (2012). Physical modeling of tsunamis generated by three-dimensional deformable granular landslides: LANDSLIDE GENERATED TSUNAMIS. *Journal of Geophysical Research: Oceans*, 117(C11):n/a–n/a.

Morlet, J. (1983). Sampling Theory and Wave Propagation. In *Issues in Acoustic Signal — Image Processing and Recognition*, pages 233–261. Springer Berlin Heidelberg, Berlin, Heidelberg.

Moukalled, F., Mangani, L., and Darwish, M. (2016). *The Finite Volume Method in Computational Fluid Dynamics: An Advanced Introduction with OpenFOAM® and Matlab*, volume 113 of *Fluid Mechanics and Its Applications*. Springer International Publishing, Cham.

Mulligan, R. P. and Take, W. A. (2017). On the transfer of momentum from a granular landslide to a water wave. *Coastal Engineering*, 125:16–22.

Nairn, R. B., Roelvink, J. A. D., and Southgate, H. N. (1990). Transition zone width and implications for modelling surfzone hydrodynamics. *Coastal Engineering Proceedings*, (22).

Nguyen, V. B. Q., Kang, H.-S., and Kim, Y.-T. (2018). Effect of clay fraction and water content on rheological properties of sand–clay mixtures. *Environmental Earth Sciences*, 77(16):576.

O'Donovan, E. and Tanner, R. (1984). Numerical study of the bingham squeeze film problem. *Journal of Non-Newtonian Fluid Mechanics*, 15(1):75–83.

Openfoam-code (2023a). OpenFOAM ESI: User Guide v2112 - kepsilon.c source code. kEpsilon.C source code.

Openfoam-code (2023b). OpenFOAM ESI: User Guide v2112 - rngkepsilon.c source code.

Openfoam-code (2023c). OpenFOAM ESI: User Guide v2112 - shihquadraticke.c source code. ShihQuadraticKE.C source code.

O'brien, J. and Julien, P. (1985). Physical properties and mechanics of hyperconcentrated sediment flows. In *Proceedings of the specialty conference on delineation of landslide, flash flood and debris flow hazard in Utah, Utah State University, Utah*, pages 260–279.

Packter, A. (1956). Studies in the rheology of clay-water systems. *Kolloid-Zeitschrift*, 149(2):109–115.

Pal, R., Yan, Y., and Masliyah, J. (1992). Rheology of clay-in-oil suspensions with added water droplets. *Chemical engineering science*, 47(5):967–970.

Panizzo, A., Bellotti, G., and De Girolamo, P. (2002). Application of wavelet transform analysis to landslide generated waves. *Coastal Engineering*, 44(4):321–338.

Panizzo, A., De Girolamo, P., and Petaccia, A. (2005). Forecasting impulse waves generated by subaerial landslides. *Journal of Geophysical Research: Oceans*, 110(C12).

Paris, A., Heinrich, P., and Abadie, S. (2021). Landslide tsunamis: Comparison between depth-averaged and Navier–Stokes models. *Coastal Engineering*, 170:104022.

Paris, A., Okal, E. A., Guérin, C., Heinrich, P., Schindelé, F., and Hébert, H. (2019). Numerical modeling of the june 17, 2017 landslide and tsunami events in karrat fjord, west greenland. *Pure and Applied Geophysics*, 176(7):3035–3057.

Paris, R., Switzer, A. D., Belousova, M., Belousov, A., Ontowirjo, B., Whelley, P. L., and Ulvrova, M. (2014). Volcanic tsunami: a review of source mechanisms, past events and hazards in Southeast Asia (Indonesia, Philippines, Papua New Guinea). *Natural Hazards*, 70(1):447–470.

Parsons, J. D., Whipple, K. X., and Simoni, A. (2001). Experimental Study of the Grain-Flow, Fluid-Mud Transition in Debris Flows. *The Journal of Geology*, 109(4):427–447.

Peregrine, D. H. (1966). Calculations of the development of an undular bore. *Journal of Fluid Mechanics*, 25(2):321–330.

Petley, D. (2023). A landslide triggered the 1650 tsunamigenic eruption of Kolumbo.

Piau, J.-M. (2007). Carbopol gels: Elastoviscoplastic and slippery glasses made of individual swollen sponges: Meso-and macroscopic properties, constitutive equations and scaling laws. *Journal of non-newtonian fluid mechanics*, 144(1):1–29.

Pierson, T. C., Costa, J. E., and Vancouver, W. (1987). *A rheologic classification of subaerial sediment-water flows*, volume 7. Geological Society of America.

Poncet, P.-A., Liquet, B., Larroque, B., D'Amico, D., Sous, D., and Abadie, S. (2022). In-situ measurements of energetic depth-limited wave loading. *Applied Ocean Research*, 125:103216.

Pranantyo, I. R. and Cummins, P. R. (2020). The 1674 Ambon Tsunami: Extreme Run-Up Caused by an Earthquake-Triggered Landslide. *Pure and Applied Geophysics*, 177(3):1639–1657.

Raoult, C., Benoit, M., and Yates, M. L. (2016). Validation of a fully nonlinear and dispersive wave model with laboratory non-breaking experiments. *Coastal Engineering*, 114:194–207.

Rauter, M., Barker, T., and Fellin, W. (2020). Granular viscosity from plastic yield surfaces: The role of the deformation type in granular flows. *Computers and Geotechnics*, 122:103492.

Rauter, M., Hoße, L., Mulligan, R. P., Take, W. A., and Løvholt, F. (2021). Numerical simulation of impulse wave generation by idealized landslides with OpenFOAM. *Coastal Engineering*, 165:103815.

Rauter, M., Viroulet, S., Gylfadóttir, S. S., Fellin, W., and Løvholt, F. (2022). Granular porous landslide tsunami modelling – the 2014 Lake Askja flank collapse. *Nature Communications*, 13(1):678.

Redfield, T. F. and Osmundsen, P. T. (2009). The Tjellefonna fault system of Western Norway: Linking late-Caledonian extension, post-Caledonian normal faulting, and Tertiary rock column uplift with the landslide-generated tsunami event of 1756. *Tectonophysics*, 474(1):106–123.

Reid, J. A. and Mooney, W. D. (2023). Tsunami Occurrence 1900–2020: A Global Review, with Examples from Indonesia. *Pure and Applied Geophysics*, 180(5):1549–1571.

Robbe-Saule, M., Morize, C., Henaff, R., Bertho, Y., Sauret, A., and Gondret, P. (2021). Experimental investigation of tsunami waves generated by granular collapse into water. *Journal of Fluid Mechanics*, 907:A11. arXiv: 2010.12308.

Rodi, W. (1980). Turbulence models and their application in hydraulics - A state of the art review. *NASA STI/Recon Technical Report A*, 81:21395. ADS Bibcode: 1980STIA...8121395R.

Romano, A., Lara, J. L., Barajas, G., and Losada, I. J. (2023). Numerical modeling of tsunamis generated by granular landslides in OpenFOAM®: A Coulomb viscoplastic rheology. *Coastal Engineering*, 186:104391.

Rudert, A. and Schwarze, R. (2009). Experimental and numerical investigation of a viscoplastic carbopol gel injected into a prototype 3d mold cavity. *Journal of Non-Newtonian Fluid Mechanics*, 161(1):60–68.

Rusche, H. (2002). *Computational fluid dynamics of dispersed two-phase flows at high phase fractions*. PhD thesis, Imperial College London (University of London).

Russell, J. (1837). “Report of the committee on waves". Technical report, Murray, London. Report of the 7th Meeting of the British Association for the Advancement of Science Liverpool.

Russell, J. S. (1844). Report on waves. Technical report, 14th Meeting of the British Association for the Advancement of U.K., Science, York, U.K.

Saket, A., Peirson, W. L., Banner, M. L., Barthelemy, X., and Allis, M. J. (2017). On the threshold for wave breaking of two-dimensional deep water wave groups in the absence and presence of wind. *Journal of Fluid Mechanics*, 811:642–658.

Sander, J. and Hutter, K. (1991). On the development of the theory of the solitary wave. A historical essay. *Acta Mechanica*, 86(1):111–152.

Saramito, P., Smutek, C., and Cordonnier, B. (2010). The horizontal dam break problem for slow non-Newtonian power-law fluids.

Sarlin, W., Morize, C., Sauret, A., and Gondret, P. (2021). Non-linear regimes of tsunami waves generated by a granular collapse. *Journal of Fluid Mechanics*, 919:R6. arXiv:2105.13991 [physics].

Satake, K. (2007). Volcanic origin of the 1741 oshima-oshima tsunami in the japan sea. *Earth, planets and space*, 59:381–390.

Schaer, N., Vazquez, J., Dufresne, M., Isenmann, G., and Wertel, J. (2018). On the Determination of the Yield Surface within the Flow of Yield Stress Fluids using Computational Fluid Dynamics. *Journal of Applied Fluid Mechanics*, 11:971 – 982.

Shih, T.-H. (1993). *A realizable Reynolds stress algebraic equation model*, volume 105993. National Aeronautics and Space Administration.

Shih, T.-H., Zhu, J., and Lumley, J. L. (1996). Calculation of wall-bounded complex flows and free shear flows. *International Journal for Numerical Methods in Fluids*, 23(11):1133 – 1144. Cited by: 53.

Skvortsov, A. and Bornhold, B. (2007). Numerical simulation of the landslide-generated tsunami in Kitimat Arm, British Columbia, Canada, 27 April 1975. *Journal of Geophysical Research: Earth Surface*, 112(F2).

Soares Frazao, S. and Zech, Y. (2002). Undular bores and secondary waves -experiments and hybrid finite-volume modelling. *Journal of Hydraulic Research*, 40(1):33–43.

Stoker, J. J. (1992). *Water Waves: The Mathematical Theory with Applications.* John Wiley & Sons, Inc., Hoboken, NJ, USA.

Street, N. (1956). The Rheology of Kaolinite suspensions. *Australian Journal of Chemistry*, 9(4):467–479.

Torrance, J. K. (1999). Physical, chemical and mineralogical influences on the rheology of remoulded low-activity sensitive marine clay. *Applied Clay Science*, 14(4):199–223.

Ubbink, O. (1997). *Numerical prediction of two fluid systems with sharp interfaces.* PhD thesis, Imperial College London (University of London).

Varnes, D. (1978). Types and processes. in: Schuster, r.l., krizek, r.j. (eds.), landslides: Analysis and control. *National Research Council, Washington, DC*, pages 11–33.

Viccione, G., Genovese, M., Guida, D., and Lenza, T. L. (2015). Physical modelling of laboratory debris flows by using the Sodium Carboxymethylcellulose ( Na-CMC ).

Viroulet, S., Cébron, D., Kimmoun, O., and Kharif, C. (2013). Shallow water waves generated by subaerial solid landslides. *Geophysical Journal International*, 193(2):747–762.

Viroulet, S., Sauret, A., and Kimmoun, O. (2014). Tsunami generated by a granular collapse down a rough inclined plane. *EPL (Europhysics Letters)*, 105(3):34004.

Viroulet, S., Sauret, A., Kimmoun, O., and Kharif, C. (2016). Tsunami waves generated by cliff collapse: Comparison between experiments and triphasic simulations. In Pelinovsky, E. and Kharif, C., editors, *Extreme Ocean Waves*, pages 173–190. Springer International Publishing.

Walder, J. S., Watts, P., Sorensen, O. E., and Janssen, K. (2003). Tsunamis generated by subaerial mass flows. *Journal of Geophysical Research: Solid Earth*, 108(B5).

Waldmann, N., Vasskog, K., Simpson, G., Chapron, E., Støren, E. W. N., Hansen, L., Loizeau, J.-L., Nesje, A., and Ariztegui, D. (2021). Anatomy of a catastrophe: Reconstructing the 1936 rock fall and tsunami event in lake lovatnet, western norway. *Frontiers in Earth Science*, 9:671378.

Wang, J., Xiao, L., Ward, S. N., and Du, J. (2021). Tsunami Squares modeling of the 2007 Dayantang landslide generated waves considering the effects in slide/water interactions. *Engineering Geology*, 284:106032.

Ward, S. N. and Asphaug, E. (2003). Asteroid impact tsunami of 2880 March 16. *Geophysical Journal International*, 153(3):F6–F10.

Weymann, H. D., Chuang, M. C., and Ross, R. A. (1973). Structure of thixotropic suspensions in shear flow: I. Mechanical properties. *The Physics of Fluids*, 16(6):775–783.

Widjaja, B., Andriani, D., Sutisna, R. A., and Fitri, A. (2015). Alternative way for determination of yields stress as rheology parameter for mudflow. *Int. J. Comput. Civ. Struct. Eng*, 2(2):4–7.

Wiegel, R. L., Noda, E. K., Kuba, E. M., Gee, D. M., and Tornberg, G. F. (1970). Water Waves Generated by Landslides in Reservoirs. *Journal of the Waterways, Harbors and Coastal Engineering Division*, 96(2):307–333.

Wilcox, D. C. (1988). Reassessment of the scale-determining equation for advanced turbulence models. *AIAA Journal*, 26(11):1299–1310.

Williams, J. M. (1985). *Tables of Progressive Gravity Waves*. Pitman Publishing, Boston.

Wroniszewski, P. A., Verschaeve, J. C. G., and Pedersen, G. K. (2014). Benchmarking of Navier–Stokes codes for free surface simulations by means of a solitary wave. *Coastal Engineering*, 91:1–17.

Xu, W.-J. and Dong, X.-Y. (2021). Simulation and verification of landslide tsunamis using a 3D SPH-DEM coupling method. *Computers and Geotechnics*, 129:103803.

Yakhot, V., Orszag, S. A., Thangam, S., Gatski, T. B., and Speziale, C. G. (1992). Development of turbulence models for shear flows by a double expansion technique. *Physics of Fluids A: Fluid Dynamics*, 4(7):1510–1520.

Yavari-Ramshe, S. and Ataie-Ashtiani, B. (2016). Numerical modeling of subaerial and submarine landslide-generated tsunami waves—recent advances and future challenges. *Landslides*, 13(6):1325–1368.

Yeh, H. H., Ghazali, A., and Marton, I. (1989). Experimental study of bore run-up. *Journal of fluid Mechanics*, 206:563–578.

Zitti, G., Ancey, C., Postacchini, M., and Brocchini, M. (2015). Impulse waves generated by snow avalanches falling into lakes. In *Proceedings of the 36th IAHR World Congress, IAHR, The Hague, The Netherlands*, volume 28.

Zweifel, A. (2010). *Impulswellen: Effekte der Rutschdichte und der Wassertiefe*. PhD thesis, Eidgenössische Technische Hochschule Zürich (Versuchsanstalt für Wasserbau, Hydrologie und Glaziologie (VAW)).

Zweifel, A., Hager, W. H., and Minor, H.-E. (2006). Plane Impulse Waves in Reservoirs. *Journal of Waterway, Port, Coastal, and Ocean Engineering*, 132(5):358–368.

# Appendices

# Appendix A

# StrainRate Function Object implementation

## A.1 Steps to define a new Function Object library

A Function Object, or Functor is simply any object that can be called as if it is a function. An ordinary function is a function
With this user-defined library or Functor, it is possible to perform the run-time or post-processing in OpenFOAM By calling them we can do the desired mathematical operations on the intended fields such as velocity, pressure, etc. Then the new variable sets beside the other outputs. Function objects eliminate the need to store all runtime generated data, hence saving considerable resources. Furthermore, function objects are readily applied to batch-driven processes, improving reliability by standardizing the sequence of operations and reducing the amount of manual interaction.
The various function objects are classified as follows:

1. Field
2. Forces
3. Graphics
4. Lagrangian
5. Sampling
6. Solvers
7. Utilities

Of all the library categories the function objects that are of interest are Fields and Forces, as these are the typical types of libraries that are repeatedly utilized in all the simulations performed in OpenFOAM. Already many Function Object have been implemented in OpenFoam for different purposes. For example for `CourantNo`[1] function which computes the field of Courant number and exists in Field Library.
Function objects can be executed by using two methods.

- Using the `functions` sub-dictionary in the `system/controlDict` file:

---

[1] https://www.openfoam.com/documentation/guides/latest/doc/guide-fos-field-CourantNo.html

```
Co1
{
// Mandatory entries (unmodifiable)
type            CourantNo;
libs            (fieldFunctionObjects);

// Optional entries (runtime modifiable)
rho             rho;

// Optional (inherited) entries
field           <phi>;
result          <fieldResult>;
region          region0;
enabled         true;
log             true;
timeStart       0;
timeEnd         1000;
executeControl  timeStep;
executeInterval 1;
writeControl    timeStep;
writeInterval   1;
}
```

- postProcess command-line utility, available to solver applications as well with the option `-postProcess`: `postProcess -func CourantNo <field>`

Here are the required steps for the User-defined Post-Processing function object defining:

1. **Create *.C and *.H files for the function object that is intended to be created.** The *.C file created consists of 5 major sections, namely, Header files, Static Data Members, Private Member Functions, Constructors, Destructor. For simplicity, we can use a ready .C and .H file from another Function Object and then edit purposefully the related sections.
2. **Copy one set of .C and .H files created into the "lnInclude" folder**.
3. **compiling the codes with the following steps in order:**

   (a) **Step 1:** Since, there might be a good number of dependency files, it's suggested to create a new folder named "strainRate" in the function object file of the source folder of OpenFOAM installation.

   (b) **Step 2:** The .C and .H files created for strinRate are copied in the "strinRate" folder. Also, the Make folder is copied from an existing one.

   (c) **Step 3:** The file named "file" is opened inside the Make folder. In this document, change the "executable name" to "strainRate". If one is utilizing the make folder available inside the function object directory under source directory(field or force directory), it's sufficient to include a new executable name for strainRate.

```
strainRate/strainRate.C // in strainRate case
```

(d) **Step 4:** This step is optional, while this can be beneficial for the ones who have copied the templates from existing ones. In the .C file created/copied, one can change the application name and the description in the comment header. This step might be beneficial if this "strainRate" folder files are used as a template to create your own function objects.

(e) **Step 5:** Copy the .C and .H files that have been created for the new function object into the lnInclude folder.

(f) **Step 6:** Go to the directory of "strainRate", i.e, function objects, fields

(g) **Step 7:** In the terminal type:

```
wclean
```

(h) **Step 8:** This is an effective step for compiling, as this avoids permission errors. Type:

```
sudo bash
```

then enter your system password. Now one can compile as a super user.

(i) **Step 9:** Now, in order to compile, type:

```
wmake
```

Thus we compile all the necessary. Here, one compiles as a super user.

(j) **Step 10:**

In order to check if OpenFOAM recognizes the function object that we have compiled, type: `strainRate -help`
The word strainRate can be replaced with the user-defined function object. To exit the super user authorization, type: `ls exit`

Thus, our new function object - "strainRate" has been created successfully. And now one can evoke the strainRate function object in the `controlDict` dictionary simply as:

```
strainRate
{
    type            strainRate;
    libs            ("libmyFieldFunctionObjects.
    so");
    field           U;
    result          strainRate;
    executeControl   writeTime;
    writeControl     writeTime;
}
```

## A.2 `.C` file and `.H` file of strainRate function object

**`.C` file:**

```
/*---------------------------------------------------------
  =========                 |
  \\      /  F ield         | OpenFOAM: The Open Source CFD
   Toolbox
   \\    /   O peration     | Website:  https://openfoam.
   org
    \\  /    A nd           | Copyright (C) 2014-2019
    OpenFOAM Foundation
     \\/     M anipulation  |
----------------------------------------------------------*\

License
    This file is part of OpenFOAM.

    OpenFOAM is free software: you can redistribute it and/
    or modify it
    under the terms of the GNU General Public License as
    published by
    the Free Software Foundation, either version 3 of the
    License, or
    (at your option) any later version.

    OpenFOAM is distributed in the hope that it will be
    useful, but WITHOUT
    ANY WARRANTY; without even the implied warranty of
    MERCHANTABILITY or
    FITNESS FOR A PARTICULAR PURPOSE.  See the GNU General
    Public License
    for more details.

    You should have received a copy of the GNU General
    Public License
    along with OpenFOAM.  If not, see <http://www.gnu.org/
    licenses/>.

\*---------------------------------------------------------*/
```

```
#include "strainRate.H"
#include "fvcCurl.H"
#include "addToRunTimeSelectionTable.H"


// * * * * * Static Data Members * * * * * //

namespace Foam
{
namespace functionObjects
{
    defineTypeNameAndDebug(strainRate, 0);

    addToRunTimeSelectionTable
    (
        functionObject,
        strainRate,
        dictionary
    );
}
}


// * * * * * Private Member Functions  * * * * * //

bool Foam::functionObjects::strainRate::calc()
{
    if (foundObject<volVectorField>(fieldName_))
    {
        return store
        (
            resultName_,
            sqrt(2.0)*mag(symm(fvc::grad(lookupObject<
            volVectorField>(fieldName_))))
        );
    }
    else
    {
        return false;
    }

    return true;
}
```

```
// * * * * * Constructors  * * * * * //

Foam::functionObjects::strainRate::strainRate
(
    const word& name,
    const Time& runTime,
    const dictionary& dict
)
:
    fieldExpression(name, runTime, dict, typeName, "U")
{
//    setResultName(typeName, "U");
}



// * * * * * Destructor  * * * * * //

Foam::functionObjects::strainRate::~strainRate()
{}


// ****************************************** //
```

**.H file:**

```
/*---------------------------------------------
  =========                 |
  \\      /  F ield         | OpenFOAM: The Open Source CFD
   Toolbox
   \\    /   O peration     | Website:  https://openfoam.
   org
    \\  /    A nd           | Copyright (C) 2014-2018
    OpenFOAM Foundation
     \\/     M anipulation  |
---------------------------------------------*\
License
    This file is part of OpenFOAM.

    OpenFOAM is free software: you can redistribute it and/
    or modify it
    under the terms of the GNU General Public License as
    published by
    the Free Software Foundation, either version 3 of the
    License, or
    (at your option) any later version.

    OpenFOAM is distributed in the hope that it will be
    useful, but WITHOUT
    ANY WARRANTY; without even the implied warranty of
    MERCHANTABILITY or
    FITNESS FOR A PARTICULAR PURPOSE.  See the GNU General
    Public License
    for more details.

    You should have received a copy of the GNU General
    Public License
    along with OpenFOAM.  If not, see <http://www.gnu.org/
    licenses/>.

Class
    Foam::functionObjects::strainRate

Group
    grpFieldFunctionObjects
```

```
Description
    This function object calculates the strain rate.

See also
    Foam::functionObjects::fieldExpression
    Foam::functionObjects::fvMeshFunctionObject

SourceFiles
    strainRate.C

/*--------------------------------------------*\

#ifndef functionObjects_strainRate_H
#define functionObjects_strainRate_H

#include "fieldExpression.H"
//#include "fvcGrad.H"

// * * * * * * * * * * * * * * * //

namespace Foam
{
namespace functionObjects
{

/*--------------------------------------------*\
                          Class strainRate Declaration
/*--------------------------------------------*\

class strainRate
:
    public fieldExpression
{
    // Private Member Functions

        //- Calculate the strainRate field and return true
        if successful
        virtual bool calc();


public:

    //- Runtime type information
```

```
    TypeName("strainRate");


    // Constructors

        //- Construct from Time and dictionary
        strainRate
        (
            const word& name,
            const Time& runTime,
            const dictionary& dict
        );


    //- Destructor
    virtual ~strainRate();
};


// * * * * * * * * * * * * * * * * //

} // End namespace functionObjects
} // End namespace Foam

// * * * * * * * * * * * * * * * * //
```

# Appendix B

# Tables of materials properties

## B.1 Rheological properties of real case landslides

The following link offers information on 60 different records of rheological parameters from subaerial real landslide cases. Studies conducted in field, experimental, and numerical methods. This data is in Excel format and provides the information in table B.1 reads as:

- **Author and year:** main author name and year of publishing
- **Slide type:** the category of the landslide
- **Case:** name and information of studied case
- **Type:** type of study: field, experimental or numerical
- **Method:** method of study
- $C_v$**:** estimated solid volume concentration
- **Rheological law:** attributed rheological law to the slide
- $\tau_0$**:** slide yield stress
- $\mu_s$ **and k** Plastic viscosity / consistency index parameters depending on law
- $\mu_s$ **and k** Plastic viscosity / consistency index parameters depending on law
- $n$ power-law index parameters for HB law
- $\rho_s$ Bulk density

| | |
|---|---|
| $\theta$ | Angle of internal friction for slides with frictional rheological law |

Link to access data:
`https://archive.org/details/rheology_real_cases_202401`

Table B.1 – Rheological data format on the real landslide cases

| Author | year | Slide type | Case | Type | Method | $C_v$ | Rheo. Law | $\tau_0$ | $\mu_s$/k | n | $\rho_s$ | $\theta$ |
|---|---|---|---|---|---|---|---|---|---|---|---|---|
| - | - | - | - | - | - | - | - | [Pa] | [Pa.s]/$[Pa.s^n]$ | - | $[gr/cm^3]$ | degrees |

## B.2 Table of runout experiments on the lab scale for rheological materials.

Table B.2 – Rheological runout studies on the lab scale:

| **Study** | **Mixture** | **Type** | $C_v$ | **Rheolo. Model** | $\tau_0$ [Pa] | k [m$Pa.s^n$] | **Bed slope** |
|---|---|---|---|---|---|---|---|
| Komatina and Jovanovic (1997) | kaolin | Exp | 2-23.6% | Bingham | 0<17 | 3.3-43 | [0-0.1%] |
| Saramito et al. (2010) | polymer | Num; Exp | | Power-law | 0 | 34 mks | 0 |
| Balmforth et al. (2007) | kaolin | Theo; Exp | | Herschel-Bulkley | 8.3 | 30±10 | 0 |
| Balmforth et al. (2007) | kaolin | Theo; Exp | | Herschel-Bulkley | 13 | 40 mks | 0 |
| Kessel and Kranenburg (1996) | kaolin | Exp | | Bingham | | | [1:42.6-1:18.5] |
| Huang and García (1998) | kaolin | Exp; Theo | 13.05-22.13% | Herschel-Bulkley | 2.21-17.86 | 0.22-21.30 [$Pa.s^n$] | [18.5-24.5] degree |
| Coussot and Piau (1994) | kaolin | Exp; steady flow | 20.5-24.5% | Herschel-Bulkley | 13-53 | | 45 degree |
| Imran et al. (2001) | bentonite | Num; Exp | | Herschel-Bulkley | 42.5 | 193.2 $s^-1$ | 0.06 |
| Ancey and Cochard (2009) | Carbopol | Theo; Exp | | Herschel-Bulkley | 78-109 | 32-75.8 | [6-24] degree |